Effect of Kinetic Energy due to Hail Impact on Damage Evolution in Gelcoated Glass Fibre Reinforced Polymer Composite

AE5711: Thesis Aerospace Structures and Materials

Saran John Vaseekaran

Delft University of Technology

TU Delft

Effect of Kinetic Energy due to Hail Impact on Damage Evolution in Gelcoated Glass Fibre Reinforced Polymer Composite

by

Saran John Vaseekaran

Student Name	Student Number
Saran John Vaseekaran	5303516

Thesis committee:	Dr. ir. C.D.Rans	TU Delft, Chair
	Dr R.M.Groves	TU Delft, Examiner
	Dr ir J.J.E Teuwen	TU Delft, Supervisor
Project Duration:	March 2022, - January , 2023	
Faculty:	Faculty of Aerospace Engineering, Delft	

TU Delft

Preface

This thesis report has been prepared to partially fulfil the Master of Science Degree in Aerospace Engineering requirement at the Delft University of Technology. This thesis is the culmination of knowledge and experience gained in the past two years, especially during the last few months, where I learnt many skills and applied theories learned in the past years during my master's. I felt challenged during my master's thesis and learned various new skills. I also learnt more about myself and improved myself in certain aspects. This master's thesis gave me a sense of normalcy in these challenging times (due to COVID) by providing an opportunity to work in the laboratory, exchange ideas with peers, gain a new perspective on issues faced during testing and learn from errors made. It has allowed me to meet lots of people and exchange different ideas. Initially, it felt like an uphill struggle at the beginning. But, The support of my friends and family made it more accessible. I would like to thank my supervisor, Dr Julie Teuwen, for her continuous support and guidance throughout the thesis project. I am grateful for her advice, even at odd hours and her patience in helping me to understand concepts throughout the thesis. I always looked forward to our meetings and the feedback I received from her. I am thankful to the staff at DASML - Victor, Alexander, Dave, Johan, Durga and Mohammed, and DEMO- Ed and Rob for their constant support and enthusiasm. Further, I would like to thank my family, especially my mom, for her love, unconditional love, and encouragement throughout my master's. I am grateful to Huseyin Eryörük for his help and advice throughout the thesis. I want to thank Reshab Savanah for being a great company throughout the thesis, helping me brainstorm various ideas and Camill de Vos, Rajneesh Hariharan, Tanya Panda and Anup Bhagali Nataraja for their help and support. I would also like to thank all my friends and roommates in Delft, with whom I made great memories and made my stay in Delft a pleasant and memorable one.

Saran John Vaseekaran
Delft, January 2023

Summary

Leading Edge Erosion is a major and developing concern for the wind energy industry as it affects the power generated and aerodynamic efficiency of wind turbine blades. The erosion caused by Hail impact is considered a more severe form of erosion, as it could significantly damage the protective layer and the composite substrate. The focus of this research study is to investigate the effect of kinetic energy (E_k) on the damage mode in gelcoated glass fibre reinforced composite in terms of the velocity and sizes of the hailstone. The gelcoated glass fibre composite samples were tested using a gas cannon using parameters based on conditions experienced in real life but with slight modifications to enable accelerated testing. Monolithic SHI of 15 mm, 18 mm and 20 mm diameter used in the research for conducting the hail impact experiments were made from deionised water. The gelcoated samples were impacted at various velocities for different hailstone sizes, 15mm hailstone (140 m/s, 150 m/s and 160 m/s), 18mm hailstone (100 m/s, 110 m/s, 120 m/s and 140 m/s) and 20mm hailstone (90 m/s) to determine the Failure Threshold Energy(FTE) for each hail stone size considered. The kinetic energy of each hailstone is estimated from the mass of the hailstone, and impact velocity is measured using a high-speed camera. Using non-contact profilometry (optical microscopy), cross-sectional damage analysis, and ultrasonic c-scan, the damage on gelcoated fibre-reinforced polymer composite samples was analysed. . The coatings did not exhibit any damage or signs of delamination in the coating-substrate interface. However, the substrate showed signs of impact damage. The damage mode was highly influenced by the kinetic energy imparted by hail impact. The damage mode of matrix cracks in the transverse and longitudinal directions was observed in the substrate for most of the impact parameters as the kinetic energies were close to each other. The damage mode remained the same for the different hailstone sizes. The impact test confirmed that FTE existed for each hailstone size (for a particular thickness). It was observed that FTE was increasing with the hailstone size. The conclusion of the work will help further understand damage evolution due to hail impact. It could also provide impetus to create and optimise wind turbine designs based on location to improve blade life. Future research to develop further awareness of damage evolution in coated composites is recommended and discussed.

Contents

List of Figures

List of Tables

Nomenclature

Abbreviations

Abbreviation	Definition
ISA	International Standard Atmosphere
GFRP	Glass Fibre Reinforced Polymer
CFRP	Carbon Fibre Reinforced Polymer
FTE	Failure Threshold Energy
SHI	Simulated Hail Ice
SEM	Scanning Electron Microscope
EASA	European Union Aviation Safety Agency
MIDAS	Meteorological office Integrated Data Archiving System
BVID	Barely Visible Impact Damage
LEE	Leading Edge Erosion
AEP	Annual Energy Production
LCM	Laser Confocal Microscopy

Symbols

Symbol	Definition	Unit
V	Velocity	[m/s]
...		
ρ_{air}	Density of air	[g/cm^3]
ρ_{hail}	Density of ice(hail)	[g/cm^3]
ΔH_{fus}	Enthalpy of fusion or latent energy of fusion	[J/Kg]
r_{hail}	Radius of hailstone	[m]
A_{hail}	Cross-sectional area of hailsone	[m^2]
E_K	Kinetic energy of hailstone	[J]
V_t	Terminal velocity of hailstone	[m/s]
D_{max}	Maximum diameter of hailstone	[cm]
...		

1
Introduction

In response to the recent geopolitical trend of moving away from traditional energy sources such as fossil fuels to more environmentally friendly sources to counter climate change, the wind industry experienced rapid growth, assisted by rapid development in materials and technology. The global annual installation rate for wind turbines has been around 14% for over a decade, as shown in the Figure 1.1. This rapid technological development increased the size of wind turbines in an attempt to achieve higher efficiency and cost-effectiveness. As the size of the rotor blade increase, the tip velocity increases[1]. However, the operational tip velocity is highly dependent on turbine operation and control. The operational tip velocity is usually lower than the maximum turbine tip velocity due to constraints such as location and noise generated by the turbine blades, which in turn have an effect on human well-being. The noise generated increases with the fifth power of velocity [2]. Generally, wind turbines are coated to prevent direct exposure of the wind turbine blades(substrate) to harsh environmental conditions such as particle impacts, bird strikes and much more. However, the coating life of the rotor blade would be significantly affected due to higher tip velocity as the impact energy would be larger. Due to these constraints, wind turbines operate at lower velocities at certain times of the day, such as at night or during stormy conditions[3]. The current trend of using larger turbines with large tip velocities makes the Leading Edge Erosion (LEE) phenomenon more important.

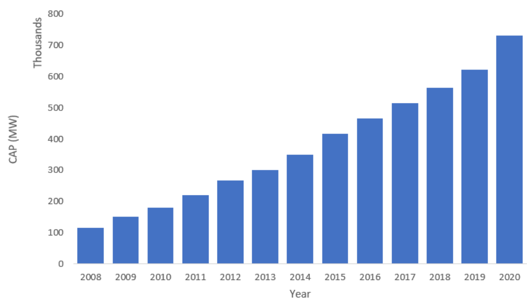

Figure 1.1: Worldwide cumulative wind turbines capacity (MW). Source [4–7]

Leading edge erosion (LEE) affects the leading edge of wind turbine blades. The front edge of the blades makes initial contact with the abrasive particles and droplets in the air [8]. These particles or droplets will eventually erode the coating and expose the composite substrate for further degradation. As mentioned earlier, higher tip velocities have a negative impact on the tip section and the leading edge of the rotor blades. Engel [9] showed experimentally that erosion damage is substantial at greater velocities. Therefore, the impact surface must be either flexible enough to release the stresses or stiff and rigid enough to endure the strains. Erosion of the leading edge generates roughness and surface imperfection, which impacts the aerodynamic nature of wind turbine blades, decreasing their efficiency due to higher drag and decreased lift [10]. This reduces the amount of energy these turbine blades generate.

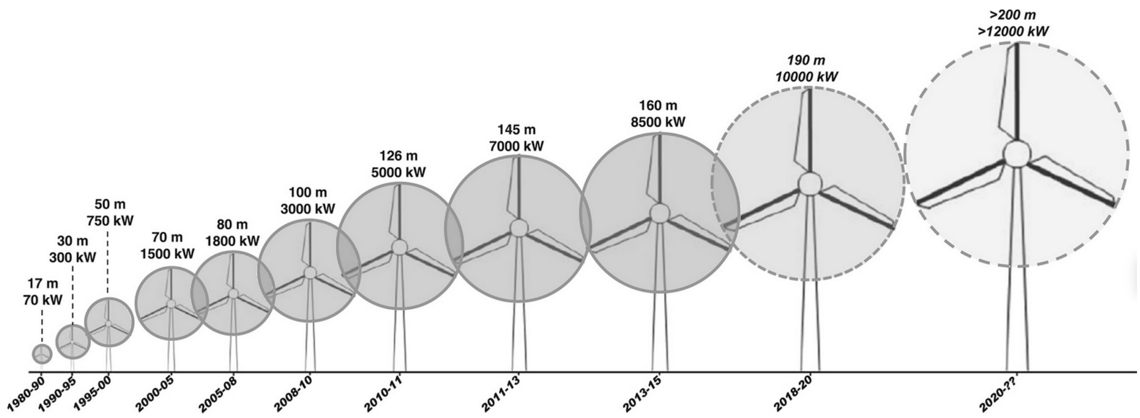

Figure 1.2: Development of turbine blades [11]

The average life of wind turbine blades is 25 years, but LEE significantly reduces turbine life to 5 years or worst case 1 year. Due to the rough profile of the rotor blades caused by LEE, there is an early shift to turbulent flow, affecting aerodynamic efficiency and leading to a yearly decrease in energy production. Even a small amount of coating degradation across the rotor blades significantly affects their aerodynamics. Gaudern [12] discovered that ”minimum erosion” led to a 4% drop in lift and a 49% increase in drag. The reduction in turbine performance caused by leading edge erosion can be better understood when observed from the Annual Energy Production (AEP) perspective. Sareen et al. [13] experimentally calculated that LEE might produce a 6-500% increase in drag and a 0.1% decrease in lift coefficient, which significantly impacts the wind turbine’s energy output of up to 25%. It is important to note that such losses have a significant economic impact on wind energy companies. Wiser [14] calculated that a drop in AEP due to Leading Edge Erosion (LEE) cost the European offshore energy sector between 56 and 72 million dollars due to insufficient production.

Figure1.3 is a visual representation of a wind turbine blade with Leading Edge Erosion (LEE) .

Figure 1.3: Image of LEE on wind turbine blades [8]

LEE not only affects energy production but also has consequences on maintenance complexity and the associated costs. Typically, the wind farm locations are at places that are difficult to access especially offshore rewind farms. Also, weather conditions must be favourable for the repair, and this becomes paramount at offshore locations, as they can be subjected to the whims of the sea. For ideal conditions to allow access and repairs, there must be no large waves and tides. Some repairs require even stringent environmental conditions to make the repairs feasible.

WTG offshore [15] conducted tests that identified and supported the early intervention strategy for repairing damages. These tests were conducted on two different samples with protective coatings. One was previously damaged and repaired, and another was undamaged. There was a sharp difference in the erosion performance of the samples. The sample that had previous damage and repair showed a 70% decrease in the durability of the coatings as the coatings eroded faster. This indicates that the damage in the turbine blades needs to be repaired as soon as they are identified. If they are left to fester before being restored, then the life of the coating would be further shortened. The impact on turbine efficiency and high maintenance costs due to LEE is considered a significant issue, and manufacturers are looking for solutions to reduce the effect. The preferred solution to counter LEE in the wind turbine blades is using an effective protective coating to protect the turbine blades.

Much of the research conducted is on LEE and ways to improve the blade life while keeping the maintenance cost and downtime low. Most of the research focuses on enhancing the protective layer on the leading edge to improve the overall life of the turbine blades and increase time intervals between maintenance. The commonly used protection method against leading edge erosion is either a gelcoat or flexible coating, as discussed earlier by Engel [9].

As wind turbine blades are exposed to severe weather conditions throughout their life cycle, such as UV exposure, precipitation, salinity, humidity and temperature, climate change has profound effects on several wind systems around the world, further affecting their efficiency and maintenance. The most severe form of these weather phenomena is hailstorms. Recent studies have predicted that climate change could significantly affect the size of the hailstones, although the frequency may not necessarily be affected as there are certain conditions for hail to form. But the modelling has shown that hailstorm frequency could increase in Europe and Australia while decreasing in North America and East Asia [16].

This master thesis aims to understand how the size and impact energy of hailstone affects the damage evolution of gelcoats. This research continues to build on the research carried out by Eryörük [17] on the effect of gel coat thickness on erosion performance against hail impact. The study hopes to help further understand the relation between the hailstone size and kinetic energy and help to improve the blade life performance of turbine blades. This form the basis for the research work.

The Structure of the report is as follows: In chapter 2, A Literature review was conducted on wind turbine blades and leading edge erosion with a focus on literature about experimental study and simulation of damage evolution caused due to impact hail impact. At the end of this chapter, literature gaps are identified based on which a research question and sub-questions are defined. The next chapter (i.e. chapter 3) includes a test plan and methodology used to carry out various impact experiments. Additionally, it provides steps to measure multiple parameters such as impact velocity and mass of hailstone. Chapter 4 presents a detailed discussion of the observation and results. In Chapter 5, the major findings of this report are presented. Finally, Chapter 6 briefly gives an overview of the improvements to obtain better results. Additionally, it provides various scopes of research for future projects and to build further on the current thesis.

2 Literature Review

In this chapter, the literature reviewed during the duration of the thesis is presented. In the first section, literature about the wind turbine materials used and standard protection methods are presented. In the subsequent section, the properties and behaviour of ice are sufficiently understood from existing literature, followed by a literature review of the different hailstone impact studies not limited to wind turbine blades. The information presented in this chapter provides the state of research in the field and identifies the gaps of knowledge to formulate the research question presented at the end of the chapter.

2.1. Wind Turbine Blade Material and Structure

Wind turbine blades are an integral part of the wind turbine system. Therefore, much care and consideration are required when designing wind turbine blades for fatigue and structural integrity[18]. The structural design of each part of the blades is explained in detail by Singh et al. [19]. Turbine blades are designed to be thicker near the joint with the rotor hub to resist high bending moments due to different loads acting on the blades[1]. Therefore, they need to have high strength and high stiffness. These criteria are met by composite reinforced materials like CFRP and GFRP. The most commonly used reinforcement fibre in the manufacturing of wind turbine blades are E glass fibres [1]. Other materials such as carbon, S and R glass fibre are also considered alternatives. Studies conducted on Aramid fibres and other hybrid fibres have a promising outlook [18].

The increase in the wind turbine size and scale of use has necessitated using materials with high strength and stiffness in fibre-reinforced plastic composites because of their versatility in material optimisation and high strength-to-weight ratio. Traditionally, Wet hand layup has been the preferred method to manufacture wind turbine blades. With the advent of an increase in the wind turbine blade size, advanced manufacturing processes such as Vacuum Assisted resin transfer moulding is used to manufacture turbine blades. Though the mechanical properties' consistencies were better in prepreg-based composites, they were significantly more expensive than the resin infusion.

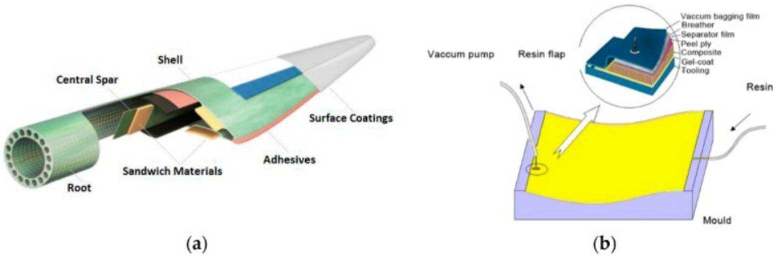

Figure 2.1: Schematic diagram of different parts of wind turbine blades along with its manufacturing process [20]

Research has been conducted on the resin used. Thermoset resin is commonly used in manufacturing wind turbine blades due to its low curing temperature and viscosity. These properties make thermoset resin suitable for making wind turbine blades using the Vacuum-assisted resin infusion process. Recently thermoplastic resins have been used due to their recyclable properties, better fracture toughness [21], infinite shelf life and the possibility of automatic processing[18]. Despite these promising results, much research still needs to be done before using thermoplastics d in producing wind turbine blades.

The commonly used method to protect the wind turbine blades against rain erosion is Coatings. There are different parameters to determine whether a material is suitable to resist leading-edge erosion, such as resistance against abrasive wear or fracture energy in the tensile test, to name a few [22]. Based on those criteria, potential coating systems were identified and used. In general coating system can be subdivided into gelcoats and flexible coatings.

2.1.1. Gelcoats

The gelcoat is manufactured using in-mould techniques. Materials used for gelcoats are similar to those used as the matrix in the substrate, such as epoxy, polyester and urethane [1]. The gelcoat is applied as the first layer to the mould, and dry fibres are placed over the gelcoat. Using in-mould reduces any additional processing steps as optimum adhesion is formed between the coating and substrate as chemical bonds are formed during the infusion process. The gelcoats exhibit low strain-to-failure rates due to their brittle nature and high acoustic impedance.

Figure 2.2: Different post-mould techniques for gelcoats [20]

2.1.2. Flexible coatings

While flexible coatings encompass all polyurethane-based coatings due to their flexible nature in contrast to the brittleness of gelcoat [1]. These coatings are usually applied using spray, trowel or rollers after the moulding process. The drawback of flexible coating is that it offers low impedance and poor adhesion since the coating material is different from the matrix substrate; any delamination problem can accelerate the erosion process. The flexible coatings also exhibit viscoelastic properties making them a suitable choice to resist rain erosion.

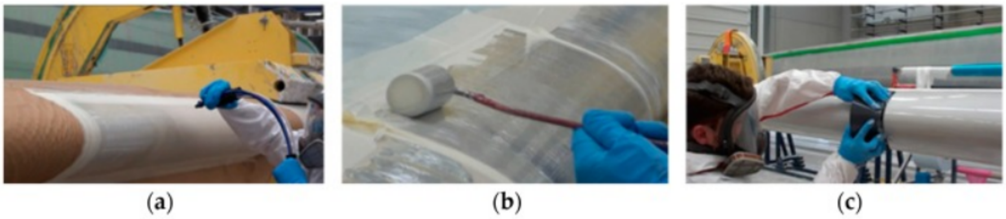

Figure 2.3: Different in mould techniques used for flexible coats [20]

2.2. Hail

‘

2.2.1. General overview

Figure 2.4: Cross-section of hailstone showing the presence of different layers [23]

Hailstones are particles with a mixture of ice/water/air larger than 5mm in diameter [24]. The hailstones smaller than 5mm are considered graupel or ice pellet. The particle's size determines the shape of hailstones. Hailstones grow larger by accumulating layer by layer as it passes through thunderstorm clouds and is layered. Hailstones of sizes between 5mm to 10 mm are generally spherical or conical in nature, and size increase beyond 10 mm are more ellipsoidal as the hailstone sizes grow, their terminal velocity increases [1].

$$V_t = \sqrt{\frac{2 \times w}{c_d \times \rho_a \times a}} \tag{2.1}$$

where V_t is the terminal velocity, w is the weight of hailstone, C_d is the drag coefficient, ρ_a is the density of air, and a is the cross-sectional area of the hailstone.

2.2.2. Distribution of Hailstones and its size

The number of hail storms in the area and the hailstone size of that area are determined by the climatic conditions and other factors beneficial for thunderstorm formation, such as colder upper atmospheric conditions with warmer surface temperatures. Due to these regions, there is an in hailstorm events in early summer. Studies carried out by Keegan M.H [25], and Macdonald H[26] have shown that the frequency of large hailstones (>10 mm) is comparatively small based on the data collected by the UK MET department archive system, also known as Meteorological office Integrated Data Archiving System (MIDAS). The data recorded by ESWD [27] shows hailstones of sizes 3cm in the past five years, with a few hailstones larger than 4cm observed. Due to climatic scenarios and extreme weather conditions, the effect of large hailstones should no longer be ignored.

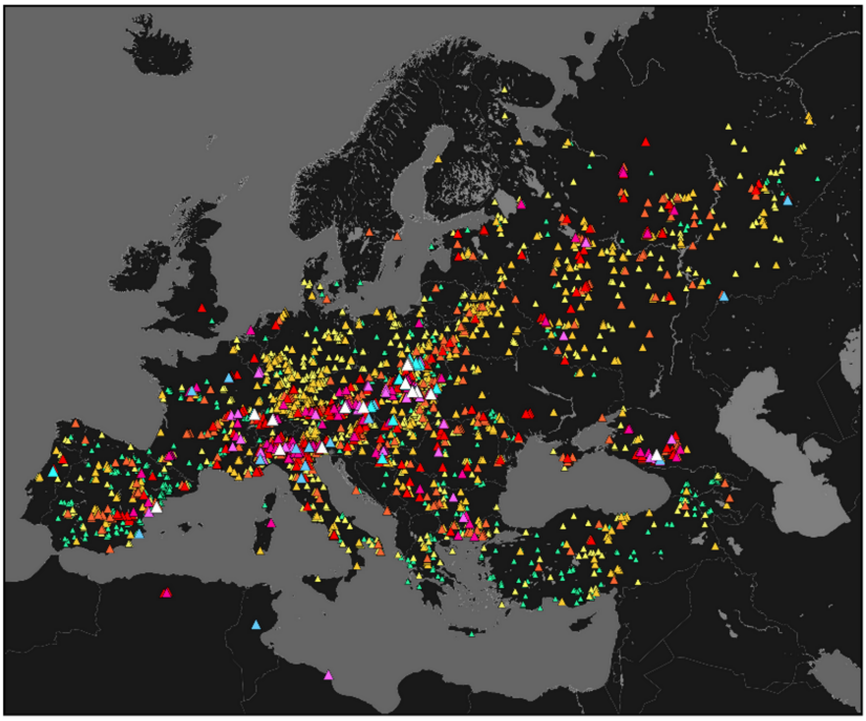

Size	unk	2 cm	3 cm	4 cm	5 cm	6 cm	7 cm	8 cm	9 cm	≥ 10 cm	Total	Size Ratio
Reports 2021	795	1,646	1,137	746	462	196	98	61	25	29	5,195	84.7 %

Data as of *October 31st, 2021*. European Severe Weather Database (ESWD), European Severe Storm Laboratory (ESSL).

Figure 2.5: Hailstone size distribution across Europe during 2021) [28]

2.2.3. Mechanical properties of Ice

Ice is a unique material with 13 different crystal structures and two different amorphous states depending on the cooling conditions [29]. The most commonly found Ice crystal structure is known as tertiary or ordinary ice. Therefore most studies about hail impacts would use ice (Ordinary ice) [30]. Ice is highly sensitive to strain, It has ductile properties at lower strain rates and exhibits brittle nature at higher strain rates. It was estimated that the ductile to brittle transition is observable for strain rates of $10^{-3}s^{-1}$. This phenomenon was first observed by Schulson [29] when compressing cylindrical ice. Polycrystal ice and single Crystal were known to exhibit high stain sensitivity in order $10^{0}to10^{2}$ as per the experiment carried out by Carney et al. [31]. The strain sensitivity of single crystals was experimentally confirmed by Shazly et al. [32]. Impact force and stresses generated onto the blade from hailstone cannot be accurately predicted due to the complexities and variables involved due to the strain sensitivities of hail.

2.3. Hail impact Mechanism

The Mechanism of hail impact is similar to that of Solid particles due to the brittle nature of ice. Telling, R.H et al. [33] have attempted to understand the phenomenon of erosion in aerospace materials due to solid impact. The impinging solid particles generate stress waves which propagate through the sample as shown in the images.

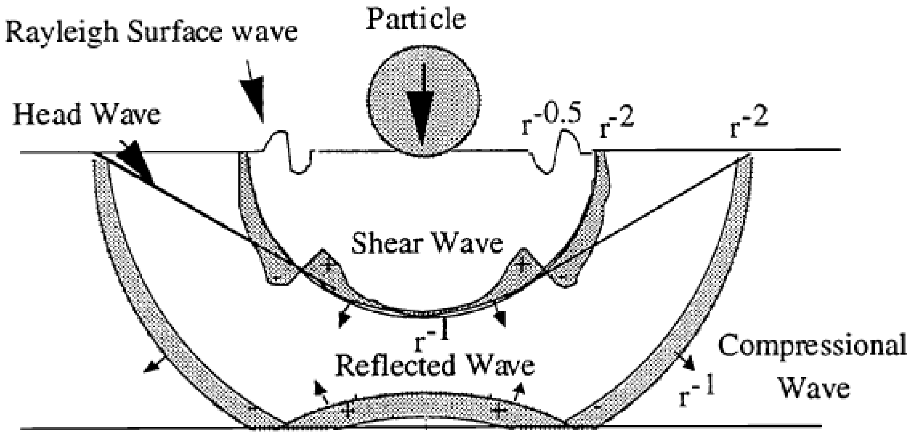

Figure 2.6: Mechanism of solid impact [33]

The Surface waves exploit surface flaws to generate surface damage and undergo less geometric attenuation than the shear and bulk waves. The bulk stress waves, such as compressive and shear waves, could initiate within the substrate upon reflection and change of phase to tensile at the substrate boundaries [34]. Figure 2.6 would give a clear representation of how the stress would propagate in the gelcoated GFRP composite on the impact of the hailstone. At the same time of impact, the contact stresses on impact with the target reach the yield pressure of the ice. It is well-known that ice(Section 2.2.3) shows both ductile and brittle behaviour and behaves like a semi-brittle material at the point where the ice is impinging on the surface as there is increased strain. At the point where the hail makes contact with the target, a crushed zone is generated containing large fragments. This phenomenon of ice crushing is represented in Figure 2.7[35].

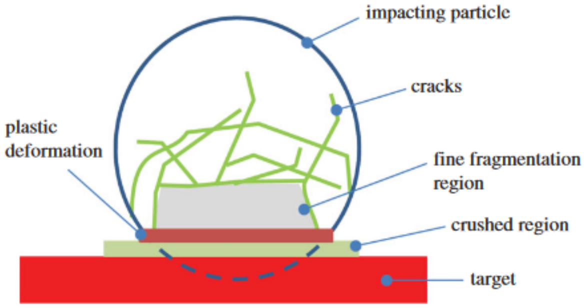

Figure 2.7: Crushing of ice on impact

2.4. Impact Velocity

The mechanism of hail impact is governed by two parameters: the size of the hailstone and impact velocity. The size of the hailstone plays a significant role as it influences terminal velocity(V_t). This is evident, as any change in sizes has a proportional effect on the maximum velocity of the free-falling hailstone(V_t, terminal velocity) and is given by 2.2. This equation is derived by balancing the aerodynamic and gravitational forces acting on this free-falling hailstone[36].

$$V_t = \sqrt{\frac{2 \times m_{hail} \times g}{C_d \times \rho_{air} \times A_{hail}}} \tag{2.2}$$

Where m_h is the mass of the hailstone, g is the acceleration due to gravity, $C_d$is the drag coefficient, ρ_{air} is the density of air (taken as $1.29kg/m^3$) and A_h is the cross-sectional area of the hailstone. this expression can be re-written in terms of the radius by assuming a sphere, As the shape of hailstone is mostly spherical in nature

$$V_t = \sqrt{\frac{8 \times g \times \rho_{hail} \times r_{hail}^3}{3 \times \rho_{air} \times C_d}} \tag{2.3}$$

In this case, r_{hail} represents the hailstone's radius and ρ_h its density. The drag coefficient for spherical hailstones is 0.6 [37]. However, the above-mentioned equation Equation 2.2 and Equation 2.3 didn't account for variation in size and shape. As explained earlier the shape of a hailstone is more elliptical for sizes greater than 20.5 mm. Heymsfield and colleagues [38] established size-dependent relationships for terminal velocities that also accounted for the size.They are depicted in Equation 2.4 and Equation 2.5.The Equation 2.4 is used for sizes less than 20.5 as the shape of a hailstone is expected to change around 2.05 cm. The terminal velocities for larger hailstones 2.05 is given by Equation 2.5.

$$v_t = 12.65 \times D_{max}^{0.65} \qquad D_{max} < 2.05cm \tag{2.4}$$

$$v_t = 15.69 \times D_{max}^{0.35} \qquad for D_{max} > 2.05cm \tag{2.5}$$

Based on the Equation 2.4 and Equation 2.5, a graph predicitng the expected terminal velocity for the hailstone up to 30 mm is shown .

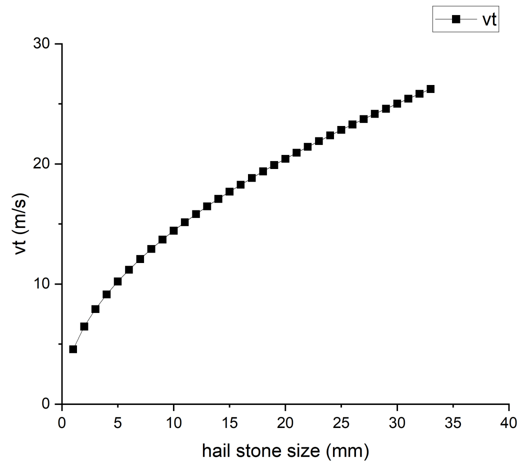

Figure 2.8: Plot relating the terminal velocity to the hailstone size

Keegan et al. [25] calculated the terminal velocity of a 15 mm and 30 mm hailstone impacting a wind turbine blade using Equation 2.2. From Equation 2.9, it is clear that impact velocity is dependent on the mass of hailstone and position of the blade. Maximum impact velocity is achieved when the blade is horizontal and sweeping upwards as the impact velocity would added up with the blade speed resulting in a higher impact velocity at these locations.

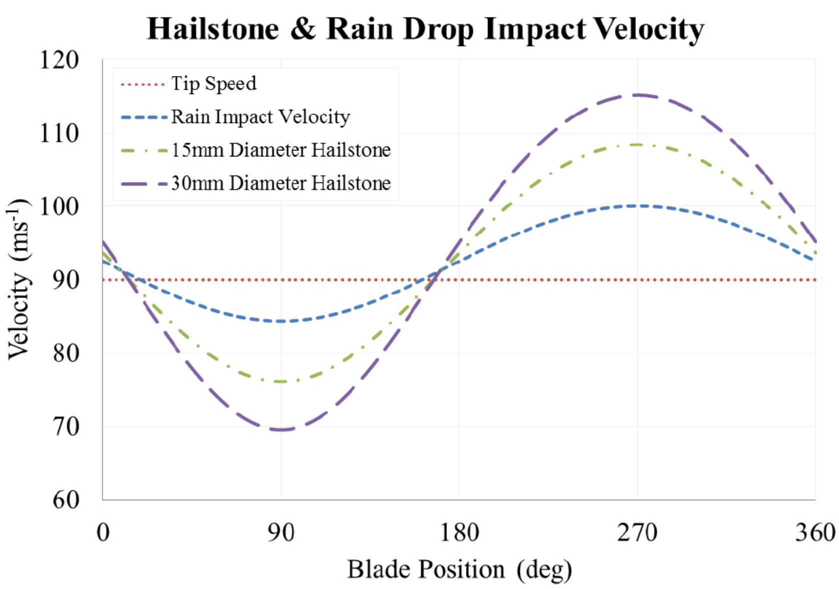

Figure 2.9: impact velocity profile with regards to turbine blade positioning for horizontal blade tip velocity of 90 m/s and wind speed of 8m/s [25]

Similarly, the terminal velocity can be determined using the equation used by Gunn et al [39] and Keegan M.H [1] as shown below:

$$V_t = \sqrt{\frac{2 \times w}{c_d \times \rho_a \times a}} \tag{2.6}$$

where V_t is the terminal velocity, w is the weight of hailstone, C_d is the drag coefficient, ρ_a is the density of air, and a is the cross-sectional area of the hailstone.

2.5. Simulated Hail Ice

As mentioned in section 2.2, the ice formed in nature comprises several layers. Making a hail representing close to the one found in nature is achievable in several ways. It is hard to replicate in lab conditions. Typically, hailstones are manufactured as a monolithic or flatwise layered hailstone. However, The strength of the multilayer spherical layer is significantly tougher than the monolithic or flatwise layered hailstone. ASTM F320-05 [40] suggests adding cotton to hailstones to make them tougher. Ganeshan Ram, S [41] studied the strength of ice when cotton was added to ice. Ice strength improved significantly, and the dynamics of ice impact differed from when normal ice impacts the surface. Several researchers have researched the type of water used on the impact behaviour of ice. The tensile strength properties of ice made from distilled water exhibited higher strength than River water containing minerals [42]. These minerals are also present in tap water. This literature supports the use of distilled water as used by Macdonald, H [26] in making SHI.

A Report by EASA [24] prevents the use of metal balls to replicate hail impact due to their difference in strength and dynamics on impact. Similarly, ceramic beads would generate severe or more damage than expected on impact by an ice projectile.

2.6. Research on Hail Impact

A study modelled the impact of Simulated Hail ice of 42.7 mm on carbon fibre composite using LS-DYNA combined smooth particle hydro dynamics was carried out by Tang et al. [43]. The paper varied various parameters, such as initial impact angle and impact velocity, to understand these parameters' effect on failure mode and energy absorption. Tang, Z et al. [43] studied the effect of simulating impacts at velocities of 100, 120, 140 and 160 m/s at 90°impact angle. The study concluded that the higher the velocity, the larger the delamination area and the larger the peak forces observed. Along with this, the effect of angle and the layup of the laminate was studied, and 90°impact angle showed maximum damage, and $[0/45]_s$ showed the least delamination among the other layup as it could comparatively absorb more energy.

Fiore et al. [44] simulated the impact of hailstones and raindrops on the surface of wind turbine blades. The hailstone of size 50.8 mm promoted delamination at certain locations, such as the leading edge, due to the large tip velocity at those points. This shows the hailstone's sensitive nature to the turbine blades' rotation, but it was comparatively less sensitive to rotation than raindrops.

Saito et al. [45] studied the effect of laminate thickness on the delamination growth by subjecting CFRP laminates to a drop weight test instead of SHI impact and were also subjected to a compressive after-impact test to understand the effect of delamination on its mechanical properties. The test showed that thicker composites had a smaller delamination area but exhibited a larger number of transverse cracks than thinner ones. At the same time, the thinner samples showed higher compressive strength than thicker laminate. Thereby suggesting that thinner plies could absorb more energy than thicker plies [45].

Kim, H et al [46] also modelled the impact response of laminate and showed that the damage mode was dependent on kinetic energy. It was predicted that the smaller hailstone would require less energy.
Kim, H et al.[47] studied the damage modes of thin-walled woven carbon fibre epoxy composites by impacting SHI at a wide range of velocities. This study suggested linear relation between the Kinetic energy at which the damage initiates to the thickness of the composite. It suggests a critical energy level for every composite, known as FTE (FTE), about which damage may be initiated. Additionally, it suggested that the lower FTE is due to the smaller contact area. The damage modes observed are categorised by Kim, H et al. given in Figure:2.10.

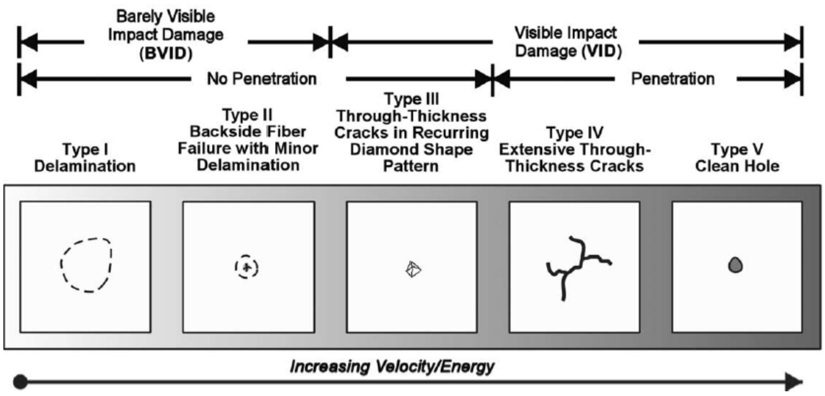

Figure 2.10: Different failures modes observed across different kinetic energies [47]

These categories were referred to in a study by Appleby-Thomas, G.J [48] to determine the ballistics limits of two commercially available carbon fibres. The target (commercially CFRP available targets was impacted with spherical fronted ice over a range of velocities (81 m/s to 268 m/s) using a single-stage gun (driving force: air). After the impact test, the damage modes were characterised using visual inspection, C-Scan and compressive strength. It established a linear relationship with sub-surface damage scan with cumulative projectile impact energy.

The previous papers discussed various damage modes observed across multiple velocities, in contrast to those findings Azouaoui, K [49], and Choi H.Y et al.[50] suggest the initial mode of failure would be matrix cracking. The earlier paper by Kim, h , Saito et al does not provide conclusive evidence of which velocity correlates to which damage mode, making it hard to disregard Azouaoui, K and Choi, H.Y et al. findings. But Elather et al [51] modelled a composite subjected to out-of-plane impact to simulate energy dissipation and understand the damage mechanism and its sequence. This simulation suggested that the initial failure mode was matrix crack followed by induced delamination concentrated mainly at the lower end of the composite. The next failure mode would be fibre breakage which would cause sudden low drop and significant dissipation in the impact. As the damage progresses, the load will decrease with maximum dissipated energy at the time of composite failure. This can be extrapolated to understand the damage mechanism and sequence of damage and have different ways to characterise damage evolution in composites due to hail impact, similar to loading in an out-of-plane direction. This further highlights that matrix cracking could be the initial failure mode.

Atas, C [52] carried out multiple impacts, though the paper uses a drop weight impact testing with a hemispherical nose to replicate SHI to study the effect of various thicknesses on impact response. It was observed that the thinner composites absorbed more energy than thicker composites due to deflection observed in thinner composites as opposed to the thicker composites. The absorbed impact energy was measured by using a piezoelectric sensor. MacDonald, H [26] studied the cumulative effect multiple hail impacts have on glass composites. This was implemented by impacting various SHI diameters over different impact velocities and the number of impacts. The test showed that the severity of damage increased with increasing hailstone diameters for the same numb ere of impacts. The study also indicated that the impact velocity also affected the damage severity, evident from Table:2.2 compiling all the damages observed under SEM as shown in Figure:2.12.

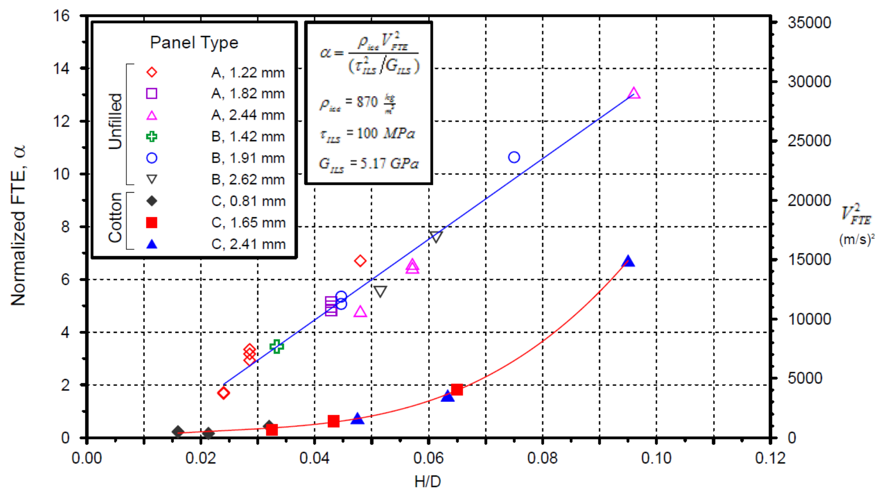

Figure 2.11: Normalised FTE vs ratio of panel thickness and SHI diameter [53]

Mean	Hailstone Diameter	Number of Impacts	
Velocity		5 or 10	25 or 50
Low velocity [40m/s - 70m/s]	5mm	[49.5m/s, 5 impacts] **minimal** surface damage;	[49.8m/s, 50 impacts] **minimal** surface damage;
	10mm	[51.0m/s, 10 impacts] **minimal** surface damage;	[50.6m/s, 25 impacts] **minimal** surface damage; individual loose fibres
	15mm	[57.0m/s, 10 impacts] **minimal** surface damage;	[51.4m/s, 25 impacts] **minimal** surface damage; minor gauges and scarring
	20mm	[47.7m/s, 5 impacts] **minimal** surface damage; minor gouges	[49.4m/s, 50 impacts] **notable** surface damage; large area of removed matrix; no debris or loose fibres; **minimal** scarring
High velocity [80m/s - 120m/s]	5mm	[491.7m/s, 5 impacts] **minimal** surface damage;localised areas of shallow scarring	[90.7m/s, 50 impacts] **minimal** surface damage; individual loose fibres and minor defects
	10mm	[94.9m/s, 10 impacts] **minimal** surface damage; minor debris and individual loose fibres	[96.9m/s, 25 impacts] **minimal** surface damage; minor fibre breakage, gouges and debris
	15mm	[99.5m/s, 10 impacts] **notable** surface damage; large gouges; significant debris; minor fibre breakage; one long furrow	[98.2m/s, 25 impacts] **notable** surface damage; large gouges; debris; areas of major fibre breakage; shallow scarring
	20mm	[89.8m/s, 5 impacts] **notable** surface damage; gouges; minor debris; scattered individual fibres	[86.9m/s, 50 impacts] **notable** surface damage; large gouges; debris; numerous areas of major fibre breakage; deep scarring spread throughout.

Table 2.2: Different damages observed for different hailstone diameters at both lower and higher limit of velocity

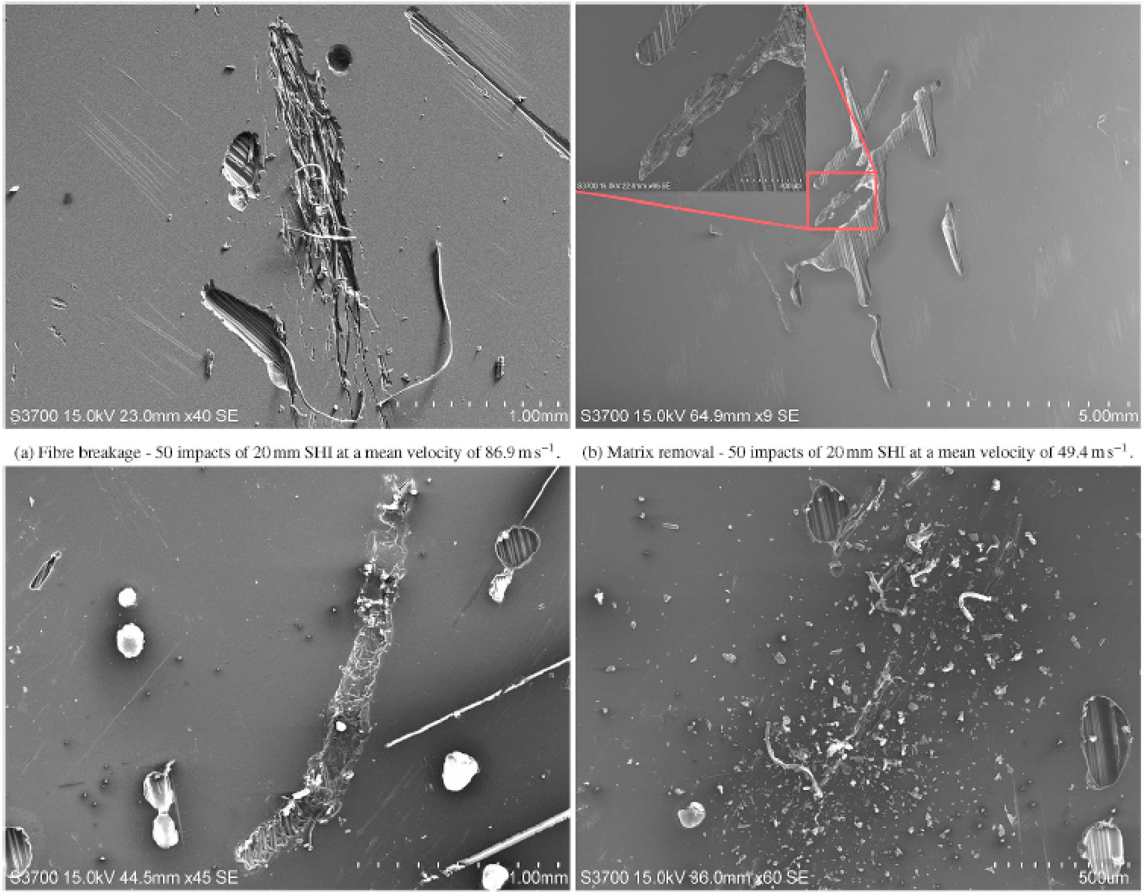

(a) Fibre breakage - 50 impacts of 20 mm SHI at a mean velocity of 86.9 m s^{-1}. (b) Matrix removal - 50 impacts of 20 mm SHI at a mean velocity of 49.4 m s^{-1}.

(c) Scarring - 10 impacts of 15 mm SHI at a mean velocity of 99.5 m s^{-1}. (d) Scattered debris - 10 impacts of 15 mm SHI at a mean velocity of 99.5 m s^{-1}.

Figure 2.12: Different damage modes observed for 15mm and 20mm hailstone [26]

Dolati, SH [54] studied the effect of nanoclay on impact damage resistance of Glass fibre reinforced polymer composite. This study included impacted nanoclay samples of varying concentrations of 0,0.5, 1.5 and 3 (Wt%) and various composite layups and fabric types. This research concluded that woven rovings exhibited better impact damage resistance. This resistance to impact damage was further improved by a presence of 1.5 (wt% nanoclay content compared to 0,0.5, and 3 (wt%). Therefore there could be an ideal nanoclay content at which desirable impact resistance can be observed [54].

Following this, a study carried out as a part of a master's thesis[17] attempted to study how the coating thickness affected the damage evolution of gelcoats due to hail impacts. This paper also used multiple effects to see how the coating thickness affected the damage evolution. This test was carried out by firing SHI of diameter 20 mm using a Gas cannon capable of firing up to 9 bars on GFRP composite coated with epoxy gelcoats of varying thicknesses (0.150mm,0.350 mm and 0.650 mm). The effect of velocity was also considered by impacting hailstone at various speeds on the GFRP composite with epoxy gelcoats of thickness 0.150 mm. The study showed that the thicker gelcoats required less energy to fail due to their brittle nature and a large number of defects in thicker gelcoats [17].

Zhu, X et al. [55] attempted to study how the damage evolves based on a single point impact or a multipoint impact to understand further and simulate very closely what happens in real life and how the difference between what is being simulated in labs. Known damage modes and new damage modes were identified for multipoint impacts. Additionally, it became clear that the mode of failure was not the product of cumulative energy but rather the product of the initial impact energy.

2.7. Research Definition

From the literature study, a range of studies focused on understanding the phenomenon of hail impact and how the damage evolved with or without a protective coating layer highlights the copious amount of work carried out in understanding how barely visible damages such as matrix crack and delamination develop. With the focus on greener energy, the world is moving towards a cleaner future. by moving towards renewable sources, a few counties are focusing on wind energy to meet their demands. This makes it even more important to understand the various parameters which may affect erosion due to hail impact and affect the power generated by the wind turbines. Finding innovative ways to improve turbine life by optimising turbine blades or designing new protective coatings is also imperative. With climate change, extreme weather conditions have become increasingly common. In the past few years, the maximum hailstone diameters have also increased to about 3cm in the Netherlands. This larger diameters hailstone increases the potential for catastrophic damage, Thereby needing to improve our current understanding of the hail erosion phenomenon. No detailed research has been attempted to separate hailstone's kinetic energy and diameter to understand its effect on damage evolution in isolation. The gaps were identified for further investigation from the Literature review, and following the research questions were formulated

> *" How does the size of hailstone and its kinetic energy affect the damage generated in gelcoated fibre reinforced polymer composite?"*

Sub-questions are identified below to help answer the main research question.

1. How does the kinetic energy affect the damage generated in gelcoated composite?
2. How does the size of hailstone affect the FTE in gelcoated composites?

Based on the literature collected on the hailstone impact on composites, it is hypothesised that:

1. Each composite is assumed to have a threshold called Failure Threshold Energy (FTE) below which no damage can be initiated. High-speed impacts generate higher kinetic energy, leading to different failure modes. But this kinetic energy should be higher than FTE.
2. Smaller hailstones should require less energy to initiate damage since the force is concentrated on a smaller region.

A modified form of the existing definition for Failure Threshold Energy (FTE) is provided for clarity and further understanding. In this research, FTE refers to the minimum energy per impact that is required to initiate damage within ten impacts.

3
Test plan and Methodology.

This section presents a brief test plan to answer the proposed research questions. In the later part of the chapter, a methodology for research is presented.

3.1. Test plan

A brief overview of the test plan of the experiments designed to assist in answering the research goal and research question is explained in this section.

3.1.1. Sample preparation

This master thesis is conducted on glass ifbre reinforced plastic (GFRP) composite with an epoxy-based gelcoat. The gelcoated composite was manufactured at DASML using vacuum infusion process by Eryorük [17].The GFRP sample manufactured using biaxial fibre placed in layup $[45/-45/45/-45/45/-45]_S$ create balanced laminate. The epoxy-based gelcoat applied is Rengel SW 5200 with hardener Ren HY5212. The characteristic coating thickness is 75μm (0.075 $\pm$ 0.02 mm) for all the samples subjected to the impact test. The thickness of the GFRP substrate is 3.5 mm (3.54 $\pm$ 0.04 mm). A cross-section with composite lay-up is shown in Figure3.1.

The batches of gelcoated GFRP samples were cut into a square shape to be placed in the impact cannon test rig,(dimensions of the samples: [8.1$\pm$0.4 cm] x [8.08$\pm$0.4] cm). The impact points were ensured to be near the centre of the samples to avoid any edge effect or interference from brackets holding the sample. Before testing, samples were visually inspected in search of defects. If a defect was found, the sample was discarded. The sample used for testing is shown Figure 3.2

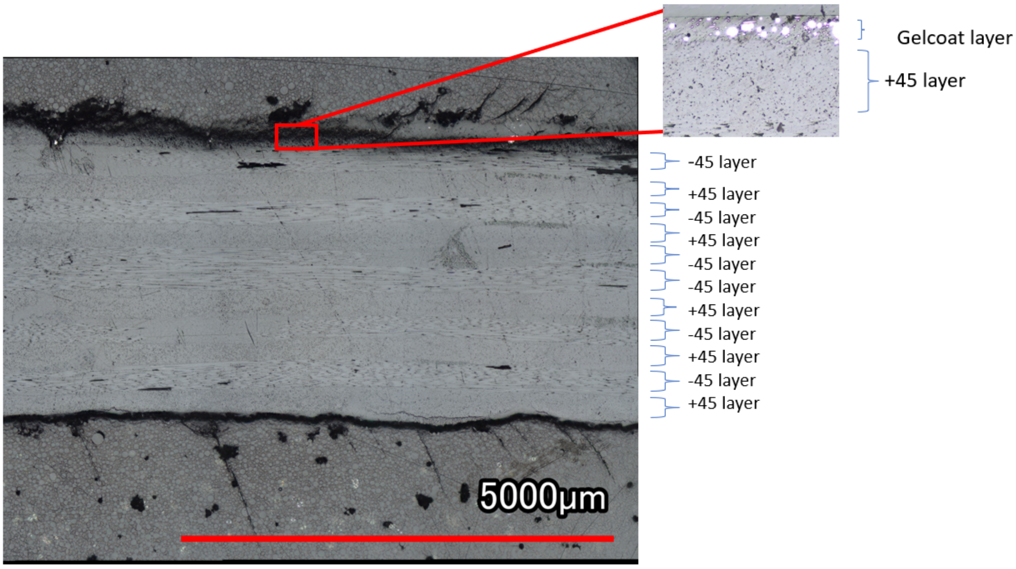

Figure 3.1: The layup of the composite used in this study

Figure 3.2: GFRP composite coated with epoxy gelcoat

3.1.2. Critical Test Parameters

In order to answer the research questions in Section 2.7, a set of essential test parameters must be clearly defined. In Section2.2.2, the increase in the average hailstone diameter has been discussed due to climate change. This highlights a need to understand the damage evolution of larger hailstones. The limitations of the gas cannon setup and the recommendations of EASA discussed in Section2.2.2 were taken into consideration to determine Three hailstone diameters: 15 mm, 18mm and 20 mm hailstone.

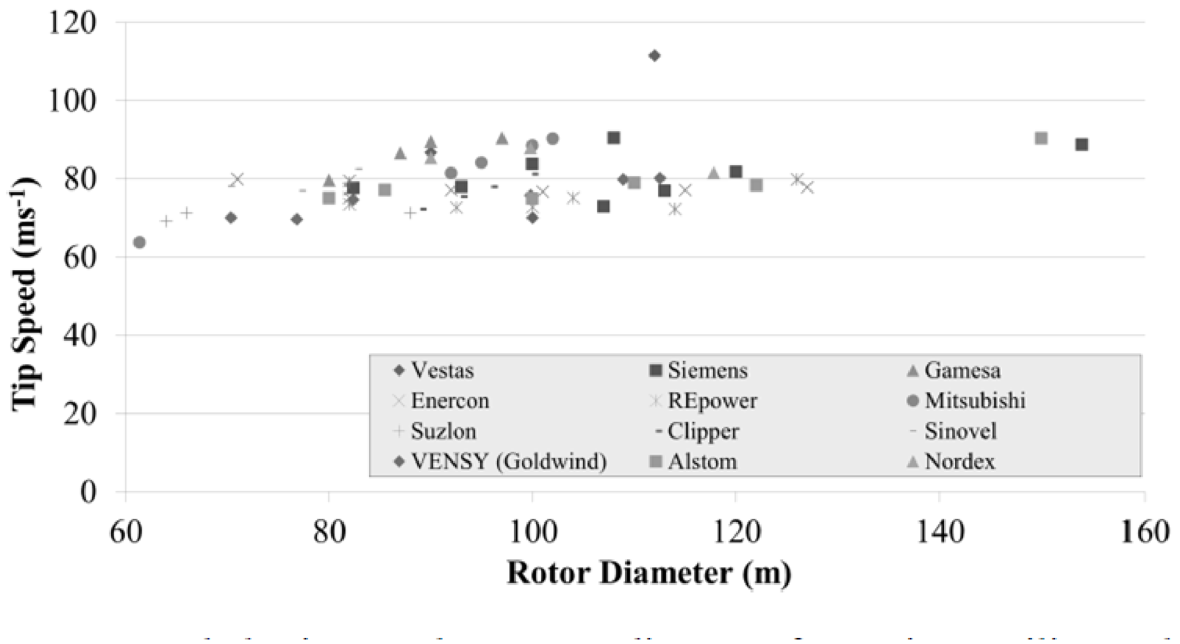

Figure 3.3: Correlation between maximum tip speed and rotor diameter of various wind turbine manufacturers [25]

The next parameter to be determined is impact velocity. The average tip speed for commercially available turbine blades was estimated to be around 90m/s. This information is obtained from Figure 3.3. As mentioned in Section 2.4, each hailstone has its own terminal velocity, which is given by Equation 2.5 and Equation 2.4. The maximum impact velocity was estimated to occur when the blades were in the horizontal position (270°), along with an example to help measure the impact velocity as mentioned in Section 2.4 [1]. To simulate close to real-life conditions, the wind was also taken into consideration along with the terminal velocity with a velocity of the hailstone and tip speed of the blade. The impact velocity for 15 mm hailstone for maximum tip velocity was found to be 106 m/s (wind speed = 3m/s, tip speed =90 m/s and V_t calculated using Equation 2.4). These impacts were found to be insufficient to simulate damage. The impact velocity was increased to 160 m/s(maximum obtainable velocity for the available gas cannon setup) to accelerate damage initiation and evolution. The kinetic energy obtained for this impact value has used a baseline or 18mm and 20 mm hailstones

No standard calibration data is available for hailstone impacts for the gas cannon. Calibrations were performed with a gas cannon to correlate the desired impact velocity to the corresponding pressure value. The velocity was measured from high-speed footage recorded on the high-speed camera(HSC). The two parameters necessary to measure projectile kinetic energy has been defined.

In order to analyse the damage that evolved due to hail impact: non-contact profilometry of the front coating surface, optical microscopy of the rear surface to locate e damage and cross-Section damage analysis to observe the damage evolved across the cross-section of the damage were chosen. This test provided sufficient information to characterise the impact damages observed. LEE causes mass loss in the coating, which would sufficiently provide information to characterise erosion. However, Macdonald et al. [26] found that the change in mass of GFRP composite was negligible or gained by 0,2%. Thereby would not add any additional information on damage observed due to impact.

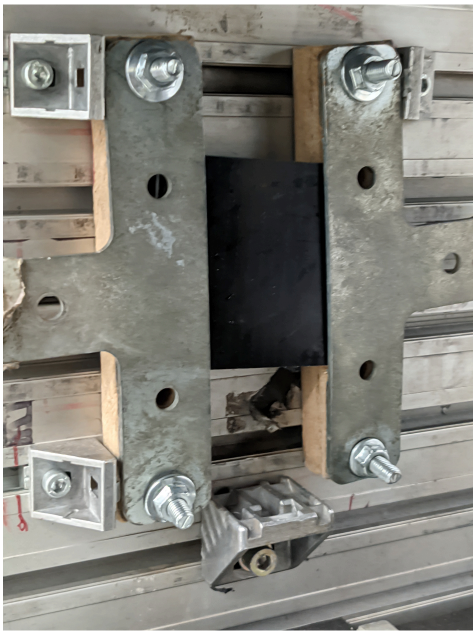

Figure 3.4: Sample clamped inside testing chamber

The boundary condition is that they are clamped on both sides, but the clamping condition would have less to no effect to impact damage generated by high-velocity impact as there would be less elastic deformation of the composite at high velocity, thereby clamping force would have no effect on it [35].

S.no	target Velocity (m/s)	hailstone Diameter	Amount of samples	Analysis intervals
1	140	15 mm	3	1,5,10
2	150	15 mm	3	1,5,10
3	160	15 mm	3	1,5,10
4	100	18 mm	2	1,5,10
5	110	18 mm	3	1,5,10
6	120	18 mm	2	1,5,10
7	140	18 mm	2	1,5,10
8	90	20 mm	1	1,5,10

Table 3.1: Testplan matrix

3.1.3. Experimental setup

In this section, the experimental setup and equipment that will be used are explained in brief.

3.1.3.1. Gas Cannon Setup

The test setup enabling the hailstones to be impacted at composite set up at a particular velocity is a gas cannon setup located at the DASML at the Faculty of Aerospace Engineering at the Delft University of Technology. As identified previously in the literature study, an impact cannon is commonly used to impact hailstones. At DASML, an impact cannon with a pressure capacity of 8 bar circa on a movable frame is used to experiment. An image of the test experiment is shown below in Figure 3.5. Savana et al. [56] and Eryorük [17] provide a brief overview of the different components. Therefore a quick recap of some of the components is highlighted.

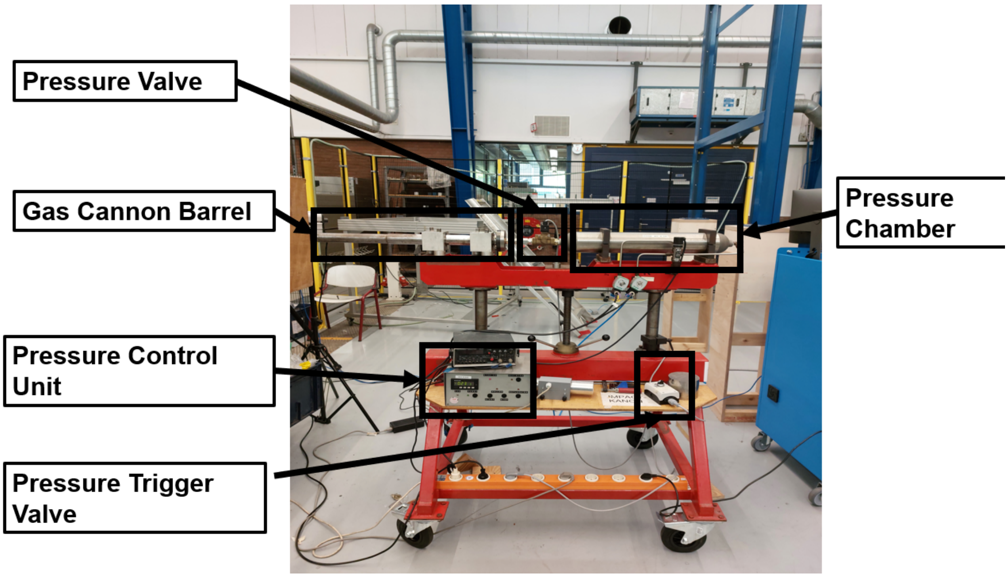

Figure 3.5: Gas cannon test rig

- **Gas cannon barrel:** A stainless steel tube of length 750 mm and inner diameter of 25,4 mm through which SHI is accelerated before impacting the composite.
- **Pressure chamber:** As the name implies, is used to store gas under high pressure before being used to accelerate the SHI. This tank can store at least 30 bars.
- **Pressure valve:** This acts as the connection between the pressure chamber and the barrel.
- **Pressure regulation system:** This assists in the regulation and measurement of pressure in the chamber.
- **Pressure trigger valve:** This enables to relieve the pressure of the pressure chamber to the barrel enabling the launch of SHI.

3.1.3.2. Challenges

Various challenges are involved in launching an SHI using a gas cannon. This issue has been explored in detail and solved by providing a suitable solution for the same test equipment by Eryorük [17].

As explained, the barrel is made up of stainless steel. The material's conductivity accelerated the melting of SHI inside the barrel as observed by Eryorük [17] and Savana [56]. The existing Standards for ASTM F320-21 [57] suggest a method to overcome this challenge but were found unsuitable for this experiment test setup, as observed by Eryorük [17]. Therefore a 3d printed tube is used as a sabot to help launch SHI without generating any debris. This was successfully tested earlier by Eryorük [17], and Savana [56]. The different diameters of SHI being tested would require different sabots. These sabots would either be 3d printed, or acrylic tubes available in the market would need to be machined to the desired specs. This is due to differences in diameters between the inner diameter of the gas cannon barrel and the SHI diameter. If the difference is too large, the SHI would move across the barrel, making multiple contacts with the barrel and shattering before impact. For this research using the 15mm SHI, a sabot was 3d printed using PLA. Similarly, for 18mm and 20mm SHI, acrylic tubes were machined to the dimension of the barrel.

Figure 3.6: 3d printed sabot used to launch 15 mm SHI

Figure 3.7: Acrylic sabot used to launch 18 mm and 20 mm SHI

3.1.3.3. Manufacturing of Simulated Hail Ice

Based on Section 2.5, it is understood that naturally occurring hailstones are layered, which is hard to replicate in lab conditions. The predominantly used SHI in research pertaining to hail impact is monolithic in nature. This research uses PLA moulds to manufacture SHI. The design of these moulds was obtained from Eryorük's work. The mould was manufactured using the 3d printing facility (Ultimaker 2+ and Prusa MK3) at DASML. These moulds were filled with deionised water using a syringe through an opening provided in the mould. The moulds were then placed in a freezer at -22°C for at least 24 hours. After removal from the freezer, mass was measured using the weight difference process, where the moulds were weighed with the SHI inside and then weighed again. This is because transferring the SHI to a ziplock bag led to flattening the SHI on its resting side when placed inside the freezer. The SHI moulds were kept in the freezer for another hour before being removed for usage in the test. The mould was kept at room temperature for 6 minutes before separating the two halves. It was quickly inspected for cracks and voids before being pushed inside the barrel with a PVC cable. It was noted that some mass was lost during the demoulding process. This was accounted for by quickly measuring the mass of SHI without the mould before impact using a ziplock.

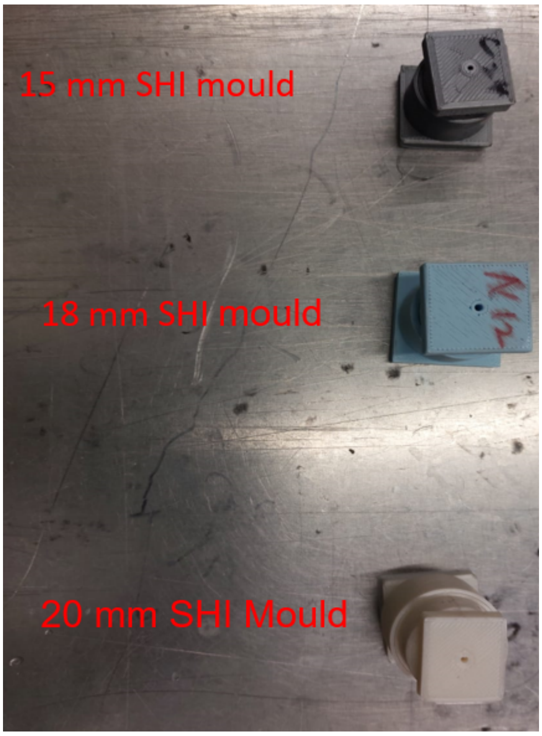

Figure 3.8: SHI moulds of diameter 15mm, 18 mm and 20mm

3.1.3.4. High Speed Camera

The impact event would need to be recorded to characterise the impact event and measure velocity. The impact event is known to last for a few seconds. Therefore, highly specialised equipment is needed to record the event and provide sufficient information for analysis. A high-speed camera was used for this purpose. The high-speed camera position and height are set to assist in capturing the motion of the SHI and its impact event. This study uses **Photron FASTCAM NOVA S6**, which can record and store up to 3 seconds of the impact event. This makes timing the transition from turning on and off the trigger valve to triggering the record switch of the high-speed camera crucial to measuring impact velocity. The impact event was recorded at 20000fps (Resolution:640 $\times$ 480) to capture the impact event in sufficient clarity to assist in determining the impact velocity. In order to understand the effect of kinetic energy, the velocity needs to be known for a given SHI to achieve desired kinetic energy. The scatter of laser by ice rendered the use of IR sensors difficult to use. The high-speed camera is a reliable method to measure velocity due to its ease of use and better reliability due to the above-mentioned problem with the use of IR sensors. The camera used for the experiment is displayed in Figure 3.9.

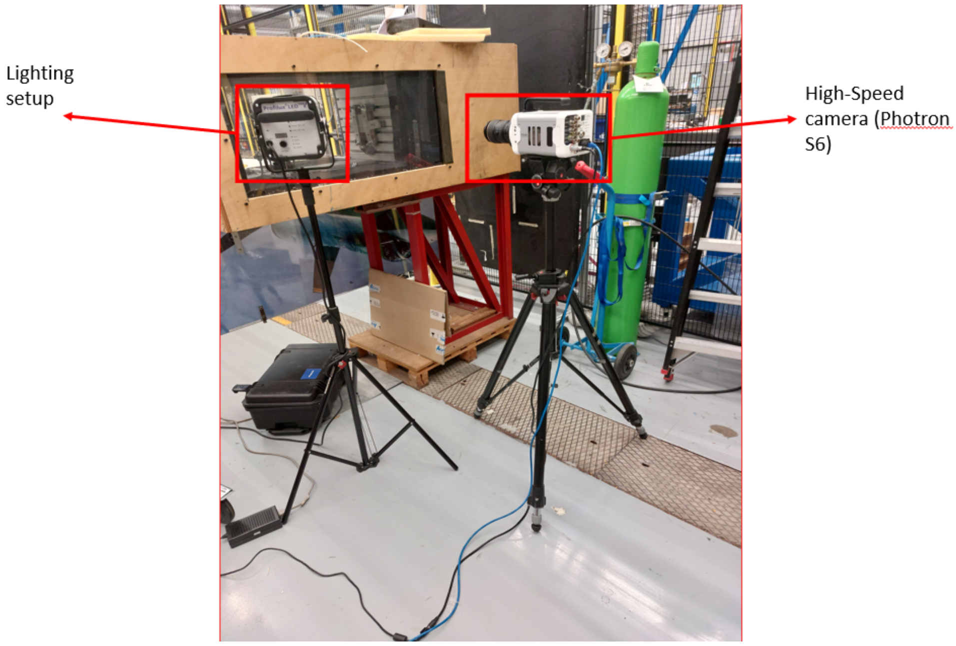

Figure 3.9: High speed velocity measurement set up

3.1.4. Measurement Techniques

3.1.4.1. Mass of hailstone

An important parameter to characterise impact events is the projectile's kinetic energy. One parameter essential for the measurement of kinetic energy is the projectile mass. In Section 3.1.3.3, it was mentioned that there was some mass loss when hailstone was removed from the mould. The indirect measurement of mass and its resultant kinetic energy would be overestimated. The hailstone's mass was measured in a ziplock before impact to minimise mass variation. The mass was determined based on the mass difference approach, where initially the dead weight of the ziplock, followed by the weight of the ziplock along with the SHI was measured. The difference between the measured masses would give the mass of SHI. The measurement is to be done quickly within 15 minutes, including the impact test to ensure that ice doesn't melt or deform significantly. The mass of the SHI measured is represented clearly in the Equation 3.1.where m_h is the mass of the hailstone, m_{zh} is the mass of the hailstone with the ziplock bag, and m_z is the mass of the empty ziplock bag.

$$m_{hailstone} = m_{zh} - m_z \tag{3.1}$$

Additionally, the hailstone was expected to lose mass further prior to impact. However, measuring the conditions and observing how they affected the hailstone during the delay before the hailstone impact proved difficult. An alternate method was used to see how much mass would be lost just before impact was found to be negligible.

3.1.4.2. Effect of Temperature on Mass Measurement

During the test, SHI was observed to start to melt within the time of impact despite launching it within 15 minutes. It is well known that even a small change in mass could cause a change in its kinetic energy. Several methods were attempted to measure the mass of the hailstone before impact. One such method was to measure hailstone mass just before impact by measuring the hailstone dimensions from high-speed footage. This method has its drawback, as it was difficult to determine the edges of the hailstone and its exact position due to the limitation of the high-speed camera used. The final and preferred method was to calculate mass loss before impact theoretically. The mass loss was determined by considering heat transfer by conduction (between the hailstone and sabot) and convection (between the air inside the sabot and the hailstone). The mass loss can be obtained by estimating the energy lost or absorbed while ice changes from solid phase to liquid phase. The mass loss is obtained from basic heat transfer equations: Equation 3.2 and Equation 3.3 as given by Çengel [58]

$$m_l = \frac{Q}{\Delta H_{fus}} \tag{3.2}$$

where m_l is the mass loss before impact, ΔH_{fus} Enthalpy of fusion (ΔH_{fus}= 334000 J/Kg [59]), Q is heat energy transferred into the hailstone from the surroundings through convection and conduction

$$Q = h \times A_{conv} \times \Delta T_{conv} \times t + k \times A_{cond} \times \Delta T_{cond} \times t \tag{3.3}$$

where Q is heat energy transferred into the hailstone from the surroundings through convection and conduction, h is the convective heat transfer coefficient(h= $10w/m^2K$[60]) , k is the thermal conductivity of the material (k=2,22 w/mK [61]), ΔT_{conv} is the temperature difference between the sabot wall and hailstone surface and ΔT_{cond} is the temperature difference between the air inside the sabot and hailstone surface, A_{conv} is the surface area in contact with air ($2 \times \pi \times r^2$) and A_{cond} is the surface area in contact with sabot ($2 \times \pi \times r^2$)

The temperature of the test environment was assumed based on the average temperature during the testing times. The internal temperature of the barrel was estimated to be a few degrees lower than the external temperature. Since temperature would vary throughout the testing campaign, for ease of calculation, an average temperature of air 27˚C was assumed for 15 mm and a temperature of 22˚C for 18 mm and 20 mm SHI. The temperature of the inner wall of the sabot was assumed to be 25˚C was assumed for 15 mm and a temperature of 20˚C for 18 mm and 20 mm SHI. The temperature of the SHI surface was assumed to be 0˚C. The temperature data were based on meteorological data from Visual Crossing database [62]. Based on the assumption and using Equation 3.2 and Equation 3.3, the mass loss for the different SHI over the period of 4 minutes(wait times before launching the hailstone after measuring demoulded mass of the hailstone) is calculated and displayed in Table 3.2

SHI diameter(mm)	Theoretical mass loss over 4 minutes(g)
15	0.082
18	0.096
20	0.12

Table 3.2: Expected mass loss based on the weather conditions during the testing months of August for 15mm SHI and September for 18mm and 20mm SHI

3.1.4.3. Measuring impact velocity

The high-speed camera setup shown in Figure 3.9 is used to record the impact event. Velocity is calculated from the change in the position of the hailstone over a given time obtained from the high-speed footage. This is given by Equation 3.4. The position of the hailstone was determined with respect to the sampled, using an aluminium substructure with a scale

$$V_{hailstone} = \frac{dx}{dt} \tag{3.4}$$

The high-speed camera needs to be set up at the desired position concerning the test setup. Velocity is measured by determining the position of the SHI on a frame and determining the distance travelled between a few frames with the help of ImageJ software. The time is calculated based on the frame rate of the camera. The estimated time depends on factors like camera frame and rate number of frames for a set distance. In this case, the frame rate is 20000 fps, and the time per frame can be estimated using the formula $\frac{1}{20000\,th}$ of a second. The distance measured is across 7 frames; hence, the time is 0.00035 seconds.

This setup needs to be calibrated for each hailstone diameter to achieve target velocity, as there is no prior calibration data. Additionally, a small change in mass can significantly change velocity. Therefore, it is essential to calibrate hailstone for hailstone diameters. The calibration plot for each hailstone diameter used has been plotted and displayed in Figure 3.10.

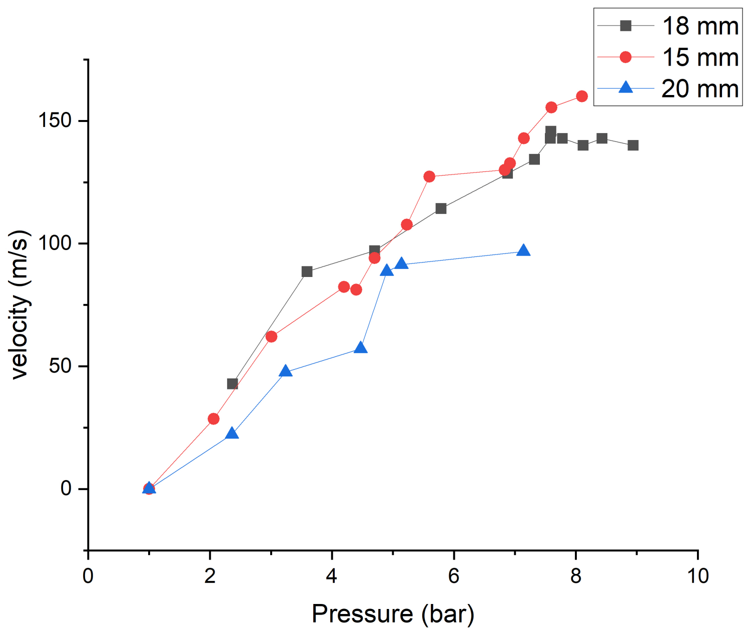

Figure 3.10: Pressure Vs velocity calibration plot

This experiment was carried out for each hailstone diameter as the impact velocity would decrease for a given pressure diameter with increasing hailstone diameter due to its mass.

3.1.5. Analysis after impact

The samples must all be scanned, and images must be taken using c-scan, laser confocal microscopy(LCM) and optical microscope before impact. So, any damage generated after impact can be easily identified using Pressure prior to impact.

3.1.5.1. Optical Microscope and Laser Confocal Microscopy

The damage evolution in the sample needs to be observed at different locations very close to the impact location or apparent damage location. Any damage that could occur on the coating side is captured using Keyence VR 5000(Figure 3.11, a wide-area optical microscope. The microscope enables the imaging of the entire sample at a higher resolution. The same set-up with its 3d measurement system is used for carrying out height profile analysis of the area of interest. This would be useful in investing in coating damage as it helps characterise the damaged area and mass loss.

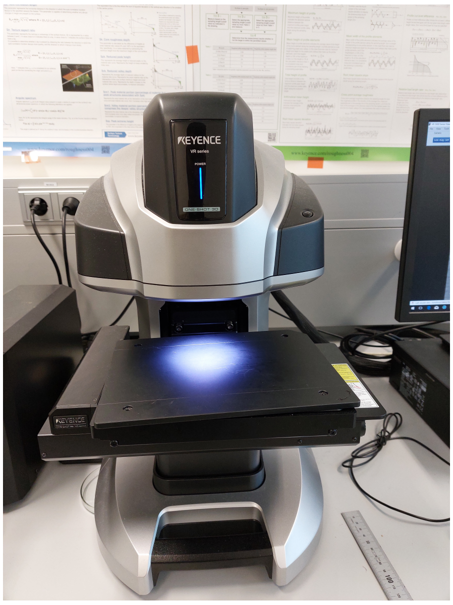

Figure 3.11: Keyence VR 5000 Wide-Area 3d measurement system

Figure 3.12: Keyence VK-X1000 Profile Analysing laser Microscope

Laser confocal provides a high resolution of damages in the substrate due to focus variation, which reduces brightness and scattering of light from a source which seems to plague the wide-area microscope in analysing substrate damages. The substrate damage can be analysed using Keyence VK-X10000(Figure 3.12, a profile analysing laser confocal microscope. This enables the imaging of the smallest form of damage, such as matrix crack, and carries out a cross-sectional analysis. The major drawback is its higher resolution, scanning zone, and scanning time is limited, Thereby only allowing scanning of the damage zone to show the presence of damage and not clearly define the location of the damage.

3.1.5.2. C-Scan

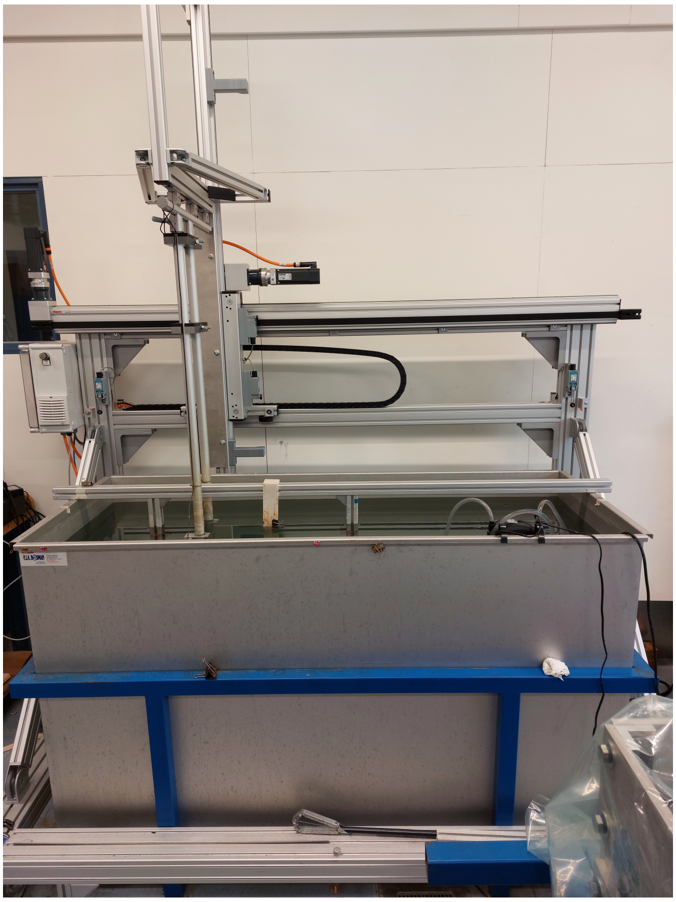

Figure 3.13: C-Scan set up

In order to identify and locate any delaminations and porosity in a sample, an ultrasonic C-Scanner is used. The scanner used in this study is Olympus Epoch 650. A 10MHz transducer is used to send and receive the pulse-echo. This frequency is sensitive enough o identify small defects in glass fibre composites. According to Savana [56]. The wavelength of the C-Scan can be estimated to be 148 μm for this set-up DASML at TU Delft. This wavelength is small enough to identify matrix cracks. But The Sample is held in place by attaching it to a steel bar with a paper clip and ensuring the entire sample is required to be underwater to get reliable results. This is due to the result of C-Scan analysis, which is presented as the intensity of ultrasonic waves received by the receiver. Water is an excellent medium allowing easy coupling of the transducer allowing for the waves to pass. The Damages can be identified by attenuation of signal strength caused by discontinuities in the material.

3.1.5.3. Cross section Analysis

The presence of any damage observed by the optical method needed to be verified. With the current Technology and technical know-how, there is no easy way to identify the presence of barely Visible Damage. Therefore, It is suggested to observe the Damage in the microstructure using destructive techniques such as cross-sectional analysis.

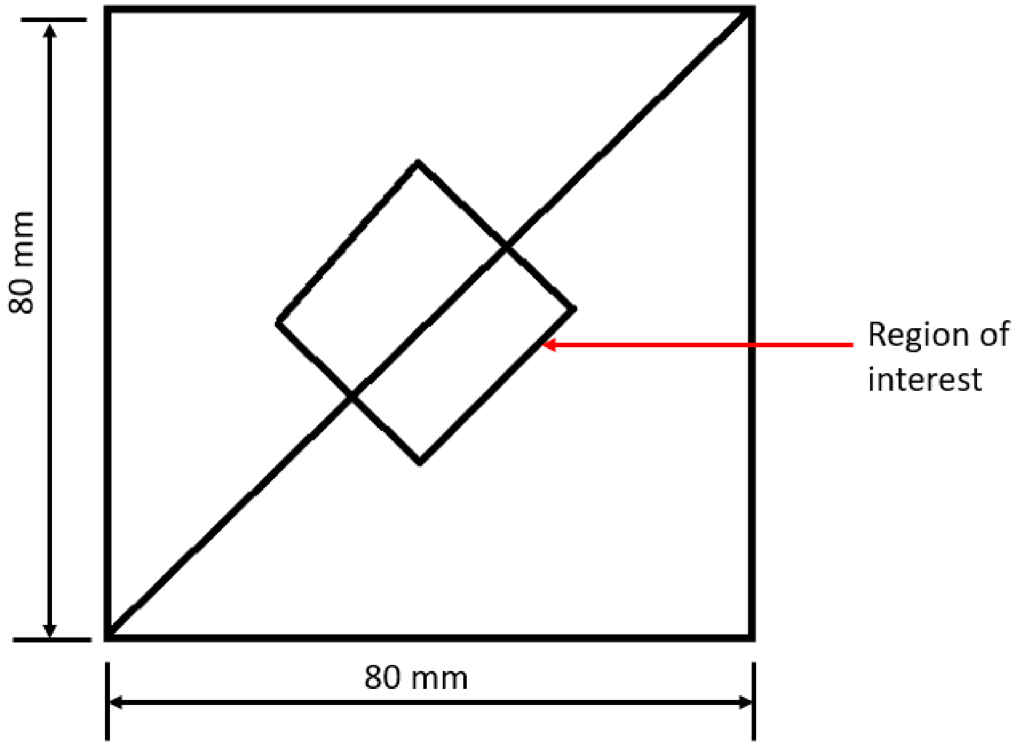

Figure 3.14: Schematics of the location of cross-section analysis of the sample

The sample is cut at 45° as shown in Figure 3.14 so that two halves of the region of interest are obtained. Additionally, a sufficient offset of 3mm is provided so that the damage is not lost during the grinding and polishing process. The sample is cut using a Secotom 10 cutting machine with a thin diamond blade. Extreme care is required, and coolant needs to be used sufficiently so that damage is not affected by heat generated or by the cutting action. The desired samples are then cleaned using an ultrasonic cleaner to remove any foreign particles and debris present. The desired side is embedded in the resin using plastic moulds with the area of interest being placed facing down which allows for easier grinding and polishing down the line. The resin is mixed according to a predetermined ratio specific to that resin. Once the resin is mixed and poured into moulds, ensure at least 75 % mould is filled to ensure proper sample coverage. The sample can be cooled before the embedded samples are removed from moulds. Then the samples are ground through a series of grinding paper from 180 μm to 4000 μm and polished across two polishing plates on the Tegramin-20 based on the predetermined program saved in the Tegramin-20 which was deemed to be suitable for this study.

3.1.5.4. Threshold Energy Measurement

The hailstone impact can be characterised using impact energy. The impact energy of hail impact is the kinetic energy of the hail impact. The impact energy of each hail impact is calculated using Equation 3.5.

$$E_k = \frac{1}{2} \times m_h \times V^2 \tag{3.5}$$

where E_k is the kinetic energy and m_h is the mass of the hailstone and V^2 Velocity of impact of the hailstone.

From Section 2.6, it is that each composite is expected to have critical impact energy below which damage does not occur. In order to determine the threshold energy, simultaneous imaging and analysis of the composite at regular intervals of impact were necessary as it hinged on identifying obvious signs of damage on the composite. Additionally, qualitative microscopic observation under a bright light source was carried out to identify the critical energy, after which damage was observed and verified under a laser confocal microscope. The impact energy or kinetic energy at which the damage was initially observed was taken FTE for that sample. In certain cases, although the threshold energy was reached, the damage was not observed. This does not mean the damage was not initiated, the damage initiated was not large enough to be observed visually. However, the damage becomes more visible after subsequent impacts because the damage has grown large enough to be observable to a naked eye or under optical microscope. This issue was overcome by comparing the energies and identifying the highest impact energy before the damage was deemed to be initiated. FTE measurement was also compared with the threshold energies of hail impacts carried out under similar conditions. The procedure for FTE measurement was followed for all composites. The procedure is significantly different from the previous methods carried out to measure FTE. Kim, H et al [47] carried out hail impacts of the different velocities for the same hailstone diameter. The energy before the impact damage observed was taken as FTE. In this study, the test procedure was designed with the idea to take effect multiple impacts on FTE and get a more accurate value or a range of values for FTE.

4

Results and Discussion

According to the methodology discussed in Chapter 3, The impact test is carried out using gas cannon and analysing the composites for damage. This chapter provides a brief overview of the results after each analysis stage and the findings are discussed in detail.

4.1. Observation

4.1.1. Impact Test

The mass and velocity of SHI measured for each SHI are displayed in Appendix A along with their kinetic energies calculated using Equation 3.5. Each SHI's kinetic energy is estimated to determine the FTE required to initiate damage. Additionally, cumulative impact energy was calculated for 5 and 10 impacts to determine if there was any cumulative effect on damage evolution. An overview of information about the damage observed is displayed in Table 4.1. Table 4.2 shows the results of the kinetic energy of each sample impacted by different SHI sizes and the corresponding information regarding the average velocity and mass.

From the impact test conducted, the following results have been obtained. The FTE for each composite exhibiting barely visible damage(BVID) has been determined by visual observation and optical microscopy images. The FTE is determined based on a comparison of values from previous impacts and a previous sample of all the velocities and number of implications after which damage was observed and kinetic energies which did not generate damage. The FTE was determined as mentioned in Section 3.1.5.4 for each SHI. During the testing procedure, a loss in mass of the stone was observed. To account for this loss, the mass of the SHI was determined by measuring the diameter of the SHI before impact from the high-speed footage. But the change was almost negligible. Additionally, the test was carried out between the end of summer and the beginning of spring.

Sample Id	target Velocity (m/s)	SHI size	Average mass(g)	Average velocity (m/s)	Damage observed after 1st impact	Damage observed after 5 impacts	Damage observed after 10 impacts
A2	140	15 mm	1,50	143	no damage	no damage	no damage
B8	140	15 mm	1,50	144	no damage	no damage	no damage
B2	140	15 mm	1,43	146	no damage	no damage	no damage
B7	150	15 mm	1,48	154	no damage	matrix crack	matrix crack
B3	150	15 mm	1,59	151	no damage	matrix crack	matrix crack
B4	150	15 mm	1,50	153	no damage	no damage	matrix crack
B6	160	15 mm	1,58	160	matrix crack	matrix crack	matrix crack
A7	160	15 mm	1,54	160	matrix crack	matrix crack	matrix crack
A5	160	15 mm	1,56	158	matrix crack	matrix crack	matrix crack
A9	100	18 mm	2,80	102	no damage	matrix crack	matrix crack
B10	100	18 mm	2,92	103	no damage	matrix crack	matrix crack
B5	110	18 mm	2,88	109	no damage	no damage	matrix crack
A8	110	18 mm	2,86	110	no damage	matrix crack	matrix crack
B9	110	18 mm	2,93	111	no damage	matrix crack	matrix crack
A1	120	18 mm	2,92	119	matrix crack	matrix crack	matrix crack
A4	120	18 mm	2,88	119	matrix crack	matrix crack	matrix crack
A3	140	18 mm	2,89	131	matrix crack	matrix crack	matrix crack
A6	140	18 mm	2,80	138	matrix crack	matrix crack	matrix crack
A10	90	20 mm	4,28	90	no damage	no damage	matrix crack

Table 4.1: Damage conditions of the samples subjected to SHI impacts

Sample Id	SHI size	Average mass(g)	Average velocity (m/s)	estimated threshold failure energy to initiate damage(j)	kinetic energy after 1 impact (j)	Cumulative kinetic energy after 5 impacts (j)	Cumulative kinetic energy after 10 impacts (j)
A2	15 mm	1,50	143	NA	11,31	72,49	149,93
B8	15 mm	1,50	144	NA	16,17	76,66	155,29
B2	15 mm	1,43	146	NA	15,1	73,42	166,97
B7	15 mm	1,48	154	19,51	19,51	84,78	180,20
B3	15 mm	1,59	151	19.49	17,43	87,22	179,94
B4	15 mm	1,50	153	19,16	19,14	90,99	191,90
B6	15 mm	1,58	160	19,14	19,14	102,21	221,35
A7	15 mm	1,54	160	19,51	19,51	95,31	195,68
A5	15 mm	1,56	158	18.96	18,96	98,16	194,69
A3	18 mm	2,89	131	26.33	26,33	180,44	295,40
A6	18 mm	2,80	138	21,72	21,71	128,04	266,38
A1	18 mm	2,92	119	26,32	26,32	110,07	208,38
A4	18 mm	2,88	119	21,58	21,58	100,39	205,62
B5	18 mm	2,88	109	19,41	19.10	98,69	204,96
A8	18 mm	2,86	110	19,61	16,92	88,02	189.23
B9	18 mm	2,93	111	19,21	17,04	88,56	180,32
A9	18 mm	2,80	102	19.45	13,23	74,85	147,78
B10	18 mm	2,92	103	19.18	13,38	80,05	158,54
A10	20 mm	4,28	90	19.80	17,17	77,74	192,53

Table 4.2: Kinetic energy per impact and cumulative kinetic energy due to multiple SHI impacts

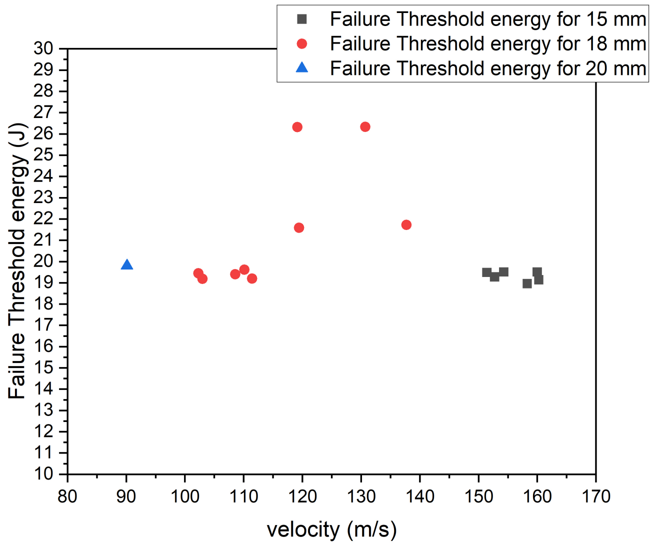

Figure 4.1: FTE as a function of velocity for 15mm, 18mm and 20mm SHI without accounting for mass loss

In sample B7, an interesting observation was made during impact testing 15 mm SHI at 150 m/s, the sample did not show any indication of damage after 1^{st} impact even though kinetic energy at impact was estimated to be 18.52 J which in comparison to other impacts for the same impact parameters was above the energy level at which damage was observed. But subsequent impacts of 15mm SHI at similar velocity exhibited white striation though estimated kinetic energy was 16.64 J.

The matrix crack is the maximum damage observed for all samples due to the low kinetic energy induced in the sample during impact. The 15 mm SHI were impacted at three different velocities to determine the FTE. The samples did not show any damage on the rear side, indicating the absence of any damage for 15mm SHI when impacted at 140m/s. Whereas higher velocities of 150 m/s and 160 m/s showed signs of damage, such as white striations indicating the presence of matrix cracks. Similarly, the samples impacted with 18mm SHI at velocities of 100 and 110m/s displayed white striation after certain impacts. However, the sample impacted at velocities of 120m/s and greater showed matrix cracking characteristics after the first impact, as the impact energy was way above the FTE. Finally, for the sample impacted by 20 mm SHI, the damage was noticed after the 6^{th} impact, where the damage was observed to be initiated because the kinetic energy had reached the FTE level for a resultant impact velocity of 94 m/s. The mass loss was theoretically calculated based on the expected weather using thermodynamic equation: Equation 3.2 and Equation 3.3 which was reported in Table 3.2. This was accounted for and corrected for in the final FTE and displayed in Table 4.3.

Sample Id	SHI size	Average mass(g)	Average velocity (m/s)	estimated threshold failure energy to initiate damage(j)	kinetic energy after 1 impact (j)	Cumulative kinetic energy after 5 impacts (j)	Cumulative kinetic energy after 10 impacts (j)
A2	15 mm	1,42	143	NA	10,59	68,30	141,11
B8	15 mm	1,42	144	NA	16,17	72,30	146,57
B2	15 mm	1,35	146	NA	15,2	68,99	157,12
B7	15 mm	1,40	154	18,47	18,47	79.67	169,94
B3	15 mm	1,51	151	18,53	16,46	82,61	170,40
B4	15 mm	1,42	153	18,16	18,10	86,13	181,16
B6	15 mm	1,50	160	18,1	18,10	96,91	193,82
A7	15 mm	1,46	160	18,47	18.47	89,94	184,96
A5	15 mm	1,48	158	17,85	17,85	92,86	184,15
B10	18 mm	2,82	103	18,57	12,92	77,33	153,23
A9	18 mm	2,70	102	18,81	12,77	72,25	146,82
B9	18 mm	2,83	111	18,57	16,46	85,61	174,30
A8	18 mm	2,76	110	18,94	16,34	85,00	182,74
B5	18 mm	2,78	109	18,77	18,46	95,30	197,98
A4	18 mm	2,78	119	20,87	20.87	96,89	198,63
A1	18 mm	2,82	119	25,44	25,44	106,49	201,38
A6	18 mm	2,70	138	20,8	20,8	123,36	257,08
A3	18 mm	2,79	131	25,44	25,44	174,35	285,47
A10	20 mm	4,18	90	19,27	16,70	75,47	187,16

Table 4.3: Kinetic energy per impact and cumulative kinetic energy due to multiple SHI impacts taking into account the mass loss

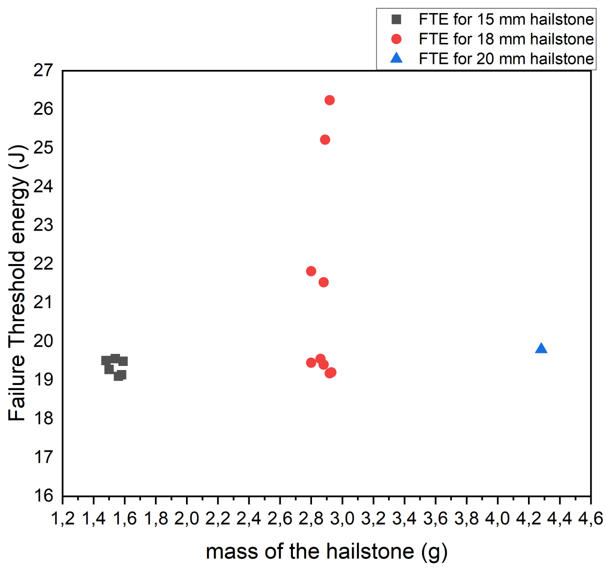

Figure 4.2: FTE as a function of SHI mass for 15mm, 18mm and 20mm without taking mass loss into account

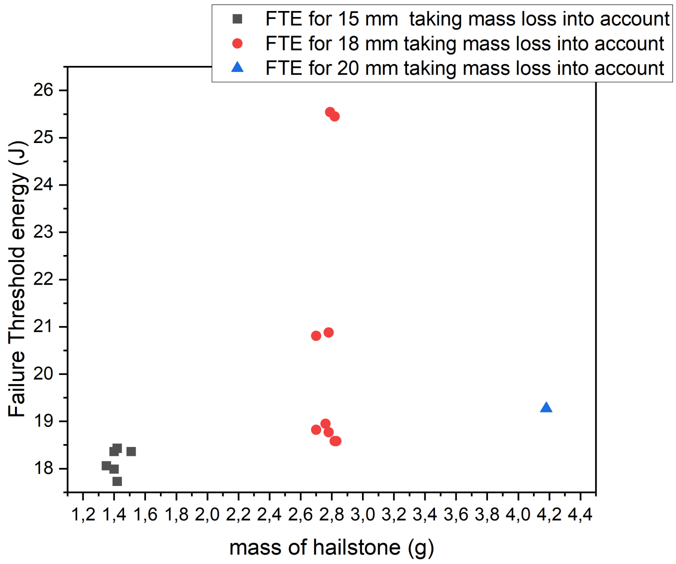

Figure 4.3: FTE as a function of SHI mass for 15mm, 18mm and 20mm taking mass loss into account

From Figure 4.2, there is an indication that FTE is being almost constant with an increase in mass as observed in all the plots before accounting for mass loss. Similarly, Figure 4.3 showed that the FTE would increase with an increase in mass as there exist a linear relation between mass and FTE. This confirms that change in mass or SHI diameter would increase the FTE. These plots also show the significant effect the mass lost has on the FTE. This loss highlight the need to have an accurate method to measure mass of SHI.

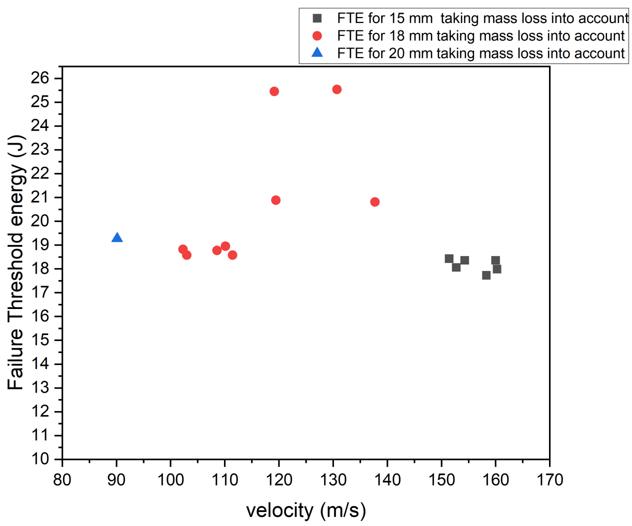

Figure 4.4: FTE vs impact velocity after taking corrected mass loss before impact into account

Similarly, Figure 4.4 showed that the FTE would decrease with an increase in velocity.. From the plot , velocity and FTE seems to have an inverse relation. In Figure 4.4, though some points have higher FTE values for 18 mm, these points were taken at velocities which were well above the minimum velocity at which damage is initiated, which is 110 m/s. These velocities where tested in order to identify the critical velocity at which FTE for 18 mm SHI exists. The critical Velocity referred to in this section can be defined as the minimum velocity at which the velocity can be initiated for that particular SHI within 10 impacts.

4.1.2. Damage Analysis

This section states the observations based on different analyses performed at different stages of the experiments. The first section presents the initial analysis to ensure no obvious manufacturing defects that could significantly affect the results and prevent a reasonable conclusion from being drawn.

All the samples were subjected to visual and microscopic inspection before impact on the Coated side(outer edge) and non coated sides (inner edge) of the sample to check for any damages before commencing the test. The samples exhibit vertical and horizontal white lines and no other obvious manufacturing defects, as seen in Figure 4.5. The horizontal and vertical lines indicate the stitches used to hold non-crimp fibre layers in place and are visible due to the transparent matrix used. Other defects, such as porosity and delamination, would be identified by C-Scan. It is pertinent to mention that the c-scan images showed the presence of no voids or delamination in the samples except for the sample used for the impact test for the 18 mm SHI impacted with an average velocity of 100 m/s.

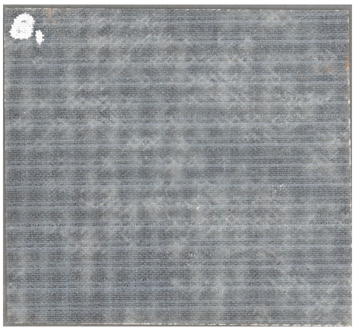

Figure 4.5: Image of non-coated side (inner edge) of the composite sample

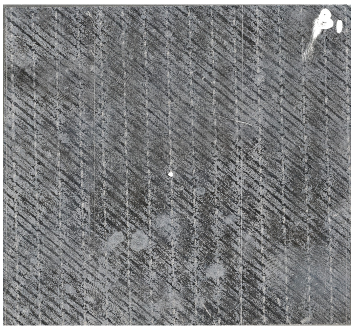

Figure 4.6: Image of gelcoated side of the composite sample

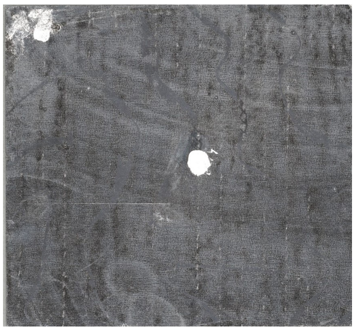

Figure 4.7: Intact gelcoat of sample A7 after 10 impacts with 15 mm SHI at 160 m/s

Figure 4.8: Height profile of A7 post 10 impacts

Following the impact test, the impact damages due to the SHI impact are generally barely visible to the naked eye. Therefore, it needs to be inspected using ultrasonic testing. The C-Scan images of the sample after the impact tests are shown in Appendix C. Sample impacted with 20mm SHI at 90m/s displayed presence voids(black spots), but there were no signs of apparent delamination. Comparing Figure 4.11 and Figure4.12, no clear evidence suggests the voids delineated into a matrix crack because of the impacts. Overall most of the samples did not display any presence of voids or delaminations.

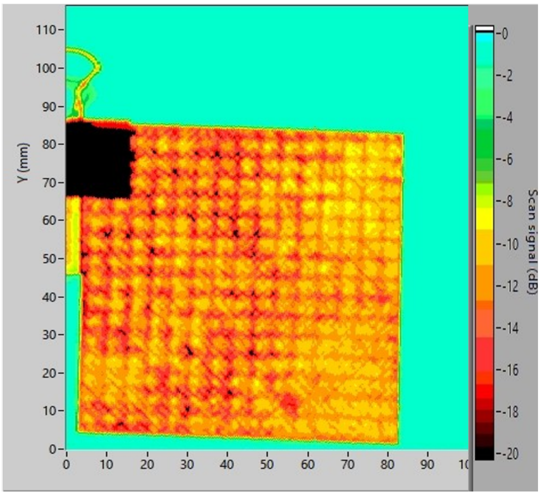

Figure 4.9: C-scan images of sample before impact with 18mm SHI at 110 m/s

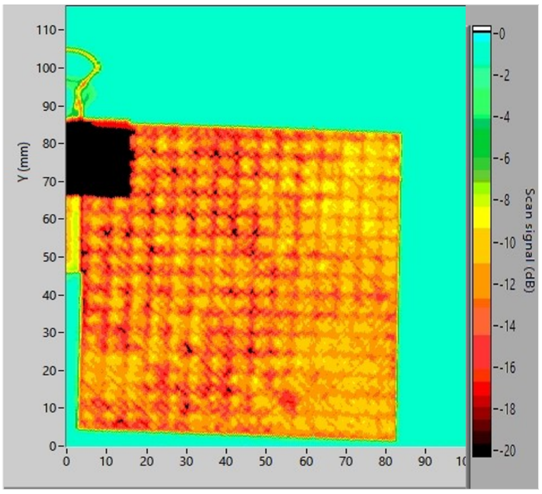

Figure 4.10: C-scan images of Sample impacted with 18mm SHI at 110 m/s(10 impacts)

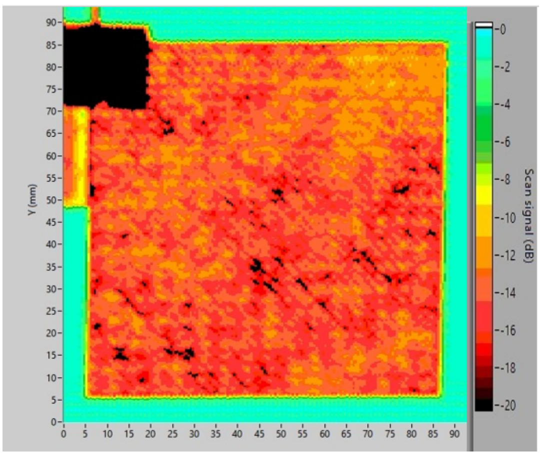

Figure 4.11: C-scan images of sample B10 before impacts with 18 mm SHI at 100 m/s

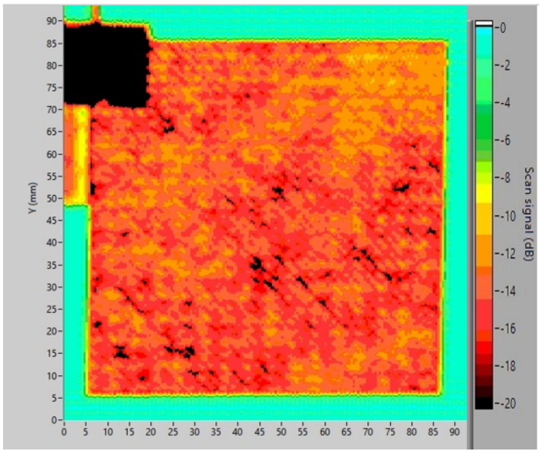

Figure 4.12: C-scan images of sample B10 impacted with 18 mm SHI at 100 m/s (10 impacts)

In order to analyse the coated substrate for any obvious damages post-impact, non-contact profilometry and microscopic analysis were performed. In non- contact profilometry, the surface profile was analysed, and representative images of the profile observed are displayed in Figure 4.8, Figure 4.14 and Figure 4.13. From Figure

4.15 (height map), it is evident that the sample is without any sign of coating degradation. It can be concluded from this image that the coating has good resistance for the tested parameters.

Similarly, all impacted samples did not show any signs of coating degradation. High impact velocity had little effect on the surface profile of the 15 mm, 18 mm, and 20 mm samples. It is speculated that the higher coating stiffness and strength protect it from any damage or changes to the surface profile, indicating that the coating can still resist damage at velocities up to 160 m/s and 140 m/s for said number of impacts (Figure 4.15 and Figure 4.14) for 15mm and 18mm SHI. This is also observed with 20 mm SHI impacting at an average velocity of 90 m/s.The excellent impact-resistant properties of the coatings do not result in any coating damage. The optical microscopic images of all the samples impacted at different velocities and SHI sizes showed no change in the height of the coating layer when post-processing the height image using surface analysis software, indicating the absence of any damage to the coating surface.

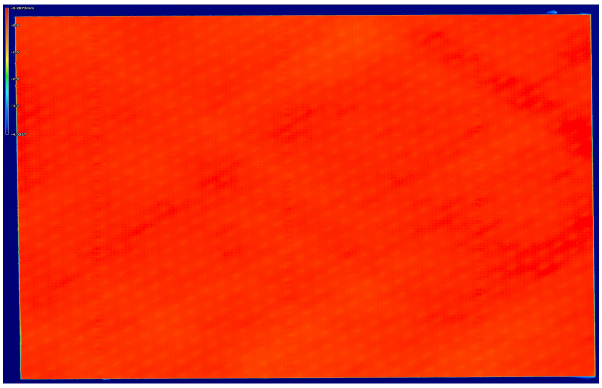

Figure 4.13: Height profile of A10 sample impacted with 20mm SHI at 90 m/s(after 10 impacts)

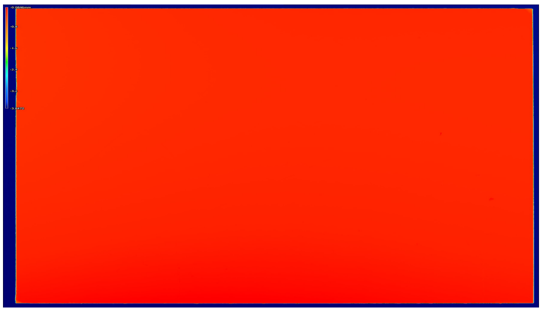

Figure 4.14: Height profile of A3 sample impacted with 18mm SHI at 140 m/s (after 10 impacts)

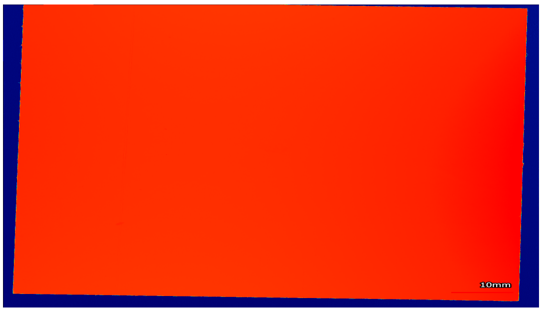

Figure 4.15: Height profile of A5 sample impacted with 15mm SHI at 160 m/s (after 10 impacts)

Subsequently, the rear side of the sample was inspected for barely visible impact damages, such as matrix cracks and delamination. Notably, oblique striations (for impacts at 150 m/s and above for 15 mm SHI) were observed at a short distance towards the lower left of the sample, away from the impact zone. These are interpreted as signs of matrix cracks. At velocities lower than this, no such features were noted. Similar but more distinct matrix cracks were seen for samples impacted at an impact velocity of 110 m/s with an 18 mm SHI. The highest impact velocity achieved for a fully intact 18 mm SHI test was 116 m/s. However, the damage is not observed for a target velocity of 100 m/s. Though the target velocity was 100 m/s, there were occasional impacts where the impact velocity was more than 110 m/s, for which the damage was observed (white striations). Thus it can be concluded that for impact velocity of 110 m/s is necessary to initiate damage

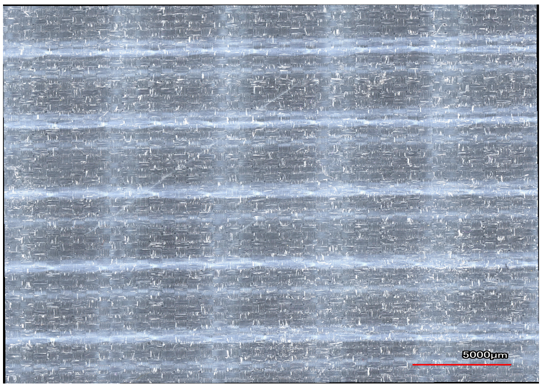

Figure 4.16: Matrix crack a observed from back of the sample under Keyence VK-1000x Laser Microscope for sample after 10 impacts with an 18mm SHI at 140 m/s

From Figure 4.16, white striations at an oblique 45° angle are evident on the rear side of the composite Sample impacted with an 18mm SHI at 140 m/s as it is above FTE limit, showing matrix cracking along the fibre direction from the 1^{st} impact. Images representative of the observed damage is provided in Appendix:B.

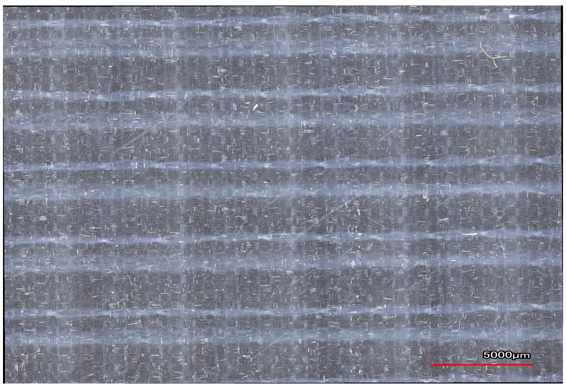

Figure 4.17: Matrix crack observed from the back of the sample under Keyence VK-1000x Laser Microscope impacted at 90 m/s with 20mm SHI(after 10 impacts)

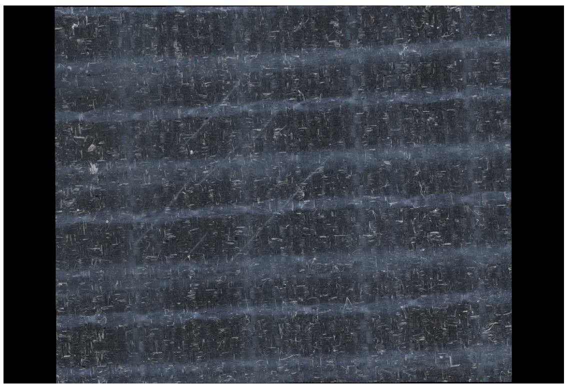

Figure 4.18: Matrix crack observed from the back of the sample under Keyence VK-1000x Laser Microscope impacted at 160 m/s with 15mm (after 10 impacts)

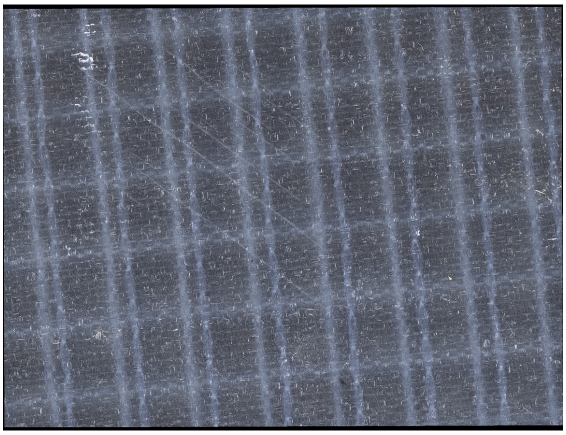

Figure 4.19: Sample A6 post 5th impact with a 18mm SHI at 140 m/s

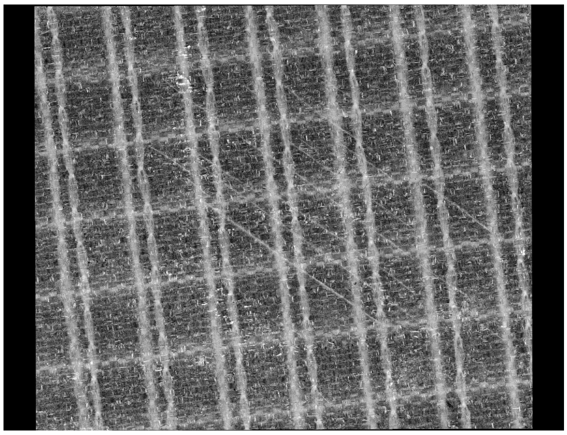

Figure 4.20: Sample A6 post 10th impact with a 18mm SHI at 140 m/s

The impact damages are generally barely visible to the naked eye. Therefore, it needs to be inspected using ultrasonic testing. The C-Scan images of the sample after the impact tests are shown in Appendix:C. Sample B10 displayed presence voids(black spots), but there were no signs of apparent delamination. Comparing Figure4.11 and Figure4.12, no clear evidence suggests the voids delineated into a matrix crack because of the impacts. Overall most of the samples did not display any presence of voids or delaminations. As described in the preceding section, matrix cracks in the 45° direction were observed in specific samples when viewed from behind. Similar Observations were made by Savana [56] for composites coated with polyurethane coating.

Next, the presence of the said matrix cracking, as observed in Figure 4.18, must be further verified using cross-section microscopic analysis. For this purpose, a sample from each velocity and the corresponding SHI size is taken for damage analysis. Transverse and longitudinal cracks in the sample were observed under coaxial light settings. Figure 4.21 shows the cross-section of sample B6, which has been impacted ten times with a 15 mm SHI (maximum impact velocity of 160 m/s).

Eight matrix cracks can be seen in the lowermost layer. An Image of higher magnification is captured and shown as images in the same Figure 4.21nalysing the images further, the cracks seem to initiate in the resin-rich region and fibre bundle layer. An interesting feature was visible in most samples. This was the presence of longitudinal matrix cracks. The Figure D.4 shows similar matrix cracks in the fibre bundle and the resin-rich zone. Longitudinal cracks were seen in both cases and were detected in the non-crimp fabric layer(not highlighted in b6 but are visible near the coating layer. This feature has been seen in many samples at the impacted side 45° layer and non-impacted side 45° layer.

In Figure D.4, a similar unique observation as observed earlier in case 15 mm SHI impact was noted. The longitudinal matrix crack initiated in the resin-rich region nucleating along the edge fibre matrix interface slowly turns in a transverse direction to transition into the transverse crack.

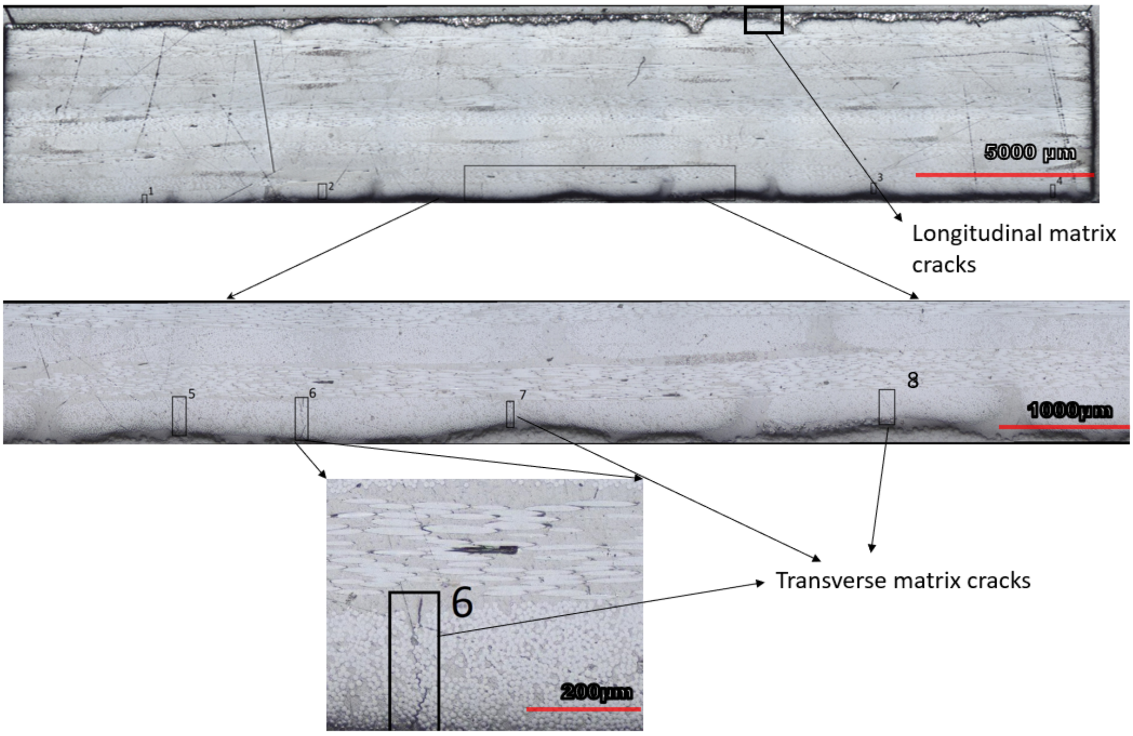

Figure 4.21: A step by step high resolution image of the matrix crack observed in sample B6 impacted with 15mm SHI at 160m/s

SHI Size	Impact Velocity	Observation
15 mm	140 m/s	no matrix cracks was observed
15 mm	150 m/s	Longitudinal cracks appear near the coating in the top ply and bottom ply accompanied by transverse cracking in the bottom ply
15 mm	160 m/s	Several transverse racks where observed
18 mm	120 m/s	Longitudinal cracks in top ply and bottom ply along with transverse crack (barely visible)
18 mm	110 m/s	Longitudinal cracks in top ply and bottom ply along with transverse crack
18 mm	100 m/s	Longitudinal cracks in top ply and bottom ply along with a possible longitudinal matrix crack transitioning to a transverse crack at the bottom
20 mm	90 m/s	Longitudinal cracks in bottom ply along with transverse crack

Table 4.4: Damage observation at microstructure level

4.2. Discussion

4.2.1. Impact test

Kim et al. [47] proposed to impact the sample at a velocity slightly lower than the expected velocity at which delamination occurred and then test at a higher velocity until delamination was noted. In this study, matrix cracks was the initial mode of failure. The FTE in this study refers to the energy required to initiate matrix cracking. Kim et al. [46] also found through numerical analysis that the FTE is related to the interlaminar shear strain energy at the contact region between the panel and the SHI. This was used to normalize the FTE and plot it against the ratio of panel thickness and SHI diameter (Figure 2.11). This approach could be particularly useful when testing panels of different thicknesses and subsequently, design a panel to be resistant to hail impact.However, In this study the sample thickness and coating remained constant and normalisation would not be necessary. A simple plot between FTE and SHI mass was plotted based on the kinetic energy required to initiate damage for each SHI size and velocity. For this research, it was deemed to be suitable enough to compare FTE with various SHI masses and average impact velocities.

The plot between FTE and SHI mass (Figure 4.2) showed scattering in data for 15mm, 18mm and 20 mm SHI. From Figure 4.2, it is visible that SHI diameter does not seem to have an effect on FTE. This is counter-intuitive to the hypothesis stated in Section 2.7. This discrepancy can be attributed to the small difference between the SHI sizes as well as the inaccuracies in the mass measurement due to the environmental sensitivity of SHI, which could not help significantly indicate the effect of SHI size on FTE . However, When mass loss due to melting was determined using basic heat transfer by considering conduction and convection between the SHI and its surroundings inside the barrel, the FTE was found to be increase for varying SHI masses as shown in Figure 4.3 in accordance to findings of kim et al [47]. This also confirms that the findings stand true even if the difference between the hailstones diameters are not very large.

Figure 4.2 and Figure 4.3 is obtained from analytical E_k (Equation 3.5), where the experimental values where used as requisite variable in equation. This is because a smaller SHI with less mass would require more velocity to generate sufficient energy to generate damage as compared to large SHI. This low kinetic energy generated is acting over smaller area for smaller SHI thereby requiring less energy to imitate damage. The Figure 4.3 shows that there is linear relation between FTE and mass of the SHI. So, when the mass increases the FTE also increases as the energy required to initiate damage due to larger contact area increases. This finding is supported by the fact by considering Figure 4.4, that the 20 mm SHI required only 90 m/s to initiate damage as compared to 15 mm SHI which required atleast 150 m/s to initiate damage. Similarly, From Figure 4.4, it is clear that there exist an inverse linear relation between kinetic energy and velocity. The velocity is required to initiate damage is low for SHI will large mass or diameter, while smaller SHI require more velocity to generate sufficient energy to initiate damage. Figure 4.4 showed that when the melting was taken into consideration, the FTE decreased for increasing velocities as less energy is required for smaller SHI.

In Sample B7 impacted with 15mm SHI at 150m/s, showed a delayed appearance of matrix cracks. This was an interesting occurrence as the 1^{st} SHI impact generated kinetic energy of 18.5 J which was higher than energies measured for the subsequent 3 impacts. But the striation only appeared after 2^{nd} impact with the estimated kinetic energy of 16.64 J. There is no clear way to examine the cause of the delay as they would require destructive testing methods. It can be speculated that the damage generated was not large enough to be observed by visual observation. The damage could have progressed and reached a size at which the damage could be observed by visual observation in subsequent impacts.

The kinetic energy is determined as the driving force for the mode of failure in the composites. This can be determined by observing the damage modes across the different SHI sizes and velocities. Though impact energy was not significant enough for the damage to transition to other damage modes making it hard to quantify the severity, the observed damage mode was sufficient enough to visually observe the significance in terms of crack intensity or number of cracks to indicate the effect of size of the SHI. The effect of size was measured across similar kinetic energy; the qualitative analysis of the available data makes it hard to correlate the impact of SHI on damage evolution. This study showed that the size of SHI indeed had an influence on the FTE of the gelcoated sample as they are influenced by the contact area. This is in agreement with the hypothesis and also suggests that even a small change in contact could have an effect on FTE. into the severity of damage or the longitudinal cracks that could be observed for SHI impact. So the damage zone is more important.

From the impact test, it is clear that the smaller SHI required less energy to initiate damage compare to larger SHI which is in agreement with the hypothesis. IT is also worth nothing that the sensitive nature of ice to temperature which would need to be accounted for or test parameters would need to be adjusted in accordance to climate so that test results are not affected.

4.2.2. Damage Analysis

The C-Scan images cannot capture matrix cracks due to the wavelength of the C-scan, which is way larger than the dimension of the crack. However, it does provide some information about the adhesion strength between the coating and substrate. The absence of any delamination or debonding which could be observed in the case of Polyurethane coating when impacted with 20 mm SHI as observed by Savana et al [56] indicates that there is a strong adhesion between the substrate and coating which could survive impact with utmost certainty for 20mm SHI upto 90 m/s. The literature review in section 2.2 suggested delamination as the initial failure mode. But several studies, including Eryörük [17] and Choi et al.[50], observed matrix cracking as the initial failure mode for low velocities. These results suggest that a sufficient amount of kinetic energy is needed to generate delamination, which this study did not achieve. The results observed also agree with damage modes observed by Savana [56] though the coating materials are different. The minimum energy required for delamination would differ for different SHI sizes. This is represented in the Figure 4.22 provided by [63], clearly showing the relation between size and delamination energy. Delaminations as the initially observed mode of failure for composites impacted by SHI, with delaminations increasing with increasing contact force. Eryorük [17] observed that matrix cracking preceded delaminations at lower velocities for gelcoated GFRP samples impacted by 20 mm SHI. This provides the reasoning for why the kinetic energy generated by the SHI impact in the current research project is insufficient to cause delaminations. Changing either or both impact velocity and mass of the SHI could lead to delamination or greater damage, provided that delamination energy is reached for similar test parameters.

From Figure 4.15, It is evident that the height profile shows no sign of coating degradation. This indicates that the coating is resistant to the FTEs subjected by the transverse impacts on the coating surface. Similarly, all impacted samples did not show any signs of coating degradation. High impact velocity had little effect on the surface profile of the 15 mm, 18 mm, and 20 mm samples. It is speculated that the higher coating stiffness and strength protect it from any damage or changes to the surface profile [9].

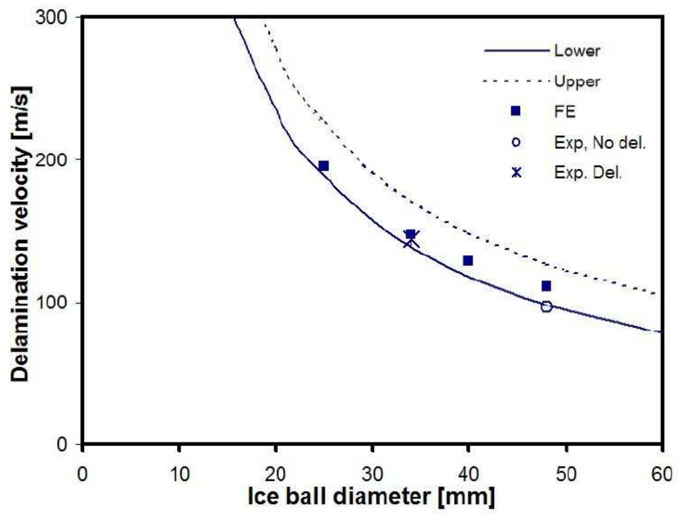

Figure 4.22: Expected delamination energy for different SHI diameters[63]

The cross-sections of the impacted samples were observed under high magnification to determine the failure mode. Cross-sectional observations confirmed the presence of transverse matrix cracks. The location of these cracks was found to be initiated from the lowermost 45° layer. The position of these cracks was noted to be away from the point of impact of the SHI, similar to the observations in section 4.1.2. This is in line with the observation and inference made by Savana[56] for the Offset of damage location. The appearance of the damage away from the impact point is probably due to high transverse stresses generated in the sample due to the impact [64]. On closer observation, the crack in transverse directions can be observed to have formed at the lowest ply. This crack is assumed to be initiated in the 45° between the resin-rich non-crimp fabric layer and propagated through the lowermost -45° fibre bundle. The matrix cracks travel through to the lowermost fibre bundle and reach the interface of the -45° and 45° layer.

Eight matrix cracks can be seen in the lowermost layer. An image of higher magnification is captured and shown as images in the same Figure 4.21.Analysing the images further, the cracks seem to initiate in the resin-rich region and fibre bundle layer. An interesting feature was visible in a few samples. This was the presence of longitudinal matrix cracks. Figure D.4 shows similar matrix cracks in the fibre bundle and the resin-rich zone. Longitudinal cracks were seen in both cases and were detected in the non-crimp fabric layer(not highlighted in the sample impacted 15mm SHI at 160 m/s but are visible near the coating layer). This feature has been seen in many samples at the outermost 45° layer and innermost 45° layer. The longitudinal cracks are speculated to initiate at the interface of the fibres and matrix in intralaminar region. The longitudinal cracks observed may be part of concentric cracks generated by the shear stress waves generated by the SHI impact. [1].

Comparing the cross-sections in Figure 4.21 and Figure D.1, a relatively significant amount of matrix cracks (8 cracks) were observed in sample impacted by 15mm SHI at average velocities of 160 m/s. In comparison, the cross-section of a sample, which was impacted at an average velocity of 150 m/s with a similar 15mm SHI, reveals a single transverse matrix crack near the middle (Figure D.1). Such a judgement can be made based on observation from the images alone. This demonstrates that the impact energy delivered by SHI significantly affects the level of damage. In terms of the position of the matrix crack(i.e close to the impact zone) and the layer(i.e innermost 45° layer) in which it is found, all of the samples displayed in Appendix D are uniform. The transverse cracks are exclusive to the innermost layer(last layer) and are absent from the other $\pm45^{\circ}$. These cracks always tend to initiate the inner edge (non-coated side) and traverses towards to midplane of the composite. The impact of the SHI, as explained in the section 2.3, generates three stress waves: rayleigh, compressive and shear waves. The shear stress generated by the SHI impact and the fibre layers beneath the neutral axis is in tension when SHI-induced bending of the composite panel is considered. This would generate significant shear stress in the lowest layer, the 45° layer). This could be why transverse cracks develop only in the bottom layer.

In Figure D.4, the longitudinal matrix cracks were observed. In several papers, the longitudinal cracks were seen at step of damage evolution of the transverse matrix cracks and just before delaminations. It is possible for delamination to occur at regions where these cracks could branch and evolve into delaminations [65]. It is also possible for the delamination to be initiated at the location where the longitudinal and transverse cracks branch into each other. Further, Juntikka et al. [63] suggest the possibility of the onset of delamination affected by the matrix cracks. Therefore it is necessary to understand the mechanism of the failure mode of both matrix cracks and how they induce delamination [66].

Kohler et al [67] suggested that interlaminar shear and normal stresses would be required to induce delamination growth. This same concept can be extended to longitudinal cracks, as their mechanisms are similar to delamination. These longitudinal cracks are generated by the compressive stress waves reflected back from the bottom ply and are turned into tensile stress waves, in addition to shear stresses generated by the bending of the composite due to impact cause large stresses between intra-plies leading to longitudinal cracks, which might further develop into more severe damage forms such as delaminations. The spherical nature of SHI means the waves generated would also be spherical so that ring cracks could plausibly be generated. It would be visible as longitudinal cracks when observed under a cross-sectional view. These longitudinal cracks occur at energies above critical energy (i.e FTE). Although there is no clear evidence, the intensity of longitudinal cracks seems to be affected by SHI diameters based on qualitative microscopic observations alone. The intensity of the longitudinal cracks seems to be more severe in the case of 18 mm SHI compared to 15mm SHI. This could be due to the large intensity of stress waves generated by larger SHI. This uncertainty also stems from the lack of evidence of such behaviour occurring in 20 mm SHI, probably due to the lack of sampling size to obtain a clear conclusion. Characterisation of the cracks in the visible cross-sections was difficult due to the small nature of cracks and other limitations. However, it can be speculated based on microscopic observations alone that the severity of the damages observed seems to be affected by SHI diameter and impact. It could be that the intensity of shear waves generated by SHI impact could be affected by the mass/size of SHI and velocity.

Several studies suggest that transverse cracks play a more significant role in the degradation of stiffness than longitudinal cracks [68] [65]. It is also predicted that delamination might initiate at the region where the longitudinal crack[66] and transverse cracks co-joined. No evidence exists that such a phenomenon may be observed for impact damage. For the number of matrix cracks observed in these samples, it is anticipated not to impair the composite's structural performance[68]. Despite these matrix cracks, the composite should withstand most of the loads for which it was designed. But the cracks could diminish the stiffness over time. The performance may be compromised if these cracks migrate towards the coating and develop fractures on the layer. This coupled with precipitation, might result in significant leading-edge erosion. Therefore it may be best to conduct routine maintenance or inspections.

5 Conclusion

This research project has examined the influence of kinetic energy on the damage generated in gelcoated glass fibre-reinforced polymer composite. The damage generated by different hailstones for different velocities was studied using a gas canon facility at the Delft Aerospace Structures and Materials Laboratory (DASML). The effect of hailstone size and kinetic energy were studied for 15mm hailstone at impact velocities of 140 m/s, 150 m/s and 160 m/s; for 18mm hailstone, the impact velocities used were 100 m/s,110 m/s,120 m/s and 140 m/s, and 20mm hailstone was impacted at 90m/s. Calibration tests were conducted to determine the pressure values for the corresponding impact velocities for the various hailstone sizes considered in this study. Several characterisation tests, such as non-contact profilometry, optical microscopy and cross-sectional analysis, were conducted to evaluate the damage generated due to the impact on the composite. The information from this research can be used in design optimisation to customise the composites or layup thickness. Based on literature and experiment results, with the increasing average size of hailstones, The observations and results have helped answer the main research question and a few sub-questions set out in Section 2.7. The sub-questions are discussed before answering the main research question.

- ”How does the kinetic energy affect the damage generated in gelcoated composite?”

Kinetic energy is one of the parameters affecting mechanism of hailstone impact according literature. Kinetic energy is dependent on the mass of the hailstone and its impact velocity. Based on test results and finding in literature, it can be hypothesised that damage mode is a function of kinetic energy. This claim can be further strengthened by comparing the major damage mode across all samples impacted with hailstones of different sizes affected at similar kinetic energies. Though the severity of damage varied across a range of kinetic energies, the initial mode of failure has always been matrix cracking. However, further experimentation and verification at higher velocities would be required to obtain different damage modes for better understanding.

Comparing the different sizes and various impact velocities showed no change in the damage mode. The lack of change in damage mode shows that neither parameter alone has a significant effect on damage mode. This is further confirmed, when larger hailstones were impacted at lower velocities to get similar kinetic energies to smaller hailstones at larger velocities.

- "How does the size of hailstone affect the FTE in gelcoated composite?"

In the earlier part of the report, it was hypothesised that smaller hailstones would require less energy to initiate damage due to a smaller contact area on impact. The results of this work are in agreement with the hypothesis as the size of the hailstone does seem to have a significant effect on the FTE of the gelcoated sample, as it is more a function of the contact area of the hailstone with regards to the surface. The FTE was found to increase with increasing hailstone sizes as the contact area for 15mm is smaller than the contact area of 18mm and 20 mm hailstones, thereby requiring lesser energy to initiate damage, which agrees with the hypothesis.

Based on these findings. The main research can be answered
" How does the size of hailstone and its kinetic energy affect the mode of damage in gelcoats?"
The Kinetic energy is determined as the driving force for the mode of failure in the composites. However, for the kinetic energies observed (both non-corrected and corrected FTE) the damage mode was matrix crack (transverse and longitudinal) across the different hailstone sizes and velocities.

The effect of size was studied across similar kinetic energy; the qualitative analysis of the available data makes it hard to correlate the impact of hailstone on damage evolution. This study showed that hailstone size indeed has an influence on the energy required to initiate damage due to its contact area. During experimentation, sensitivity to temperature on the FTE was attributed and was known to affect the test data.

The size of hailstone in this study is shown to affect damage severity based on qualitative microscopic observation. However, substantiating this claim quantitatively is difficult due to the inherent drawbacks of cross-sectional analysis, resulting in an unreliable crack density estimation due to damage modes observed. Nevertheless, the damage severity is more significant for larger hailstones based on qualitative microscopic observation, even though FTE are close to each other for all the hailstones. The longitudinal cracks observed were more severe for 18mm hail impacts than for 15mm hailstones. The limited sampling size for 20mm hailstones does not offer much insight into the severity of damage or the longitudinal cracks that could be observed.

The transverse matrix cracks appear in the lowermost 45° fibre bundle and are speculated to be due to the bending of the panels, while longitudinal cracks in the outermost impacted and non-impacted non-crimp fabric layer of the composite, it is further hypothesised that the intralaminar shear stress generated by the bending of composites due to hail impact causes to cracks to initiate at fibre matrix interface and propagate along the intralaminar region.

The test conducted on the gelcoated composites shows that for a limited number of impacts (ten impacts), it was found to have little or no effect on the FTE. Within this Study. The damage initiation was found to be more dependent on the kinetic energy of the hail impact rather than the number of impacts However, as far as damage evolution is concerned, both the number of impacts and the kinetic energy of the impact play a crucial role. Overall, these results enable us to further understand the influence of individual parameters on the damage evolution due to hail impacts.

6 Recommendations

The main goal of this research was to study how parameters like kinetic energy and size of hailstone affect the evolution of damage in a leading edge of a gelcoated composite. One of the research goals was to see how kinetic energy affected the damage evolution over a period of multiple impacts over a single point. As observed throughout the literature, the damage initiation occurs at higher energies for larger hailstones. But the large hailstones would be very rare in real life, and damage to evolution would not be seen over a prolonged lifetime.

However, there is a need to understand the effect of damage evolution at different velocities for different hailstone sizes, along with the percentage of kinetic energy being transmitted into the sample and the portion of kinetic energy stored in the sample after each impact.

The information from this research can be used in design optimisation to customise the composites or layup thickness.

Based on Literature and Experiment results, with the increasing average size of hailstones, it may be advisable to go with thinner plies as they are much more flexible and can observe more impact energies.

Further, based on the hailstone distribution, the operation speed can be controlled to reduce impact velocity and significantly lower FTE during hail events. These results and existing literature also show a need to determine an optimal gelcoat thickness as they exhibit brittle nature for higher thickness. But offer low or no protection to the substrate at a very small thickness.

A high-speed camera with a higher frame rate would help improve the velocity measurement accuracy. Also, it was observed that hailstones were hard to track due to hailstone's transparent nature. This issue could be resolved by using a dyed hailstone or changing the background colour to improve the contrast.

Another important aspect of hail erosion would be to study how the damage modes would be affected after the coated samples had been exposed to UV radiation. Comparative study of damage evolution of a coated sample exposed to UV radiation and coated sample unexposed to UV radiation. It would also be interesting to study the effect of radiation on coating thickness and how that affects the erosion performance of coatings.

Additionally, with the existing test setup, the effect of multiple impacts is unknown mainly due to the uneven time intervals between impacts, which is a drawback. There is a need to develop a setup capable of producing multiple impacts within an equal interval which enables to study of the effect of hail erosion.

The lack of temperature controlled environment causes a discrepancy in the measured mass of hailstone before impact and the mass of hailstone on impact. This becomes a major problem of concern during summer. This issue can be avoided by providing a controlled environment so the external weather does not affect the results.

Through this thesis, difficulty in identifying the small matrix cracks where evident, making an accurate determination of the FTE a tedious task. With technological developments, there is a need to identify and develop new methods or improve the efficacy of existing methods to observe matrix cracking other than destructive techniques. Though matrix cracks are not detrimental to structural integrity, early identification of matrix cracks can improve blade life by carrying out preventive maintenance before severe debilitating damage occurs.

References

[1] Mark Hugh Keegan. *Wind Turbine Blade Leading Edge Erosion: An investigation of rain droplet and hailstone impact induced damage mechanisms | Enhanced Reader*. 2014. URL: https://pureportal.strath.ac.uk/en/publications/wind-turbine-blade-leading-edge-erosion-an-investigation-of-rain.

[2] T. F. Brooks et al. “Scaling of airfoil self-noise using measured flow parameters”. In: *AIAAJ* 23 (2 1985), pp. 207–213. ISSN: 0001-1452. DOI: 10.2514/3.8896. URL: https://ui.adsabs.harvard.edu/abs/1985AIAAJ..23..207B/abstract.

[3] Luis Bartolomé and Julie Teuwen. “Prospective challenges in the experimentation of the rain erosion on the leading edge of wind turbine blades”. In: *Wind Energy* 22 (1 Jan. 2019), pp. 140–151. ISSN: 1099-1824. DOI: 10.1002/WE.2272. URL: https://onlinelibrary-wiley-com.tudelft.idm.oclc.org/doi/full/10.1002/we.2272.

[4] IRENA. *Renewable Energy Statistics 2018*. 2018. URL: https://irena.org/publications/2018/Jul/Renewable-Energy-Statistics-2018.

[5] IRENA. *Renewable Energy Statistics 2019*. 2019. URL: https://www.irena.org/publications/2019/Jul/Renewable-energy-statistics-2019.

[6] IRENA. *Renewable energy statistics 2020*. 2020. URL: https://www.irena.org/publications/2020/Jul/Renewable-energy-statistics-2020.

[7] IRENA. *Renewable energy statistics 2021*. 2021. URL: https://irena.org/publications/2021/Aug/Renewable-energy-statistics-2021.

[8] Lisa Rempel. “ROTOR BLADE LEADING EDGE EROSION-REAL LIFE EXPERIENCES”. In: *Wind Systems Magazine* (2012), pp. 22–24. URL: www.completewind.com.

[9] Olive G Engel. “Erosion Damage to Solids Caused by High-Speed Collision With Rain *”. In: *Journal of Research of the National Bureau of Standards* 61 (1 1958).

[10] Leon Mishnaevsky and Jan Sütterlin. “Micromechanical model of surface erosion of polyurethane coatings on wind turbine blades”. In: *Polymer Degradation and Stability* 166 (Aug. 2019), pp. 283–289. ISSN: 0141-3910. DOI: 10.1016/J.POLYMDEGRADSTAB.2019.06.009.

[11] IEA. *Technology Roadmap - Wind Energy 2013 – Analysis - IEA*. 2013. URL: https://www.iea.org/reports/technology-roadmap-wind-energy-2013.

[12] N. Gaudern, Gaudern, and N. “A practical study of the aerodynamic impact of wind turbine blade leading edge erosion”. In: *JPhCS* 524 (1 2014), p. 012031. ISSN: 1742-6596. DOI: 10.1088/1742-6596/524/1/012031. URL: https://ui.adsabs.harvard.edu/abs/2014JPhCS.524a2031G/abstract.

[13] Agrim Sareen, Chinmay A. Sapre, and Michael S. Selig. “Effects of leading edge erosion on wind turbine blade performance”. In: *Wind Energy* 17 (10 Oct. 2014), pp. 1531–1542. ISSN: 1099-1824. DOI: 10.1002/WE.1649. URL: https://onlinelibrary-wiley-com.tudelft.idm.oclc.org/doi/full/10.1002/we.1649.

[14] Ryan Wiser et al. *Forecasting wind energy costs and cost drivers: the views of the world’s leading experts*. 2016. URL: https://escholarship.org/content/qt0s43r9w4/qt0s43r9w4.pdf.

[15] WTG-Offshore. “Blade leading edge erosion: damage limitation, containment and prevention”. In: *Power & Energy Solution Talk point* (2018), pp. 1–3. URL: https://pes.eu.com/wind/blade-leading-edge-erosion-damage-limitation-containment-and-prevention/.

[16] Timothy H. Raupach et al. “The effects of climate change on hailstorms”. In: *Nature Reviews Earth & Environment 2021 2:3* 2 (3 Feb. 2021), pp. 213–226. ISSN: 2662-138X. DOI: 10.1038/S43017-020-00133-9. URL: https://www-nature-com.tudelft.idm.oclc.org/articles/s43017-020-00133-9.

[17] Huseyin Eryörük. “Effects of gelcoat thickness on damage resistance of leading edge gelcoated glass fibre composite subjected to hailstone impact”. In: (2021). URL: https://repository.tudelft.nl/islandora/object/uuid%3Abec72336-20ff-4409-8fd3-4b61072b0bd6.

[18] Leon Mishnaevsky et al. “Materials for Wind Turbine Blades: An Overview”. In: *Materials 2017, Vol. 10, Page 1285* 10 (11 Nov. 2017), p. 1285. ISSN: 19961944. DOI: 10.3390/MA10111285. URL: https://www.mdpi.com/1996-1944/10/11/1285/htm.

[19] Vipin Kumar Singh, Tiju Thomas, and Vilas Warudkar. *Structural design of a wind turbine blade: A review*. 2013. URL: https://www.researchgate.net/publication/287755001_Structural_design_of_a_wind_turbine_blade_A_review.

[20] Enrique Cortés et al. “On the Material Characterisation of Wind Turbine Blade Coatings: The Effect of Interphase Coating–Laminate Adhesion on Rain Erosion Performance”. In: *Materials* 10.10 (2017). ISSN: 1996-1944. DOI: 10.3390/ma10101146. URL: https://www.mdpi.com/1996-1944/10/10/1146.

[21] Dylan S. Cousins et al. “Recycling glass fiber thermoplastic composites from wind turbine blades”. In: *Journal of Cleaner Production* 209 (Feb. 2019), pp. 1252–1263. ISSN: 0959-6526. DOI: 10.1016/J.JCLEPRO.2018.10.286.

[22] Leon Mishnaevsky et al. “Leading edge erosion of wind turbine blades: Understanding, prevention and protection”. In: *Renewable Energy* 169 (May 2021), pp. 953–969. ISSN: 0960-1481. DOI: 10.1016/J.RENENE.2021.01.044.

[23] ERZ. *“The centre of a large hailstone with alternate layers of opaque and transparent ice*. May 2008. URL: https://en.wikipedia.org/wiki/Hail#/mediamo/File:Hagelkorn_mit_Anlagerungsschichten.jpg.

[24] P.R. Field et al. *”Hail Threat Standardisation ”*. 2008. URL: https://www.easa.europa.eu/en/document-library/research-reports/easarepresea20085.

[25] M. H. Keegan, D. H. Nash, and M. M. Stack. “On erosion issues associated with the leading edge of wind turbine blades”. In: *Journal of Physics. D, Applied Physics* 46 (38 Sept. 2013). ISSN: 00223727. DOI: 10.1088/0022-3727/46/38/383001.

[26] Hamish Macdonald. “The infuence of hail on wind turbine blade leading edge erosion and damage”. In: (2017). DOI: 10.48730/TDZW-QT13. URL: https://doi.org/10.48730/tdzw-qt13.

[27] ESWD. *European Severe Weather Database*. 2022. URL: https://eswd.eu/cgi-bin/eswd.cgi.

[28] Tomas Pucik. *Hailstorms of 2021 | European Severe Storms Laboratory*. 2021. URL: https://www.essl.org/cms/hailstorms-of-2021/.

[29] Erland M. Schulson. “The brittle failure of ice under compression”. In: *Journal of Physical Chemistry B* 101 (32 Aug. 1997), pp. 6254–6258. ISSN: 15206106. DOI: 10.1021/JP9632192/ASSET/IMAGES/LARGE/JP9632192F00003.JPEG. URL: https://pubs-acs-org.tudelft.idm.oclc.org/doi/full/10.1021/jp9632192.

[30] Victor F. Petrenko and Robert W. Whitworth. “Physics of Ice”. In: *Physics of Ice* (Jan. 2010). DOI: 10.1093/ACPROF:OSO/9780198518945.001.0001.

[31] Kelly S. Carney et al. “A phenomenological high strain rate model with failure for ice”. In: *International Journal of Solids and Structures* 43 (25-26 Dec. 2006), pp. 7820–7839. ISSN: 0020-7683. DOI: 10.1016/J.IJSOLSTR.2006.04.005.

[32] Mostafa Shazly, Vikas Prakash, and Bradley A. Lerch. “High strain-rate behavior of ice under uniaxial compression”. In: *International Journal of Solids and Structures* 46 (6 Mar. 2009), pp. 1499–1515. ISSN: 0020-7683. DOI: 10.1016/J.IJSOLSTR.2008.11.020.

[33] R Telling, G Jilbert, and J Field. “Erosion of aerospace materials by solid-particle impact”. In: *https://doi-org.tudelft.idm.oclc.org/10.1117/12.277065* 3060 (June 1997), pp. 56–67. DOI: 10.1117/12.277065. URL: https://www-spiedigitallibrary-org.tudelft.idm.oclc.org/conference-proceedings-of-spie/3060/0000/Erosion-of-aerospace-materials-by-solid-particle-impact/10.1117/12.277065.full.

[34] F. P. Bowden and J. Field. “The brittle fracture of solids by liquid impact, by solid impact, and by shock”. In: *undefined* 282 (1390 Nov. 1964), pp. 331–352. ISSN: 0080-4630. DOI: 10.1098/RSPA.1964.0236.

[35] I. V. Roisman and C. Tropea. “Impact of a crushing ice particle onto a dry solid wall”. In: *Proceedings of the Royal Society A: Mathematical, Physical and Engineering Sciences* 471 (2183 Nov. 2015). ISSN: 14712946. DOI: 10.1098/RSPA.2015.0525. URL: https://royalsocietypublishing.org/doi/10.1098/rspa.2015.0525.

[36] Georgia State University. *Fluid Friction*. URL: http://hyperphysics.phy-astr.gsu.edu/hbase/airfri2.html.

[37] Arnett Dennis. “Weather Modification by Cloud Seeding”. In: *International Geophysics Series* 24 (Jan. 1980). URL: https://digitalcommons.usu.edu/water_rep/670.

[38] Andrew J. Heymsfield, Ian M. Giammanco, and Robert Wright. “Terminal velocities and kinetic energies of natural hailstones”. In: *Geophysical Research Letters* 41 (23 Dec. 2014), pp. 8666–8672. ISSN: 1944-8007. DOI: 10.1002/2014GL062324. URL: https://onlinelibrary-wiley-com.tudelft.idm.oclc.org/doi/full/10.1002/2014GL062324.

[39] Ross Gunn and Gilbert D. Kinzer. “The Terminal Velocity Of Fall For Water Droplets In Stagnant Air”. In: *Journal of Atmospheric Sciences* 6.4 (1949), ”243 –248”. DOI: 10.1175/1520-0469(1949)006<0243:TTVOFF>2.0.CO;2. URL: "https://journals.ametsoc.org/view/journals/atsc/6/4/1520-0469_1949_006_0243_ttvoff_2_0_co_2.xml".

[40] ASTM. *Standard Test Method for Hail Impact Resistance of Aerospace Transparent Enclosures*. 2005. URL: https://www-astm-org.tudelft.idm.oclc.org/f0320-05.html.

[41] Srinivasan Ganesh Ram. “Can Hail Impacts Trigger Delaminations?: A qualitative study to evaluate the consequences of hail ice impact on composite structures.” In: (2021). URL: https://repository.tudelft.nl/islandora/object/uuid%3A8d09838f-8c0d-4329-804a-f89798928d31.

[42] Yiheng Zhang et al. “Dynamic splitting tensile behaviours of distilled-water and river-water ice using a modified SHPB setup”. In: *International Journal of Impact Engineering* 145 (Nov. 2020), p. 103686. ISSN: 0734-743X. DOI: 10.1016/J.IJIMPENG.2020.103686.

[43] Zhongbin Tang et al. “Numerical and experimental investigation on hail impact on composite panels”. In: *International Journal of Impact Engineering* 105 (2017). Design and Analysis of Protective Structures 2015, pp. 102–108. ISSN: 0734-743X. DOI: https://doi.org/10.1016/j.ijimpeng.2016.05.016. URL: https://www.sciencedirect.com/science/article/pii/S0734743X16303050.

[44] Fiore G., Fujiwara G. E. C, and M. S. Selig. “A damage assessment for wind turbine blades from heavy atmospheric particles.” In: *53rd AIAA Aerospace Sciences Meeting,AIAA SciTech* (2015), pp. 1495–1507.

[45] Hiroshi Saito et al. “Effect of ply-thickness on impact damage morphology in CFRP laminates”. In: *Journal of Reinforced Plastics and Composites* 30 (13 July 2011), pp. 1097–1106. ISSN: 07316844.

[46] Hyonny Kim and Keith T. Kedward. “Modeling Hail Ice Impacts and Predicting Impact Damage Initiation in Composite Structures”. In: *AIAA Journal* 38 (7 July 2000), pp. 1278–1281. ISSN: 00011452. DOI: 10.2514/2.1099. URL: https://arc-aiaa-org.tudelft.idm.oclc.org/doi/10.2514/2.1099.

[47] Hyonny Kim, Douglas A. Welch, and Keith T. Kedward. “Experimental investigation of high velocity ice impacts on woven carbon/epoxy composite panels”. In: *Composites Part A: Applied Science and Manufacturing* 34 (1 Jan. 2003), pp. 25–41. ISSN: 1359-835X. DOI: 10.1016/S1359-835X(02)00258-0.

[48] Gareth J. Appleby-Thomas, Paul J. Hazell, and Gussan Dahini. “On the response of two commercially-important CFRP structures to multiple ice impacts”. In: *Composite Structures* 93 (10 Sept. 2011), pp. 2619–2627. ISSN: 0263-8223. DOI: 10.1016/J.COMPSTRUCT.2011.04.029.

[49] K. Azouaoui et al. “Modelling of damage and failure of glass/epoxy composite plates subject to impact fatigue”. In: *International Journal of Fatigue* 23 (10 Nov. 2001), pp. 877–885. ISSN: 0142-1123. DOI: 10.1016/S0142-1123(01)00050-0.

[50] Hyung Yun Choi and fu Kuo Chang. “A Model for Predicting Damage in Graphite/Epoxy Laminated Composites Resulting from Low-Velocity Point Impact”. In: 26 (14 July 2016), pp. 2134–2169. ISSN: 1530793X. DOI: 10.1177/002199839202601408. URL: https://journals-sagepub-com.tudelft.idm.oclc.org/doi/10.1177/002199839202601408.

[51] M.A. Eltaher, R. Alsulami, and A. Wagih. “On the evolution of energy dissipation in dispersed composite laminates under out-of-plane loading”. In: *Composites Part B: Engineering* 216 (2021), p. 108864. ISSN: 1359-8368. DOI: https://doi.org/10.1016/j.compositesb.2021.108864. URL: https://www.sciencedirect.com/science/article/pii/S1359836821002559.

[52] Cesim Atas, Bulent Murat Icten, and Mümin Küçük. “Thickness effect on repeated impact response of woven fabric composite plates”. In: *Composites Part B: Engineering* 49 (2013), pp. 80–85. ISSN: 1359-8368. DOI: https://doi.org/10.1016/j.compositesb.2013.01.019. URL: https://www.sciencedirect.com/science/article/pii/S1359836813000255.

[53] Hyonny Kim, J. Nightingale, and Hwun Park. “Impact Damage Resistance Of Composite Panels Impacted By Cotton-Filled And Unfilled Ice”. In: (2007). URL: https://www-semanticscholar-org.tudelft.idm.oclc.org/paper/IMPACT-DAMAGE-RESISTANCE-OF-COMPOSITE-PANELS-BY-AND-Kim-Nightingale/877f269cbdc2bac657ccb8d4e6f3589a927433e7.

[54] Sh Dolati, A. Fereidoon, and A. R. Sabet. “Hail impact damage behaviors of glass fiber reinforced epoxy filled with nanoclay”. In: *Journal of Composite Materials* 48 (10 Apr. 2014), pp. 1241–1249. ISSN: 1530793X. DOI: 10.1177/0021998313484950/ASSET/IMAGES/LARGE/10.1177_0021998313484950-FIG2.JPEG. URL: https://journals-sagepub-com.tudelft.idm.oclc.org/doi/full/10.1177/0021998313484950?casa_token=jrpUrYWl7k8AAAAA%3AJdaYgFZ8cwvduz1Rvp1PqB5pRiK_FmBZXpmXkUvxOgWyEU7COjjpoEtSlzw6g9EWVEUL_QtP8-PzTw.

[55] Xinying Zhu et al. “Damage mechanism of composite laminates under multiple ice impacts at high velocity”. In: *International Journal of Impact Engineering* 168 (Oct. 2022), p. 104296. ISSN: 0734-743X. DOI: 10.1016/J.IJIMPENG.2022.104296.

[56] Reshab Savana. “Effect of Hail Impact on Leading Edge Polyurethane Composites”. In: (2022). URL: https://repository.tudelft.nl/islandora/object/uuid%3Aa2976e84-b359-4b78-a907-ca7c0abb7353.

[57] ASTM. *Standard Test Method for Hail Impact Resistance of Aerospace Transparent Enclosures*. 2021. URL: https://www-astm-org.tudelft.idm.oclc.org/f0320-21.html.

[58] Yunus A. Çengel and Afshin J. (Afshin Jahanshahi) Ghajar. *Heat and mass transfer : fundamentals & applications*. Mcgraw Hill Education, 2020. ISBN: 0073398195.

[59] Tatsunori Asaoka et al. "Effect of temperature on the effective latent heat of fusion of ice in aqueous solutions". In: *International Journal of Refrigeration* 33 (8 Dec. 2010), pp. 1533–1539. ISSN: 0140-7007. DOI: 10.1016/J.IJREFRIG.2010.02.009.

[60] Philip Kosky et al. "Mechanical Engineering". In: *Exploring Engineering* (Jan. 2021), pp. 317–340. DOI: 10.1016/B978-0-12-815073-3.00014-4. URL: https://linkinghub.elsevier.com/retrieve/pii/B9780128150733000144.

[61] Evgeny Chuvilin et al. "Effect of Ice and Hydrate Formation on Thermal Conductivity of Sediments". In: *Impact of Thermal Conductivity on Energy Technologies* (Mar. 2018). DOI: 10.5772/INTECHOPEN.75383. URL: https://www.intechopen.com/state.item.idundefined/state.item.id.

[62] Visual Crossing Corporation. *Weather history dashboard for Delft*. URL: https://www.visualcrossing.com/weather-history/Delft/metric/2022-08-14/2022-10-08.

[63] R. Juntikka and R. Olsson. "Experimental and modelling study of hail impact on composite plates". In: *ICCM* (2009).

[64] TK OBRIEN and W Elber. "Delamination and fatigue of composite materials: a review". In: *AGARD, Debonding/Delamination of Composites 11 p(SEE N 93-21507 07-24)* (1992).

[65] Jean Luc Rebière. "The initiation of transverse matrix cracking and longitudinal matrix cracking in composite cross-ply laminates: Analysis of a damage criterion". In: *Cogent Engineering* 3 (1). ISSN: 2331-1916. DOI: 10.1080/23311916.2016.1175060.

[66] J. E. Bailey, P. T. Curtis, and A. Parvizi. "On The Transverse Cracking And Longitudinal Splitting Behaviour Of Glass And Carbon Fibre Reinforced Epoxy Cross Ply Laminates And The Effect Of Poisson And Thermally Generated Strain." In: *Proc R Soc London Ser A* 366 (1727 1979), pp. 599–623. ISSN: 00804630. DOI: 10.1098/RSPA.1979.0071. URL: https://royalsocietypublishing.org/.

[67] S. Kohler et al. "Transverse cracking in the bulk and at the free edge of thin-ply composites: Experiments and multiscale modelling". In: *Composites Part A: Applied Science and Manufacturing* 124 (2019), p. 105468. ISSN: 1359-835X. DOI: https://doi.org/10.1016/j.compositesa.2019.05.036. URL: https://www.sciencedirect.com/science/article/pii/S1359835X19302118.

[68] Serge Abrate. "Matrix cracking in laminated composites: A review". In: *Composites Engineering* 1 (6 Jan. 1991), pp. 337–353. ISSN: 0961-9526. DOI: 10.1016/0961-9526(91)90039-U.

A

Test Data

S,no	Sample Id	SHI diameter (mm)	SHI mass (g)	corrected SHI mass (g)	Velocity (m/s)	Kinetic Energy (J)	corrected Kinetic Energy (J)	Observation
1	A2	15 mm	1,31	1,23	131,43	11,81	10,62	No Damage
2	A2	15 mm	1,45	1,37	137,14	13,64	12,88	No Damage
3	A2	15 mm	1,41	1,33	142,86	14,39	13,57	No Damage
4	A2	15 mm	1,53	1,45	142,86	15,61	14,80	No Damage
5	A2	15 mm	1,53	1,45	151,43,86	17,54	16,62	No Damage
6	A2	15 mm	1,45	1,37	145,71	15,39	14,54	No Damage
7	A2	15 mm	1,56	1,48	142,86	15,92	15,10	No Damage
8	A2	15 mm	1,41	1,33	142,86	14,39	13,57	No Damage
9	A2	15 mm	1,37	1,29	142,86	13,98	13,16	No Damage
10	A2	15 mm	1,66	1,66	142,86	16,94	13,94	No Damage

Table A.1: Sample A2 impacted with15mm SHI impacted at 140 m/s test results

S,no	Sample Id	SHI diameter (mm)	SHI mass (g)	corrected SHI mass (g)	Velocity (m/s)	Kinetic Energy (J)	corrected Kinetic Energy (J)	Observation
1	B8	15 mm	1,65	1,57	140	16,17	15,39	No Damage
2	B8	15 mm	1,65	1,57	148,57	18,21	17,33	No Damage
3	B8	15 mm	1,31	1,23	145,71	13,91	13,06	No Damage
4	B8	15 mm	1,35	1,27	142,86	13,78	12,96	No Damage
5	B8	15 mm	1,43	1,35	142,86	14,59	13,78	No Damage
6	B8	15 mm	1,47	1,39	145,71	15,61	14,76	No Damage
7	B8	15 mm	1,43	1,35	148,57	15,78	14,90	No Damage
8	B8	15 mm	1,63	1,55	142,86	16,63	15,82	No Damage
9	B8	15 mm	1,46	1,38	137,14	13,73	12,98	No Damage
10	B8	15 mm	1,59	1,51	145,71	16,88	16,03	No Damage

Table A.2: Sample B8 impacted with 15mm SHI impacted at 140 m/s test results

S,no	Sample Id	SHI diameter (mm)	SHI mass (g)	corrected SHI mass (g)	Velocity (m/s)	Kinetic Energy (J)	corrected Kinetic Energy (J)	Observation
1	B2	15 mm	1,48	1,40	142,86	15,10	14,29	No Damage
2	B2	15 mm	1,35	1,27	145,71	14,33	13,48	No Damage
3	B2	15 mm	1,31	1,23	148,57	14,46	13,58	No Damage
4	B2	15 mm	1,32	1,24	145,71	14,01	13,16	No Damage
5	B2	15 mm	1,52	1,44	142,86	15,51	14,69	No Damage
6	B2	15 mm	1,49	1,41	148,57	16,44	15,56	No Damage
7	B2	15 mm	1,50	1,42	145,71	15,92	15,08	No Damage
8	B2	15 mm	1,36	1,28	145,71	14,44	13,59	No Damage
9	B2	15 mm	1,48	1,40	148,57	16,33	15,45	No Damage
10	B2	15 mm	1,49	1,41	151,43	17,08	16,17	No Damage

Table A.3: Sample B2 impacted with15mm SHI impacted at 140 m/s test results

S,no	Sample Id	SHI diameter (mm)	SHI mass (g)	corrected SHI mass (g)	Velocity (m/s)	Kinetic Energy (J)	corrected Kinetic Energy (J)	Observation
1	B7	15 mm	1,58	1,50	157,14	19,51	18,52	No Damage
2	B7	15 mm	1,38	1,30	157,14	17,04	16,64	Matrix crack
3	B7	15 mm	1,34	1,26	151,43	15,36	15,00	Matrix crack
4	B7	15 mm	1,50	1,24	151,43	17,20	16,90	Matrix crack
5	B7	15 mm	1,16	1,08	151,43	13,30	12,85	Matrix crack
6	B7	15 mm	1,50	1,42	154,29	17,85	17,53	Matrix crack
7	B7	15 mm	1,51	1,43	160	19,33	18,96	Matrix crack
8	B7	15 mm	1,59	1,51	157,14	19,63	18,64	Matrix crack
9	B7	15 mm	1,54	1,46	151,43	17,66	17,38	Matrix crack
10	B7	15 mm	1,65	1,57	151,43	18,92	18,00	Matrix crack

Table A.4: Sample B7 impacted with 15mm SHI at 150 m/s test results

S,no	Sample Id	SHI diameter (mm)	SHI mass (g)	corrected SHI mass (g)	Velocity (m/s)	Kinetic Energy (J)	corrected Kinetic Energy (J)	
1	B3	15 mm	1,52	1,44	154,29	17,43	16,51	No damage
2	B3	15 mm	1,46	1,38	151,43	16,74	15,82	No damage
3	B3	15 mm	1,65	1,57	134,29	14,88	14,16	No damage
4	B3	15 mm	1,70	1,62	151,43	19,49	18,57	Matrix crack
5	B3	15 mm	1,63	1,55	151,43	18,69	17,77	Matrix crack
6	B3	15 mm	1,64	1,56	157,14	20,25	19,26	Matrix crack
7	B3	15 mm	1,61	1,53	151,43	18,46	17,54	Matrix crack
8	B3	15 mm	1,58	1,50	151,43	18,12	17,20	Matrix crack
9	B3	15 mm	1,48	1,40	151,43	16,97	16,05	Matrix crack
10	B3	15 mm	1,59	1,51	154,29	18,92	17,97	Matrix crack

Table A.5: Sample B3 impacted with 15mm SHI at 150m/s test results

S,no	Sample Id	SHI diameter (mm)	SHI mass (g)	corrected SHI mass (g)	Velocity (m/s)	Kinetic Energy (J)	corrected Kinetic Energy (J)	
1	B4	15 mm	1,55	1,47	157,14	19,14	18,15	No Damage
2	B4	15 mm	1,57	1,49	151,43	18,00	17,08	No Damage
3	B4	15 mm	1,49	1,41	154,29	17,73	16,78	No Damage
4	B4	15 mm	1,65	1,57	151,43	18,92	18,00	No Damage
5	B4	15 mm	1,62	1,54	145,71	17,20	16,35	No Damage
6	B4	15 mm	1,65	1,57	151,43	18,92	18,00	No Damage
7	B4	15 mm	1,42	1,34	154,29	16,90	15,95	No Damage
8	B4	15 mm	1,61	1,53	154,29	19,16	18,21	Matrix crack
9	B4	15 mm	1,48	1,40	157,14	18,27	17,29	Matrix crack
10	B4	15 mm	1,53	1,45	154,29	18,21	17,26	Matrix crack

Table A.6: Sample B4 impacted with 15mm SHI at 150m/s test results

S,no	Sample Id	SHI diameter (mm)	SHI mass (g)	corrected SHI mass (g)	Velocity (m/s)	Kinetic Energy (J)	corrected Kinetic Energy (J)	
1	B6	15 mm	1,55	1,47	157,14	19,14	18,15	Matrix crack
2	B6	15 mm	1,61	1,53	160	20,61	19,58	Matrix crack
3	B6	15 mm	1,57	1,49	160	20,10	19,07	Matrix crack
4	B6	15 mm	1,69	1,61	157,14	20,87	19,88	Matrix crack
5	B6	15 mm	1,68	1,60	160,00	21,50	20,48	Matrix crack
6	B6	15 mm	1,56	1,48	162,86	20,69	19,63	Matrix crack
7	B6	15 mm	1,60	1,52	157,14	19,76	18,77	Matrix crack
8	B6	15 mm	1,51	1,43	160	19,33	18,30	Matrix crack
9	B6	15 mm	1,59	1,51	160	20,35	19,33	Matrix crack
10	B6	15 mm	1,62	1,54	165,71	22,24	1,15	Matrix crack

Table A.7: Sample B6 impacted with 15mm SHI impacted at 160m/s test results

S,no	Sample Id	SHI diameter (mm)	SHI mass (g)	corrected SHI mass (g)	Velocity (m/s)	Kinetic Energy (J)	corrected Kinetic Energy (J)	
1	A7	15 mm	1,58	1,50	160	20,22	18,52	Matrix crack
2	A7	15 mm	1,41	1,33	160	18,05	17,02	Matrix crack
3	A7	15 mm	1,45	1,37	162,86	19,23	18,17	Matrix crack
4	A7	15 mm	1,45	1,37	160	18,56	17,54	Matrix crack
5	A7	15 mm	1,56	1,48	160	19,97	18,94	Matrix crack
6	A7	15 mm	1,55	1,47	160	19,84	18,82	Matrix crack
7	A7	15 mm	1,63	1,55	162,86	21,62	20,55	Matrix crack
8	A7	15 mm	1,67	1,59	160	21,38	20,35	Matrix crack
9	A7	15 mm	1,64	1,56	157,14	20,25	19,26	Matrix crack
10	A7	15 mm	1,40	1,32	157,14	17,29	16,30	Matrix crack

Table A.8: Sample A7 impacted with 15mm SHI at 160m/s test results

S,no	Sample Id	SHI diameter (mm)	SHI mass (g)	corrected SHI mass (g)	Velocity (m/s)	Kinetic Energy (J)	corrected Kinetic Energy (J)	Observation
1	A5	15 mm	1,43	1,35	162,86	18,96	17,90	Matrix crack
2	A5	15 mm	1,62	1,54	157,14	20,00	19,01	Matrix crack
3	A5	15 mm	1,48	1,40	160	18,94	17,92	Matrix crack
4	A5	15 mm	1,62	1,54	157,14	20,00	19,01	Matrix crack
5	A5	15 mm	1,64	1,56	157,14	20,25	19,26	Matrix crack
6	A5	15 mm	1,62	1,54	162,86	21,48	20,42	Matrix crack
7	A5	15 mm	1,55	1,47	162,86	20,55	19,49	Matrix crack
8	A5	15 mm	1,51	1,43	157,14	18,64	17,66	Matrix crack
9	A5	15 mm	1,54	1,46	165,71	21,15	20,05	Matrix crack
10	A5	15 mm	1,50	1,42	140,00	14,70	13,92	Matrix crack

Table A.9: Sample A5 impacted with 15mm SHI impacted at 160 m/s test results

S,no	Sample Id	SHI diameter (mm)	SHI mass (g)	corrected SHI mass (g)	Velocity (m/s)	Kinetic Energy (J)	corrected Kinetic Energy (J)	
1	A3	18 mm	2,92	2,82	134,29	26,33	25,43	Matrix crack
2	A3	18 mm	2,80	2,70	154,29	33,32	32,13	Matrix crack
3	A3	18 mm	3,06	2,96	145,71	32,48	31,42	Matrix crack
4	A3	18 mm	2,80	2,70	145,71	29,76	28,70	Matrix crack
5	A3	18 mm	3,06	2,96	140,00	30,03	29,05	Matrix crack
6	A3	18 mm	2,80	2,70	142,86	28,52	27,50	Matrix crack
7	A3	18 mm	3,00	2,90	137,14	28,20	27,26	Matrix crack
8	A3	18 mm	2,74	2,64	28,57	1,12	1,08	Matrix crack
9	A3	18 mm	2,77	2,67	142,86	28,23	27,21	Matrix crack
10	A3	18 mm	2,99	2,89	137,14	28,08	27,14	Matrix crack
11	A3	18 mm	2,99	2,89	140,00	29,35	28,37	Matrix crack

Table A.10: Sample A3 impacted with 18mm SHI at 140m/s test results

S,no	Sample Id	SHI diameter (mm)	SHI mass (g)	corrected SHI mass (g)	Velocity (m/s)	Kinetic Energy (J)	corrected Kinetic Energy (J)	Observation
1	A6	18 mm	2,31	2,21	137,14	21,72	20,78	Matrix crack
2	A6	18 mm	2,85	2,75	137,14	26,77	25,83	Matrix crack
3	A6	18 mm	2,90	2,80	142,86	28,44	27,46	Matrix crack
4	A6	18 mm	2,90	2,80	142,86	29,59	28,57	Matrix crack
5	A6	18 mm	2,39	2,29	151,43	21,52	20,62	Matrix crack
6	A6	18 mm	2,94	2,84	145,71	28,84	27,86	Matrix crack
7	A6	18 mm	3,04	2,94	142,86	26,23	25,37	Matrix crack
8	A6	18 mm	2,85	2,75	142,86	26,84	25,90	Matrix crack
9	A6	18 mm	2,90	2,80	142,86	27,30	26,36	Matrix crack
10	A6	18 mm	2,97	2,87	142,86	29,12	28,14	Matrix crack

Table A.11: Sample A6 impacted with 18mm SHI at 140m/s test results

S,no	Sample Id	SHI diameter (mm)	SHI mass (g)	corrected SHI mass (g)	Velocity (m/s)	Kinetic Energy (J)	corrected Kinetic Energy (J)	Observation
1	A1	18 mm	2,92	2,82	134,29	26,32	25,42	Matrix crack
2	A1	18 mm	2,94	2,84	117,14	20,19	19,50 Matrix crack	
3	A1	18 mm	2,84	2,74	120	20,44	19,72	Matrix crack
4	A1	18 mm	3,56	3,46	114,29	23,23	22,58	Matrix crack
5	A1	18 mm	2,90	2,80	117,14	19,89	19,20	Matrix crack
6	A1	18 mm	2,79	2,69	117,14	19,16	18,48	Matrix crack
7	A1	18 mm	2,93	2,83	122,86	22,13	21,37	Matrix crack
8	A1	18 mm	2,74	2,64	114,29	17,89	17,24	Matrix crack
9	A1	18 mm	2,80	2,70	120,00	20,13	19,41	Matrix crack
10	A1	18 mm	2,77	2,67	117,14	19,00	18,31	Matrix crack

Table A.12: Sample A1 impacted with 18mm SHI at 120m/s test results

S,no	Sample Id	SHI diameter (mm)	SHI mass (g)	corrected SHI mass (g)	Velocity (m/s)	Kinetic Energy (J)	corrected Kinetic Energy (J)	Observation
1	A4	18 mm	3,00	2,90	120	21,58	20,86	Matrix crack
2	A4	18 mm	2,87	2,77	122,86	21,64	20,88	Matrix crack
3	A4	18 mm	2,67	2,57	114,29	17,40	16,75	Matrix crack
4	A4	18 mm	2,70	2,60	120	19,42	18,70	Matrix crack
5	A4	18 mm	2,83	2,73	120	20,35	19,63	Matrix crack
6	A4	18 mm	3,00	2,90	122,86	22,63	21,87	Matrix crack
7	A4	18 mm	2,90	2,80	117,14	19,93	19,24	Matrix crack
8	A4	18 mm	2,96	2,86	120	21,35	20,63	Matrix crack
9	A4	18 mm	2,86	2,76	117,14	19,60	18,91	Matrix crack
10	A4	18 mm	3,02	2,92	120	21,74	21,02	Matrix crack

Table A.13: Sample A4 impacted with 18mm SHI at 120m/s test results

S,no	Sample Id	SHI diameter (mm)	SHI mass (g)	corrected SHI mass (g)	Velocity (m/s)	Kinetic Energy (J)	corrected Kinetic Energy (J)	Observation
1	B5	18 mm	2,93	2,83	114,29	19,10	18,45	No Damage
2	B5	18 mm	2,94	2,84	102,86	15,53	15,00	No Damage
3	B5	18 mm	2,94	2,84	108,57	17,73	16,73	No Damage
4	B5	18 mm	2,67	2,57	105,71	14,90	14,34	No Damage
5	B5	18 mm	2,81	2,71	100	14,06	13,56	No Damage
6	B5	18 mm	2,86	2,76	111,43	17,77	17,15	No Damage
7	B5	18 mm	2,86	2,76	108,57	16,88	16,29	No Damage
8	B5	18 mm	2,84	2,74	105,71	15,89	15,33	No Damage
9	B5	18 mm	2,84	2,74	111,43	17,63	17,01	No Damage
10	B5	18 mm	3,00	2,90	111,43	18,60	17,98	No Damage
11	B5	18 mm	2,88	2,78	111,43	17,87	17,25	No Damage
12	B5	18 mm	2,97	2,87	117,14	20,39	18,75	Matrix crack

Table A.14: Sample B5 impacted with 18mm SHI at 110m/s test results

S,no	Sample Id	SHI diameter (mm)	SHI mass (g)	corrected SHI mass (g)	Velocity (m/s)	Kinetic Energy (J)	corrected Kinetic Energy (J)	
1	A8	18 mm	2,87	2,77	108,57	16,92	16,33	No Damage
2	A8	18 mm	2,91	2,81	111,43	18,04	17,42	No Damage
3	A8	18 mm	2,86	2,76	120	20,58	18,93	Matrix crack
4	A8	18 mm	2,71	2,61	105,71	15,14	14,58	Matrix crack
5	A8	18 mm	2,95	2,85	111,43	18,31	17,69	Matrix crack
6	A8	18 mm	2,90	2,80	111,43	18,00	17,38	Matrix crack
7	A8	18 mm	2,87	2,77	111,43	17,84	17,22	Matrix crack
8	A8	18 mm	2,70	2,60	100	13,48	12,98	Matrix crack
9	A8	18 mm	2,96	2,86	111,43	18,35	17,73	Matrix crack
10	A8	18 mm	2,86	2,76	108,57	16,84	16,25	Matrix crack
10	A8	18 mm	2,83	2,73	108,57	16,70	16,11	Matrix crack

Table A.15: Sample A8 impacted with 18mm SHI at 110m/s test results

S,no	Sample Id	SHI diameter (mm)	SHI mass (g)	corrected SHI mass (g)	Velocity (m/s)	Kinetic Energy (J)	corrected Kinetic Energy (J)	
1	B9	18 mm	2,89	2,79	108,57	17,04	16,45	No Damage
2	B9	18 mm	2,98	2,88	108,57	17,56	16,97	No Damage
3	B9	18 mm	2,99	2,89	108,57	17,62	17,03	No Damage
4	B9	18 mm	2,94	2,84	114,29	19,21	18,56	Matrix crack
5	B9	18 mm	2,91	2,81	108,57	17,13	16,54	Matrix crack
6	B9	18 mm	3,04	2,94	114,29	19,83	19,18	Matrix crack
7	B9	18 mm	2,96	2,86	108,57	17,43	16,84	Matrix crack
8	B9	18 mm	2,93	2,83	114,29	19,15	18,50	Matrix crack
9	B9	18 mm	2,88	2,78	114,29	18,82	18,17	Matrix crack
10	B9	18 mm	2,80	2,70	108,57	16,53	15,94	Matrix crack

Table A.16: Sample B9 impacted with 18mm SHI at 110m/s test results

S,no	Sample Id	SHI diameter (mm)	SHI mass (g)	corrected SHI mass (g)	Velocity (m/s)	Kinetic Energy (J)	corrected Kinetic Energy (J)	Observation
1	A9	18 mm	2,80	2,70	97,14	13,23	12,76	
2	A9	18 mm	2,72	2,62	97,14	12,84	12,37	
3	A9	18 mm	2,98	2,88	114,29	19,45	18,80	Matrix crack
4	A9	18 mm	2,73	2,63	105,71	15,25	14,69	Matrix crack
5	A9	18 mm	2,82	2,72	100	14,09	13,59	Matrix crack
6	A9	18 mm	2,67	2,57	94,29	11,86	11,42	Matrix crack
7	A9	18 mm	2,96	2,86	102,86	15,67	15,14	Matrix crack
8	A9	18 mm	2,84	2,74	102,86	15,03	14,50	Matrix crack
9	A9	18 mm	2,72	2,62	105,71	15,17	14,61	Matrix crack
10	A9	18 mm	2,72	2,62	105,71	15,19	14,63	Matrix crack

Table A.17: Sample A9 impacted with 18mm SHI at 100m/s test results

S,no	Sample Id	SHI diameter (mm)	SHI mass (g)	corrected SHI mass (g)	Velocity (m/s)	Kinetic Energy (J) corrected Kinetic Energy (J)		
1	B10	18 mm	2,84	2,74	97,14	13,38	12,91	No Damage
2	B10	18 mm	3,09	2,99	108,57	19,18	18,56	Matrix crack
3	B10	18 mm	2,86	2,76	108,57	16,87	16,28	Matrix crack
4	B10	18 mm	2,83	2,83	108,57	16,70	16,11	Matrix crack
5	B10	18 mm	2,78	2,68	100	13,92	13,42	Matrix crack
6	B10	18 mm	3,00	2,90	102,86	15,87	15,35	Matrix crack
7	B10	18 mm	2,94	2,84	100,00	14,71	14,21	Matrix crack
8	B10	18 mm	2,95	2,85	105,71	16,48	15,92	Matrix crack
9	B10	18 mm	3,01	2,91	100,00	15,06	14,56	Matrix crack
10	B10	18 mm	2,93	2,83	105,71	16,37	15,81	Matrix crack

Table A.18: Sample B10 Impacted with 18mm SHI at 100m/s test results

S,no	Sample Id	SHI diameter (mm)	SHI mass (g)	corrected SHI mass (g)	Velocity (m/s)	Kinetic Energy (J)	corrected Kinetic Energy (J)	Observation
1	A10	20 mm	4,51	4,39	57,14	7,36	7,17	No Damage
2	A10	20 mm	4,38	4,26	88,57	17,17	16,70	No Damage
3	A10	20 mm	3,89	3,77	80	12,46	12,08	No Damage
4	A10	20 mm	3,76	3,64	88,57	14,74	14,27	No Damage
5	A10	20 mm	4,11	3,99	85,71	15,09	14,65	No Damage
6	A10	20 mm	4,37	4,25	82,86	15,01	17,78	No Damage
7	A10	20 mm	4,45	4,33	97,14	21,02	19,27	Matrix crack
8	A10	20 mm	4,48	4,36	91,43	18,73	18,22	Matrix crack
9	A10	20 mm	4,45	4,33	97,14	20,98	19,23	Matrix crack
10	A10	20 mm	4,47	4,35	97,14	21,10	19,34	Matrix crack
11	A10	20 mm	4,23	4,11	91,43	17,67	17,17	Matrix crack
12	A10	20 mm	4,54	4,42	91,42	18,97	18,47	Matrix crack

Table A.19: Sample A10 impacted with 20mm SHI at 90m/s test results

B
optical microscpy

B.1. 15mm Hailstone

B.1.1. Sample A2 impact velocity 140 m/s

B.1.1.1. Sample A2 pre impact

Figure B.1: Sample A2 before impact

B.1.1.2. Sample A2 post 1st impact

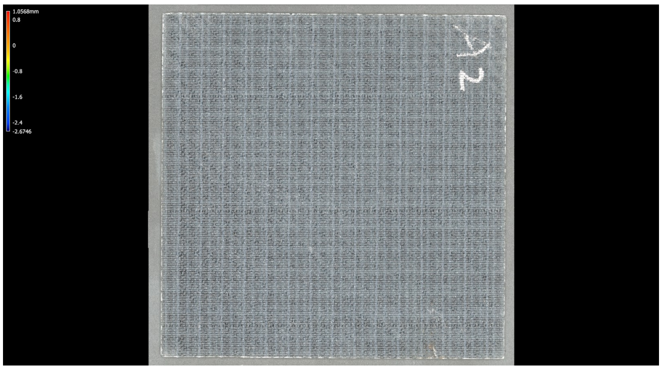

Figure B.2: Sample A2 post 1st impact

B.1.1.3. Sample A2 post 5th impact

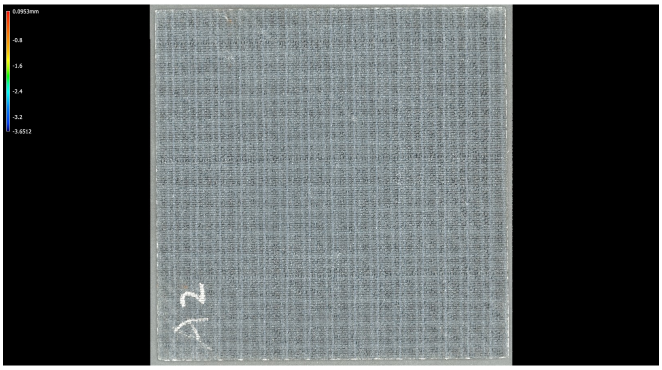

Figure B.3: Sample A2 post 5th impact

B.1.1.4. Sample A2 post 10th impact

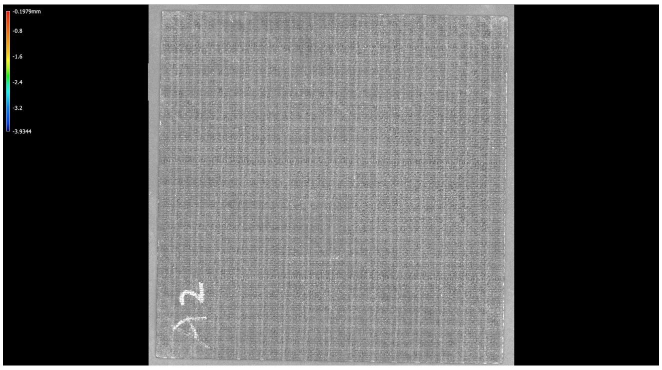

Figure B.4: Sample A2 post 10th impact

B.1.2. Sample B7 impact velocity 150 m/s

B.1.2.1. Sample B7 post 5th impact

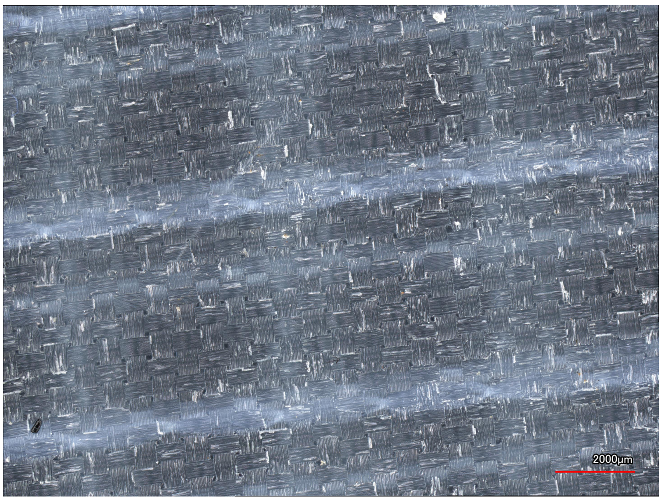

Figure B.5: Sample B7 post 5th impact

B.1.2.2. Sample B7 post 10th impact

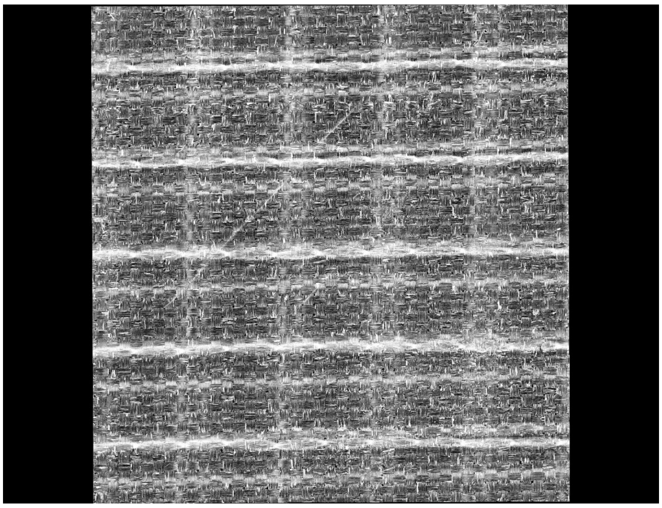

Figure B.6: Sample B7 post 10th impact

B.1.3. Sample A5 impact velocity 160 m/s

B.1.3.1. Sample A5 post 1st impact

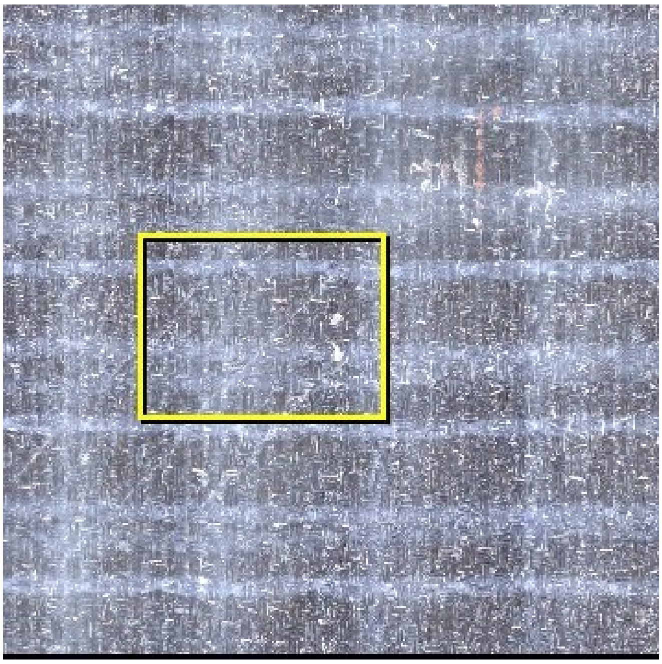

Figure B.7: Sample B6 post 1st impact

B.1.3.2. Sample A5 post 10th impact

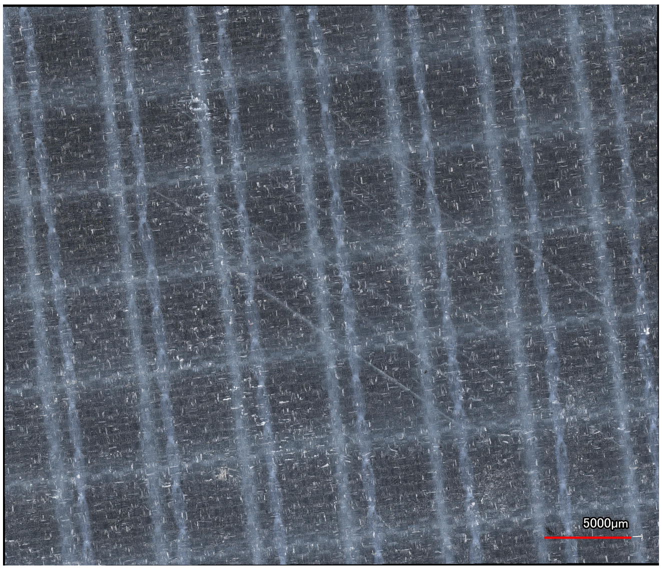

Figure B.8: Sample A5 post 10th impact

B.2. 18mm Hailstone damage evolution

B.2.1. Sample A6 impact velocity 100 m/s

B.2.1.1. Sample A6 post 5th impact

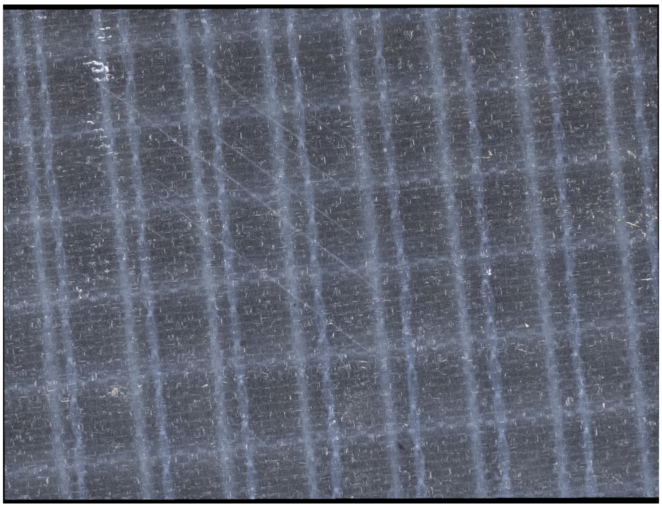

Figure B.9: Sample A6 post 5th impact

B.2.1.2. Sample A6 post 10th impact

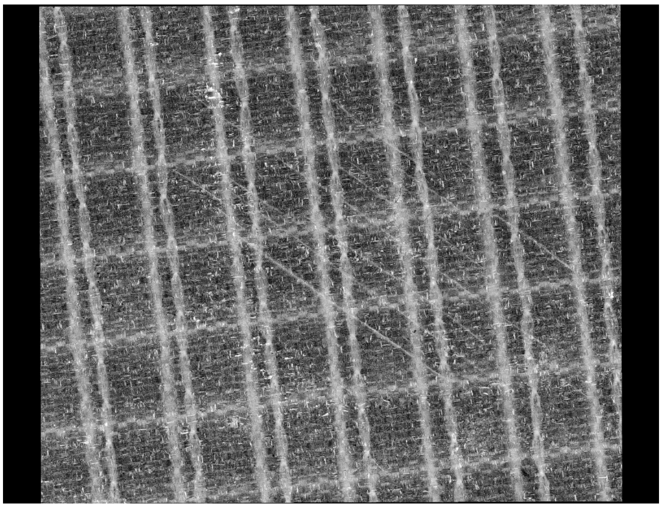

Figure B.10: Sample A6 post 10th impact

B.2.2. Sample A1 impact velocity 120 m/s

B.2.2.1. Sample A1 post 1st impact

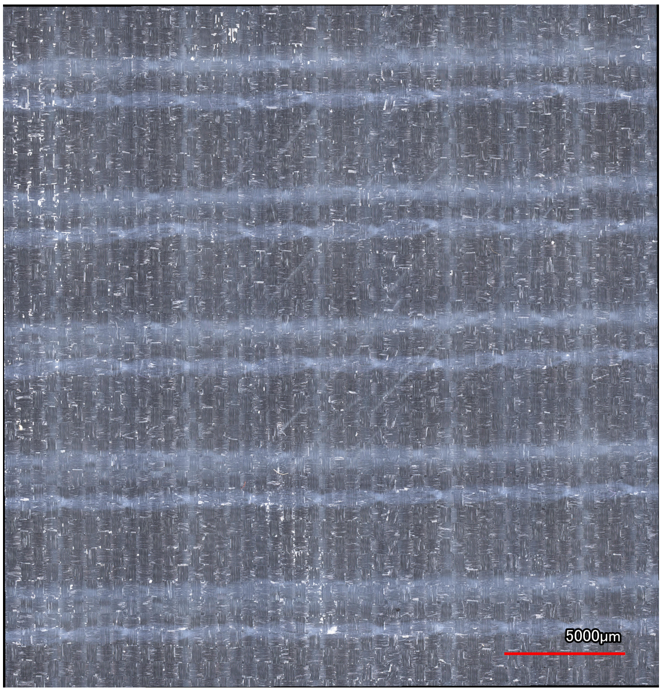

Figure B.11: Sample A1 post 1st impact

B.2.2.2. Sample A1 post 5th impact

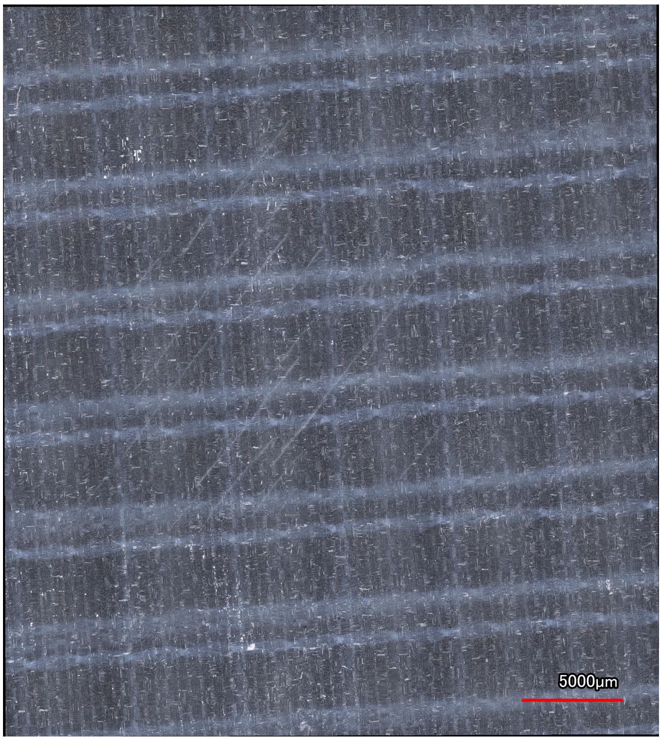

Figure B.12: Sample A1 post 5th impact

B.2.2.3. Sample A1 post 10th impact

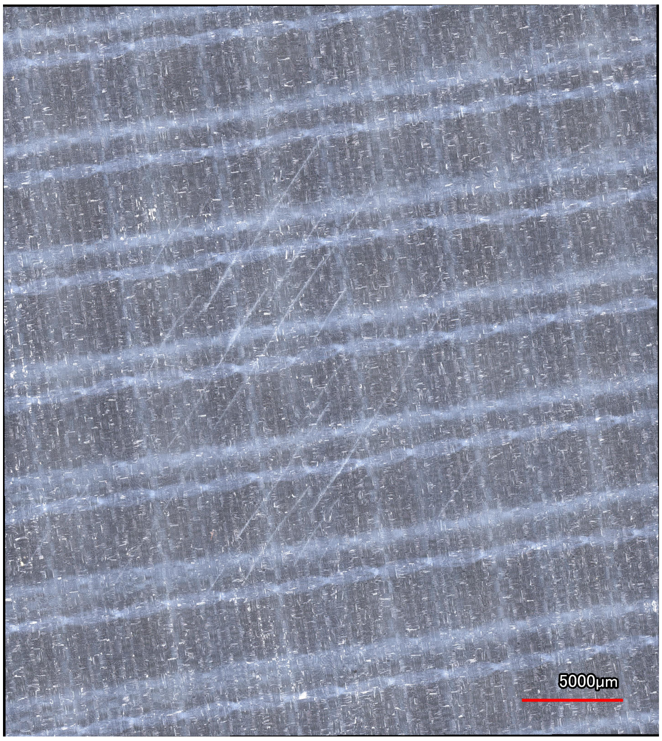

Figure B.13: Sample A1 post 10th impact

B.2.3. Sample B9 impact velocity 110 m/s

B.2.3.1. Sample B9 post 1st impact

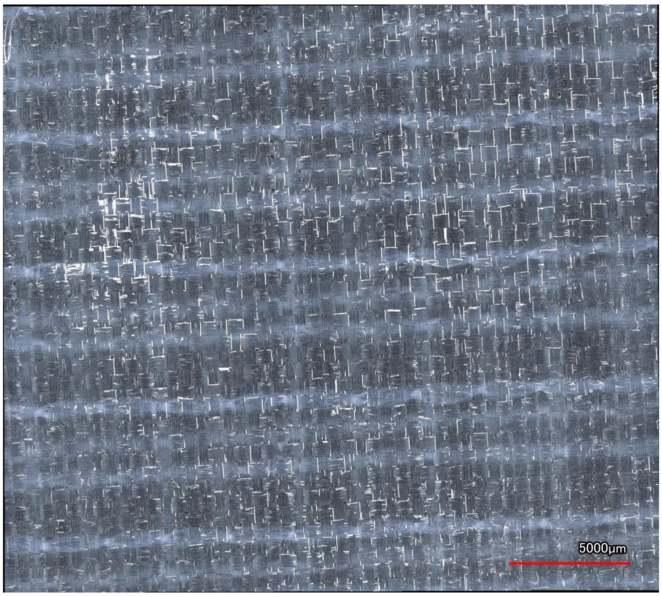

Figure B.14: Sample B9 post 1st impact

B.2.3.2. Sample B9 post 5th impact

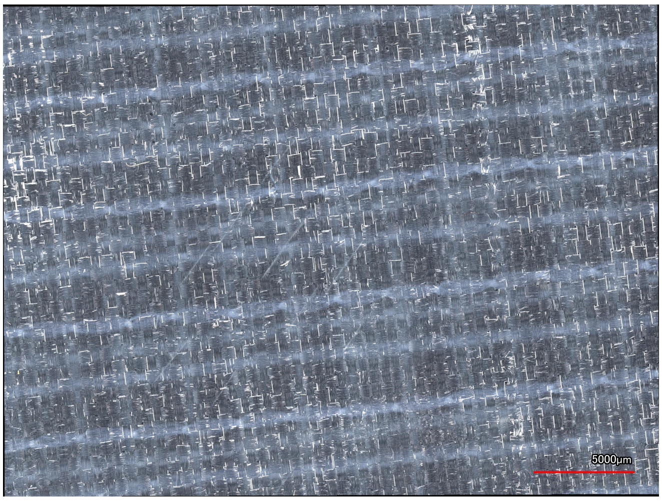

Figure B.15: Sample B9 post 5th impact

B.2.3.3. Sample B9 post 10th impact

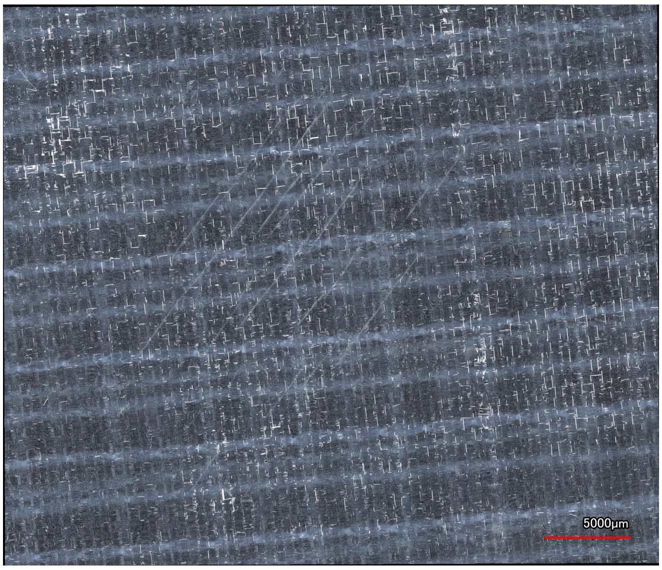

Figure B.16: Sample B9 post 10th impact

B.2.4. Sample B10 impact velocity 100 m/s

B.2.4.1. Sample B10 pre impact

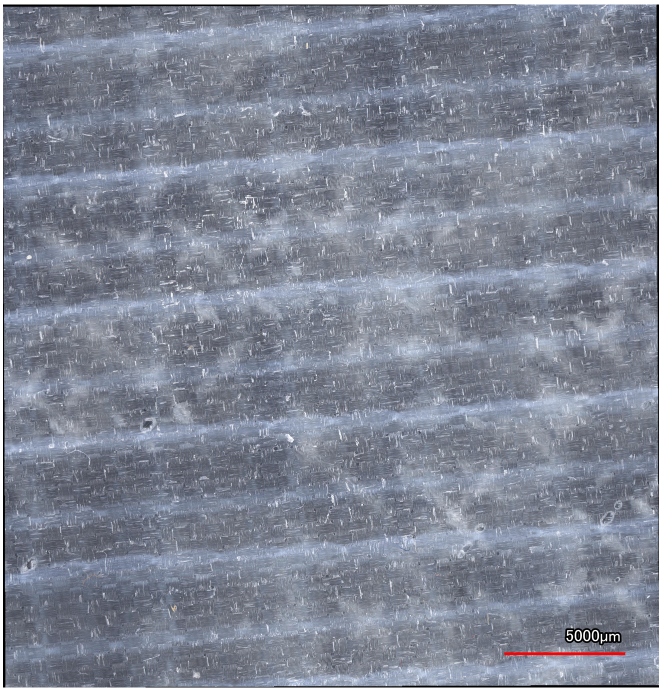

Figure B.17: Sample B10 before impact

B.2.4.2. Sample B10 post 1st impact

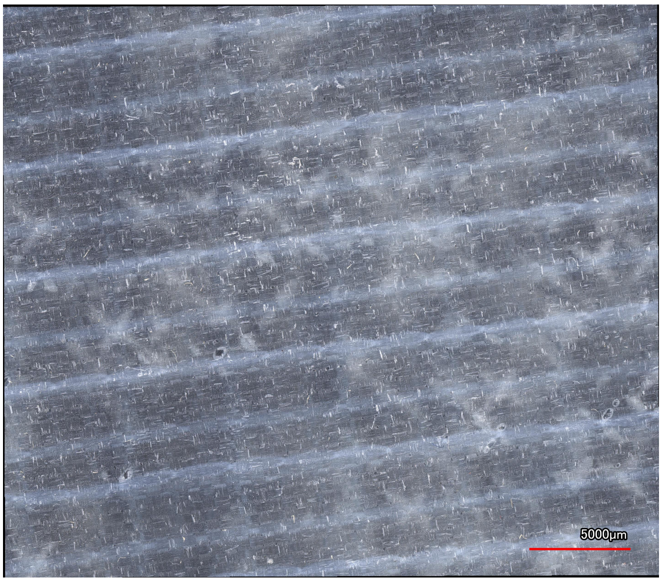

Figure B.18: Sample B10 post 1st impact

B.2.4.3. Sample B10 post 5th impact

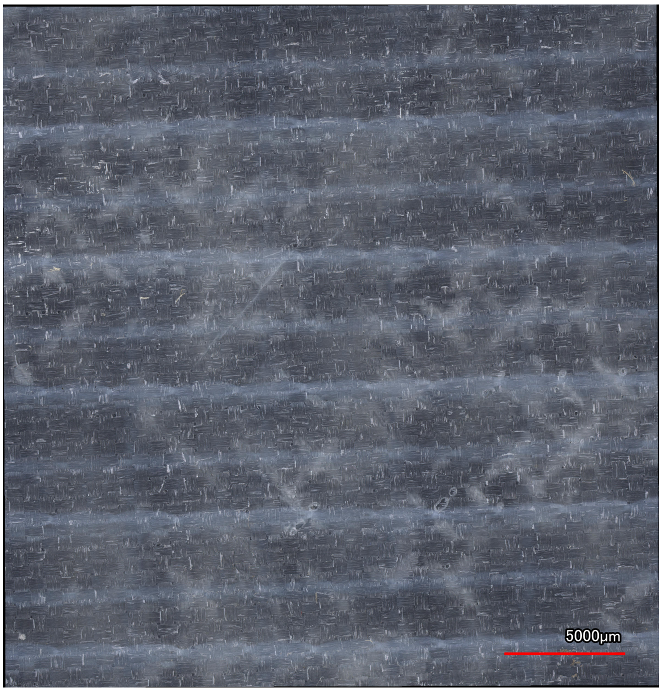

Figure B.19: Sample B10 post 5th impact

B.2.4.4. Sample B10 post 10th impact

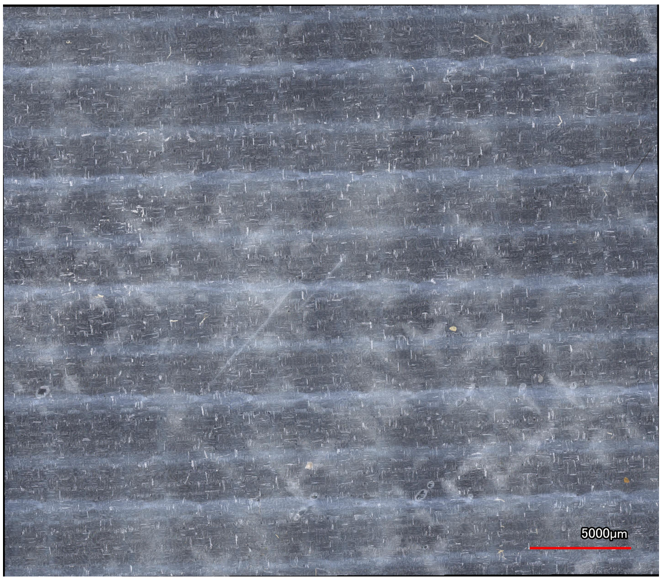

Figure B.20: Sample B10 post 10th impact

B.2.5. Sample A10 impact velocity 100 m/s

B.2.5.1. Sample A10 post 1st impact

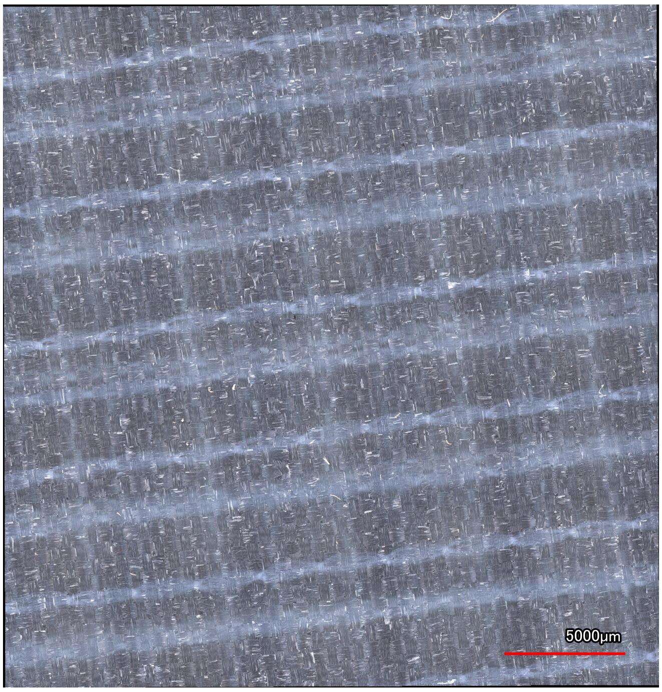

Figure B.21: Sample A10 post 1st impact

B.2.5.2. Sample A10 post 5th impact

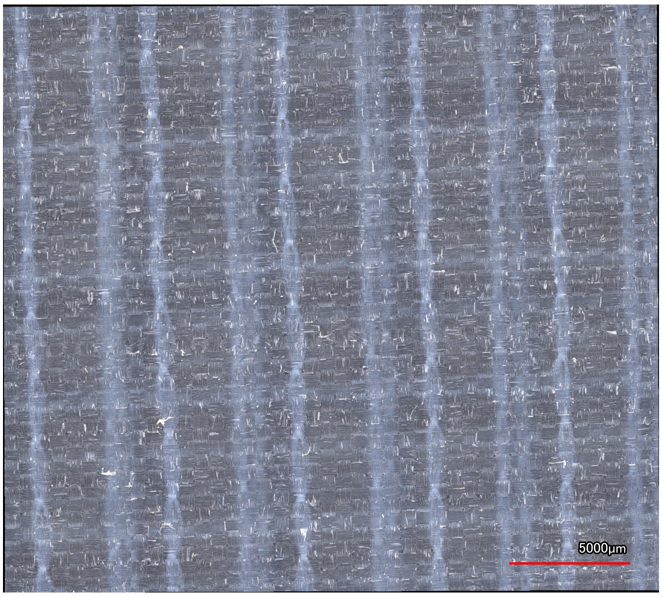

Figure B.22: Sample A10 post 5th impact

B.2.5.3. Sample A10 post 10th impact

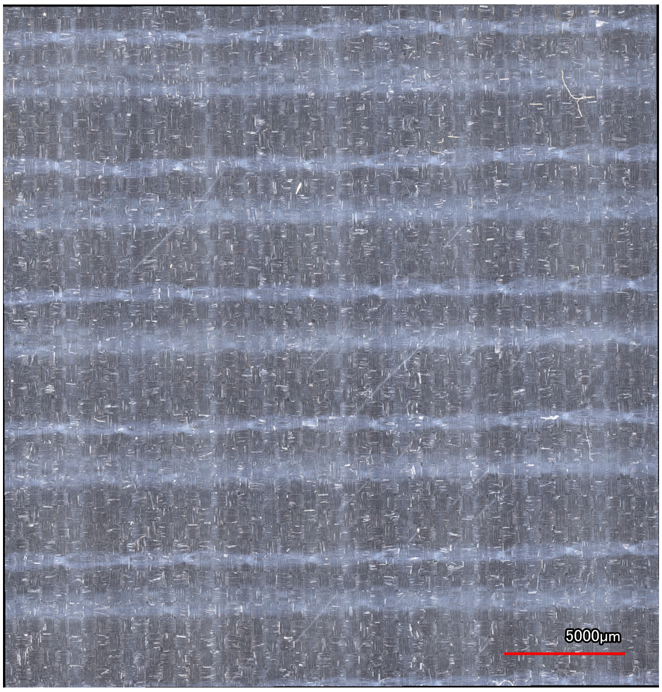

Figure B.23: Sample A10 post 10th impact

C

C-scan Images

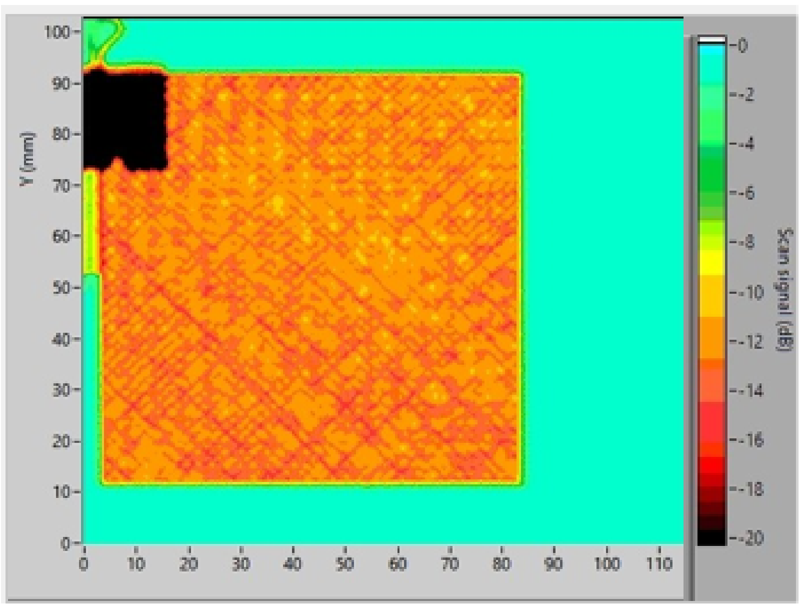

Figure C.1: C-scan image of sample A2 subjected to 1 impact with 15mm hailstone at 140m/s

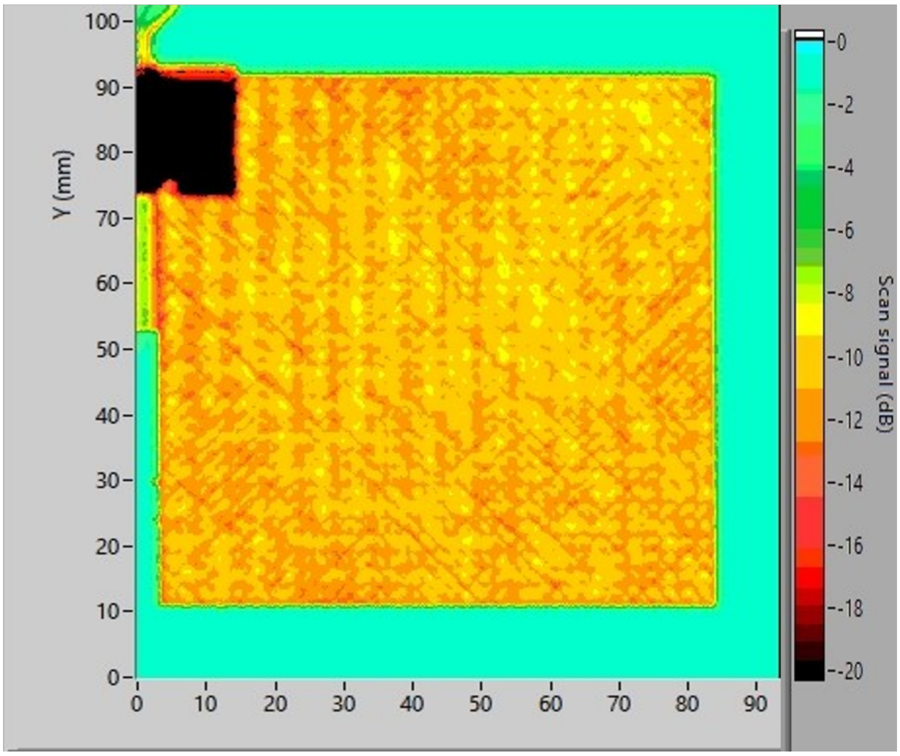

Figure C.2: C-scan image of sample A2 subjected to 5 impacts with 15mm hailstone at 140m/s

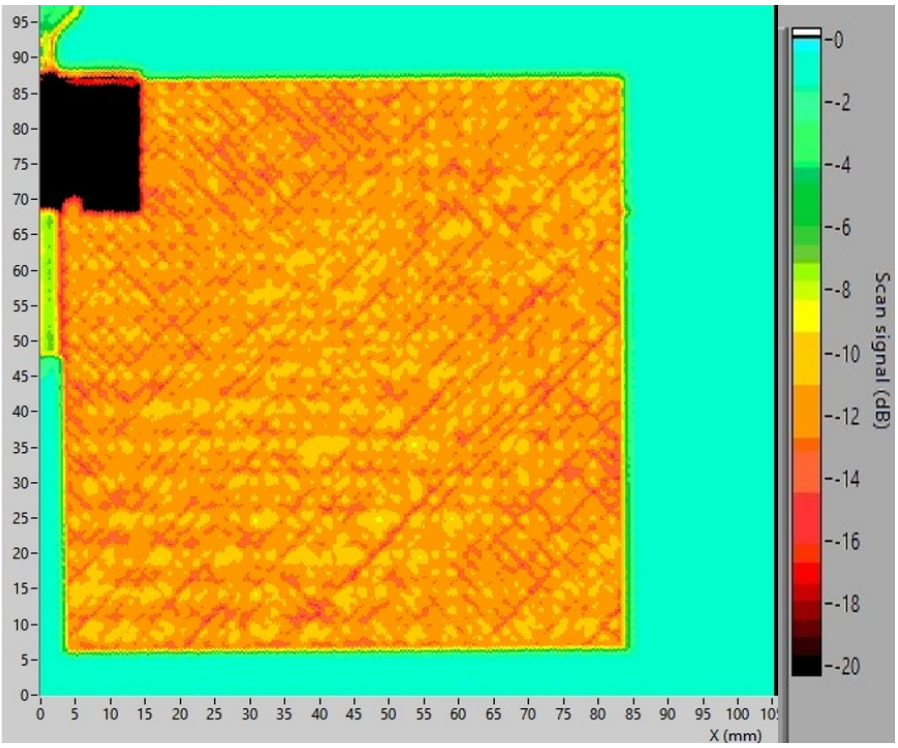

Figure C.3: C-scan image of sample A2 subjected to 10 impacts with 15mm hailstone at 140m/s

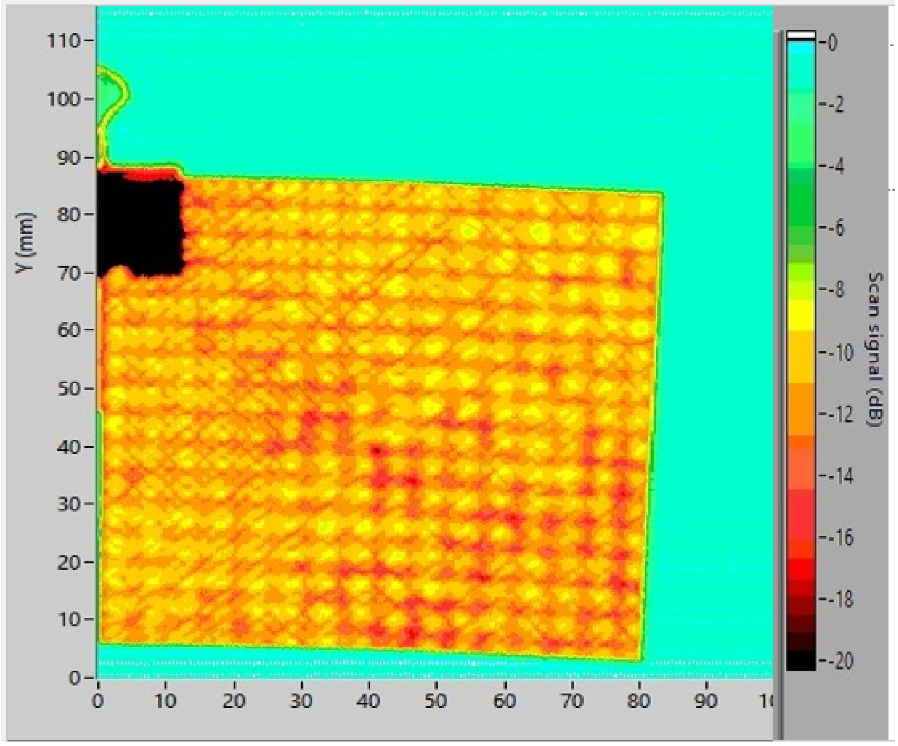

Figure C.4: C-scan image of sample B4 subjected to 10 impacts with 15mm hailstone at 150m/s

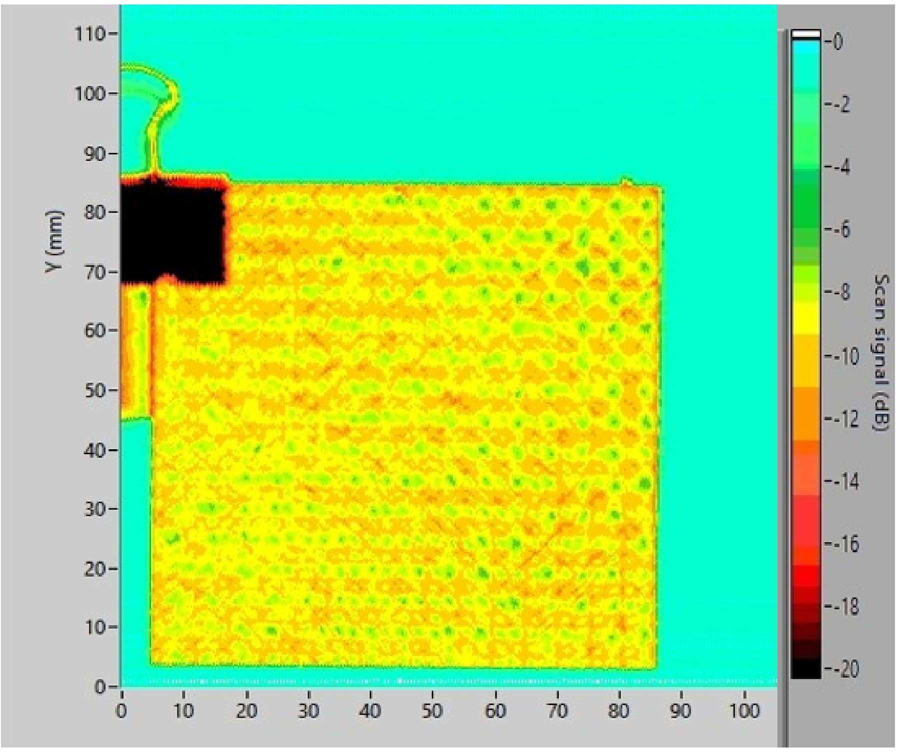

Figure C.5: C-scan image of sample A7 subjected to 10 impacts with 15mm hailstone at 160m/s

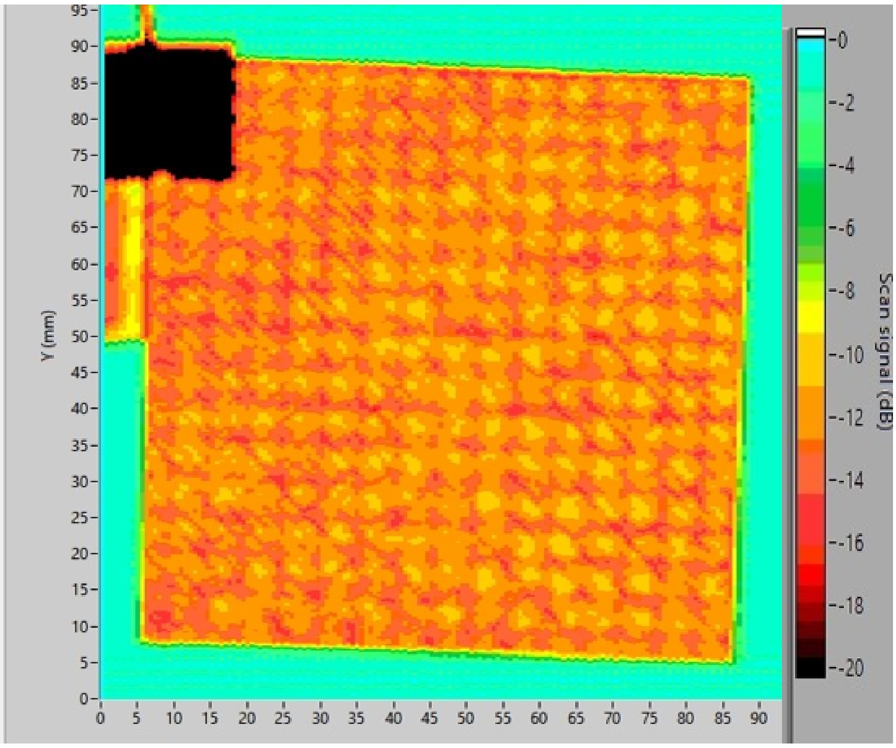

Figure C.6: C-scan image of sample A6 subjected to 10 impacts with 18mm hailstone at 140m/s

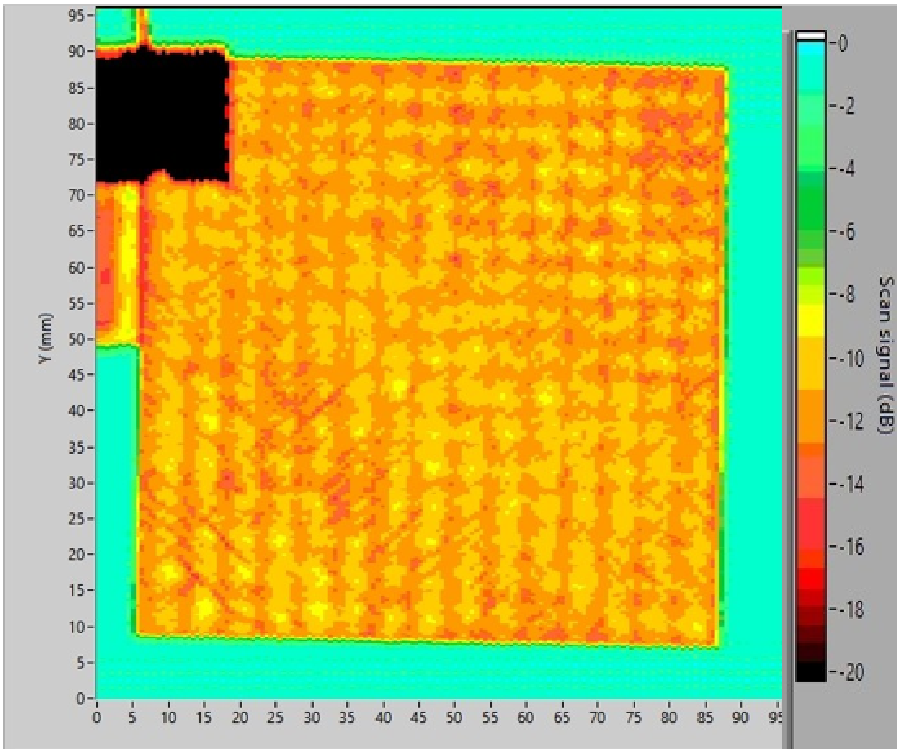

Figure C.7: C-scan image of sample A3 subjected to 10 impacts with 18mm hailstone at 120m/s

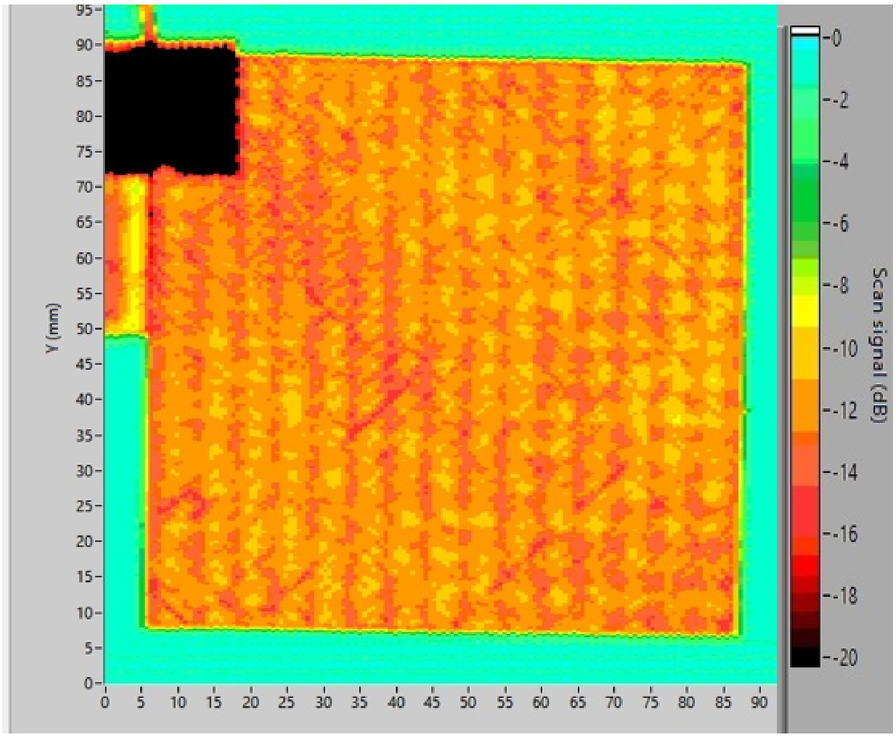

Figure C.8: C-scan image of sample A8 subjected to 10 impacts with 18mm hailstone at 110m/s

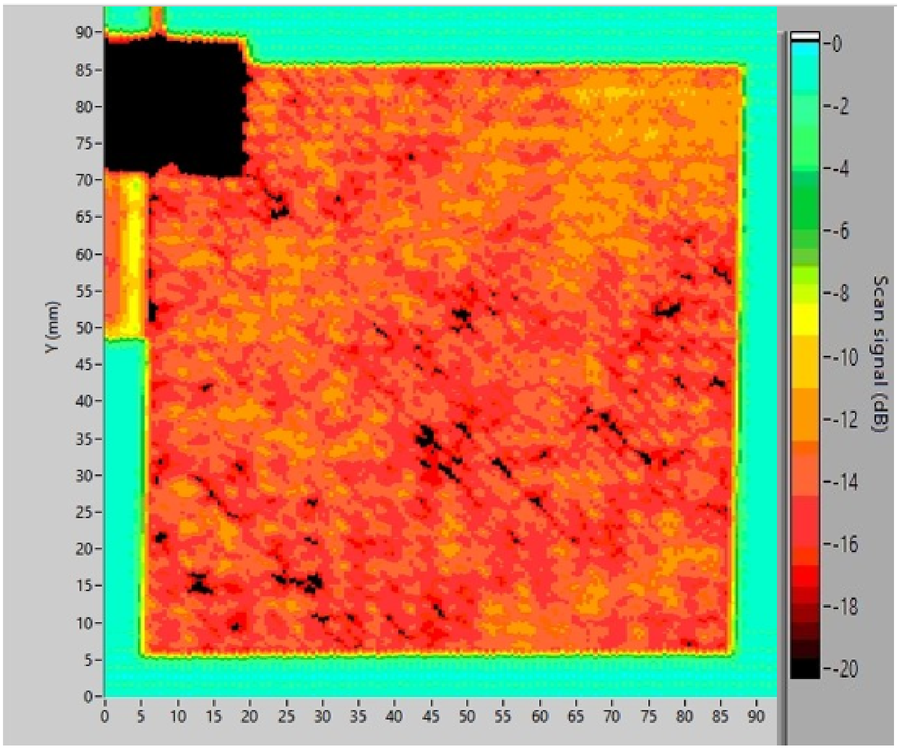

Figure C.9: C-scan image of sample B10 subjected to 10 impacts with 18mm hailstone at 100m/s

D

Cross-sectional Microscopy

Cross-sectional Microstructure of Sample B4 subjected to 10 impacts 15 mm hailstone at 150m/s:

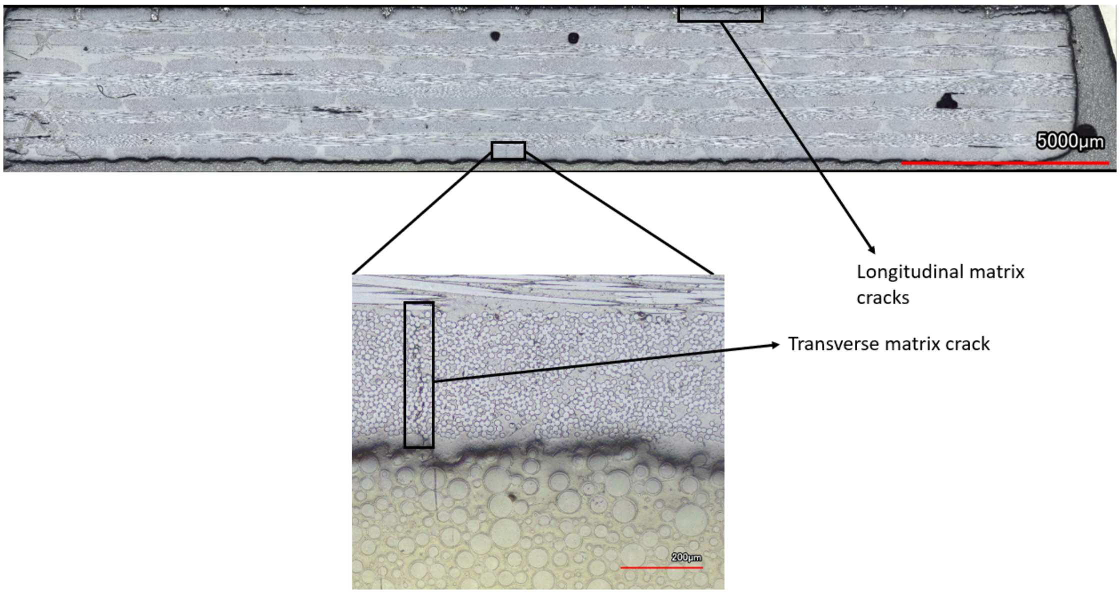

Figure D.1: Cross-sectional view of sample B4 subjected to 10 impacts 15 mm hailstone at 150m/s

Cross-sectional Microstructure of Sample B6 subjected to 10 impacts with 15 mm hailstone at 160m/s:

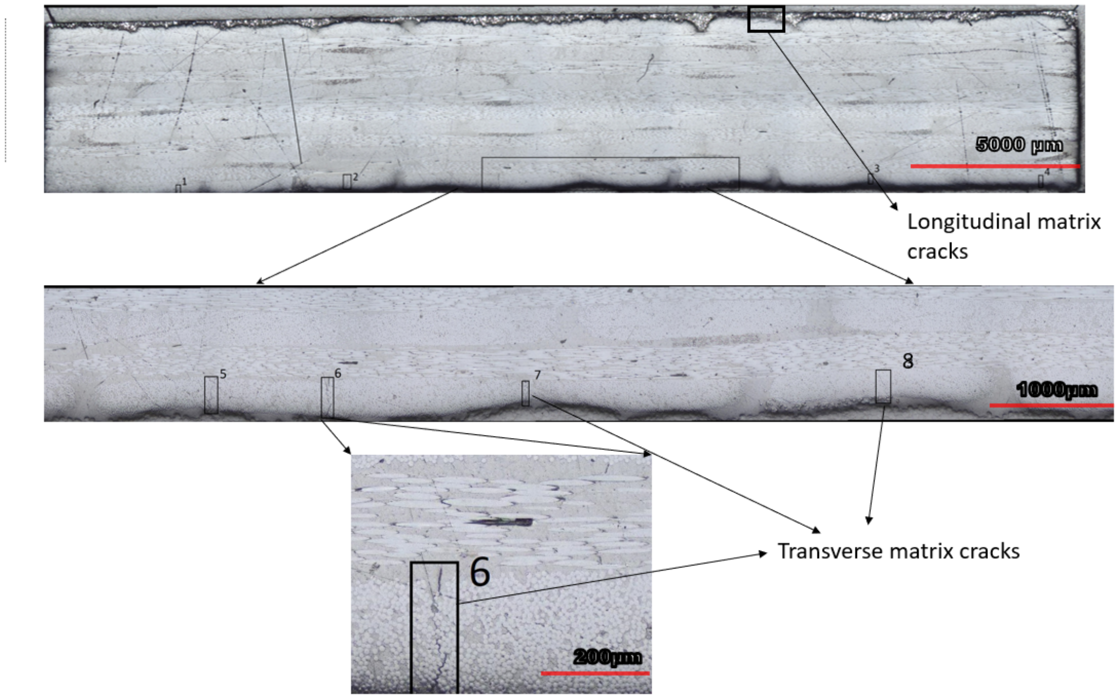

Figure D.2: Cross-sectional view of sample B6 subjected to 10 impacts with 15 mm hailstone at 160m/s

Cross-sectional Microstructure of sample B5 subjected to 10 impacts with impact 18 mm hailstone at 110m/s:

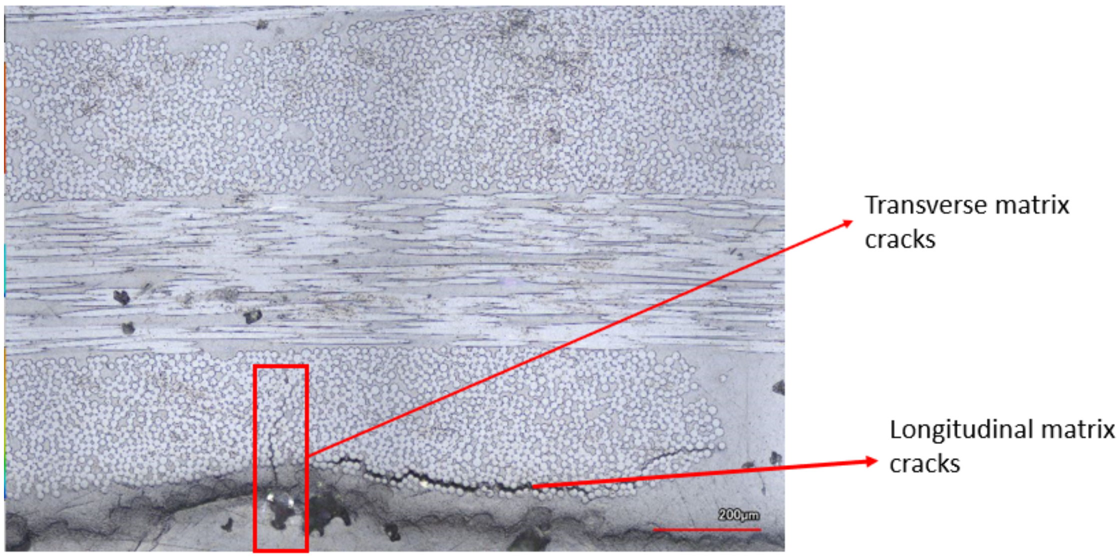

Figure D.3: Cross sectional view of sample B5 subjected to 10 impacts with impact 18 mm hailstone at 110m/s

Cross-sectional Microstructure of Sample A9 subjected to 10 impacts with 18 mm hailstone at 100m/s:

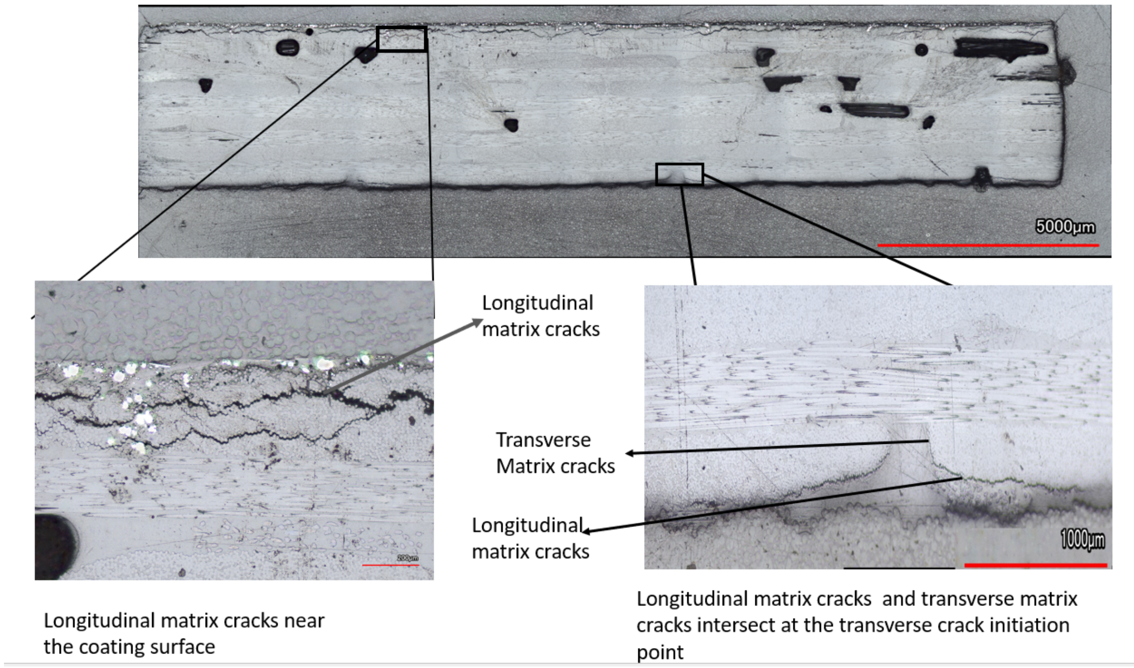

Figure D.4: Cross-sectional view of sample view subjected to 10 impacts with 18 mm hailstone at 100m/s

Cross-sectional Microstructure of Sample A10 subjected to 10 impacts with 20 mm hailstone at 90m/s:

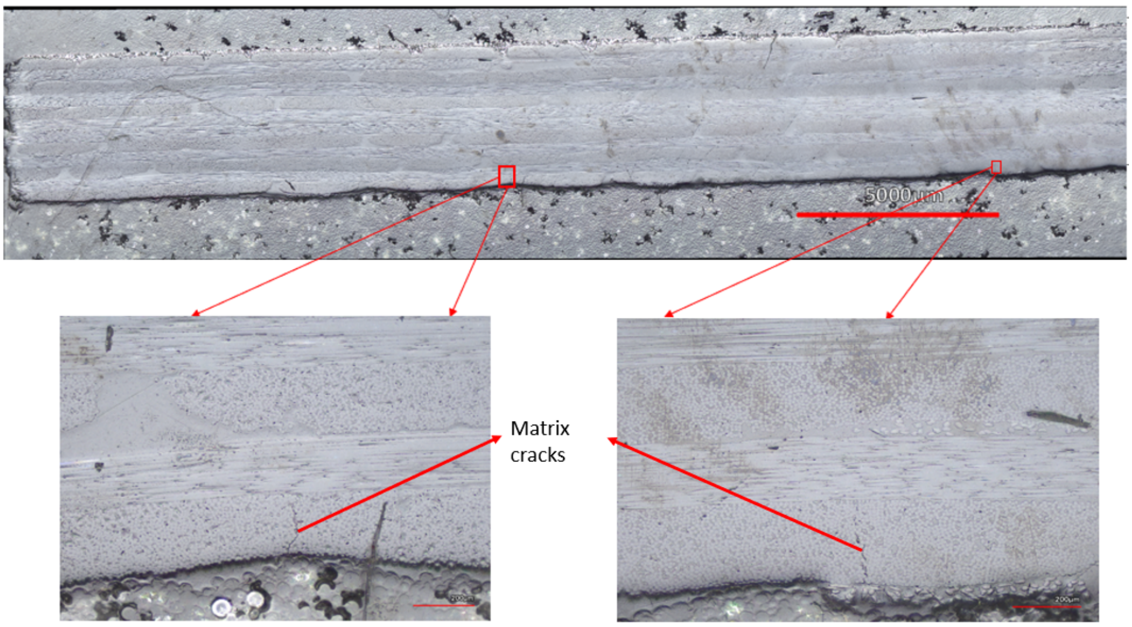

Figure D.5: Cross sectional view of sample A10 view subjected to 10 impacts with 20 mm hailstone at 90m/s